Cellular Solids Based on Biopolymer Nanocomposites: For Hypersonic Heat Shields Aboard Sounding Rockets

Anand Raja

TU Delft

Materials Science and Engineering

DARE Delft Aerospace Rocket Engineering

Hypersonic Heat Shields A PRG Project

MS53035: MSE Thesis

Cellular Solids Based on Biopolymer Nanocomposites: For Hypersonic Heat Shields Aboard Sounding Rockets

by

Anand Raja

in partial fulfilment of the requirements to obtain the degree

Master of Science - Materials Science and Engineering
at the Delft University of Technology.
Date of Defence: Friday, 27th November 2020

Student Number:	**4770390**
Chair/Supervisor:	**Prof. dr. S.J. Picken, TU Delft**
Co - Supervisor:	**Dr. M.A. Bessa, TU Delft**
Committee Member:	**Prof. dr. ir. J. Sietsma, TU Delft**
Committee Member:	**Dr. J. Zlopaša, TU Delft**
Advisor:	**MSc. S. Pereira Espíndola, TU Delft**

Preface

"I hope everything is okay upon your return to India.". These were the parting words of my dear departed grandfather on the night of 15th August 2018; the day I embarked to Delft to pursue a Masters degree in Science. And, on the morning of 11th September 2020, I was awakened to the terrible news that my grandmother also succumbed to her prolonged illness. Often are we so consumed by our ambitions, that we forget to take a moment to pay tribute to those who have helped us reach our current place. Appa, Amma, Adi and Paati, I would be nowhere without your support, your belief in my abilities and your love for me. If I haven't taken a moment to say this verbally, thank you. Trudy the Love Barbarian, whilst I may only have this thesis to contend with, some others contend with life itself. Your fighting spirit provides the motivation I need to get out of bed on most days.

In many ways, this thesis is supposed to reflect on my individual prowess in Materials Science and Engineering. But let's face it, no one likes letting an ape loose with a blowtorch for good measure. To Stephen *Dr Slimy* Picken. You have been less of a menacing supervisor and more of a close companion since our encounter within WASCOM. Our innate ability to spam Whatsapp groups will always continue to provide me with inspiration in my professional life. To Dr Miguel Bessa and Dr Jilt Sietsma. Whilst our conversations have been brief, they have provided me with the uniquely alternate perspective on my endeavours over the last nine months. I thank you for that. To Jure, my brother from a Croatian mother. None of this would have been possible without your incessant ramblings about current affairs, Croatia and alginate; in that order. To Suellen. One always needs a companion around the lab to microwave some glycerol and discuss how despite Nolan's efforts, entropy and time travel are still confusing topics.

To Ajo, my Mallu friend not in *de Gelf.* It's always nice to have someone who has synced perfectly with your weird wavelength. We will always have that funny Goa story to narrate to everyone. To Moonmoon, Deus Vult, Leon and Nimbehulli. When I met you guys at the age of 20, I was probably too naive to fall prey to your MBTI and Political Compass fiasco. Now, four years later, I'm probably no better and still fall prey to our long and drawn out conversations on Skype.

To Ath, Teriyaki Sauce, Ta Kiṭa Dum, Sampy, The Irrational Pai, Thesis Life, Sripathy Ji, Mr Dot, Kencha and John. Thank you for the free food, Friday night poker games, CS: GO savagery, Bosboom cricket matches and any other opportunity to chill out. In those moments I could be my Super Saiyan self and take a moment to enjoy life.

Last but definitely not the least, to the glorious Parachute Research Group within DARE. I would never have had the opportunity to work on something as exciting as heat shields had it not been for you guys. To Esmée. Thank you for helping me find something sensible to do within PRG. In case no one has ever told you this, your work ethic is an inspiration to every single DARE member. It has been a pleasure working closely with you. To Lars, Bram and Mark (aka the PRG dinosaurs). If Owncloud ever crashes (knocks on wood), PRG (and even DARE) would survive because of the immense knowledge and practical skills that you guys bring to the table. To Thomas Britting (because there are two Thomases and it shouldn't get confusing) and Sowndariya Dhiyaneeswaran (as a fellow Tamilian, I'm probably the only one within DARE who can spell your name correctly). You guys have made such wonderful team leaders within my tenure at PRG. To all the other members I've had the pleasure of knowing within PRG. Thank you for all the great conversations we've had this far. Finally, to the new members who make up the current PRG team, I've got only three words for you.

De Ad Terra.

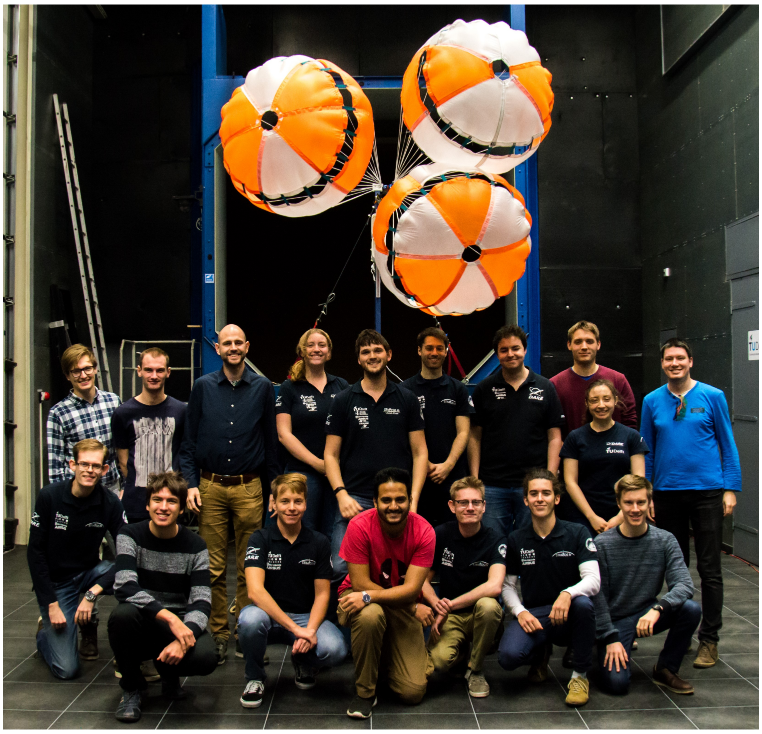

Abstract

The society of Delft Aerospace Rocket Engineering (DARE) aims at launching the Stratos IV sounding rocket to an apogee of 100km; thus cementing their place as one of the few student teams that have had the unique opportunity to design and build a rocket that is capable of reaching the frontiers of space. In doing so, DARE has entered flight supersonic regimes during atmospheric entry. With the development of cryogenic engines in the pipeline, future DARE missions look at reaching the hypersonic velocity regimes resulting in the current cork and carbon fibre composite heat shield design becoming redundant. Thus, hypersonic flight brings with it the challenge of designing new a heat shield; capable of withstanding the elevated temperatures.

Alginate and montmorillonite nanoclay based biopolymer nanocomposites have become a well-researched topic in recent years. This stems from the ability of the nanoclay fillers to align themselves within the suspension to mimic natural materials such as nacre (mother of pearl). The alignment of the nanoclay not only reinforces the biopolymer to provide a high storage modulus but also provides a tortuous path for transport phenomenon such as diffusion to take place; thereby making them flame retardant.

In their native state, the nanocomposites are film-like and offer limited viability. But, simple production practices may be borrowed from culinary disciplines to transform the nanocomposites into foams with different relative densities. The introduction of the gaseous voids should further heighten the thermal characteristics; allowing them to function as heat shields. However, in transforming the nanocomposite to a foam, little is understood about the impact it will have on the mechanics of the native nanocomposite. As multiple analytical and numerical models have been provided over the years to estimate the mechanical properties of foams, a careful assessment of the various literature sources becomes necessary. Once a suitable model is identified, a detailed experimental campaign can be carried out to characterise the biopolymer nanocomposite foams mechanically.

Keywords: Biopolymer Nanocomposites, Foams, Heat Shields, Relative Density, Mechanical Characterisation

Contents

List of Figures

List of Tables

Chapter 1

Introduction

The society of Delft Aerospace Rocket Engineering [1] (DARE) is a motivated student group that looks at providing young engineers with the opportunity to conduct research in the multidisciplinary field of rocket science. By providing students with a hands-on approach, it helps them push past their theoretical bounds and allows their concepts to turn into fruition. Whilst the research conducted within DARE is indeed multifaceted, the holistic aim of the society over the last nineteen years has been to become one of the few student groups that realise their dream of reaching space. To that effect, the flagship project within DARE, titled Stratos, is focused on developing a launch vehicle that has the capacity to carry a small scientific payload and cross the Kármán line (100 km altitude) to reach the frontiers of space.

Over the last nineteen years, multiple sounding rockets have been built to achieve Stratos's aim. Whilst the record-breaking Stratos I and Stratos II+ rockets were successfully launched to altitudes of 12.5 km and 21.5 km respectively, the Stratos II and Stratos III rockets have had issues of their own; thereby leading to the unfortunate failure of their respective missions. However, the society looks at collectively capitalising on the lessons learnt from each one of these launches and has decided to launch the Stratos IV rocket in the year 2021. This rocket looks at finally achieving the single, most important aim of DARE as a whole and is expected to cross the Kármán line to reach the frontiers of space.

Whilst it may seem sufficient to launch a rocket into space and achieve a somewhat lifelong dream, there still remain additional and equally important challenges to worry about. The nosecone section of the rockets houses critical flight electronic systems as well as flight data that is worth recovering. And so; the Parachute Research Group (PRG) was established within DARE for this very reason. By constantly conducting research in the field of recovery, PRG has been able to successfully develop recovery modules for the

Stratos missions. Although extensive development has led to PRG designing parachutes and deployment systems capable of withstanding supersonic flight regimes, the design of the heat shield to protect these systems from aerothermal heating during atmospheric entry remains relatively simple. The current heat shield is essentially a composite panel that is made up of Carbon Fibre Reinforced Polymer (CFRP) and cork. Whilst the CFRP provides the heat shield with the required structural stiffness, the thermal characteristics of cork allow it to withstand the high-temperature environment and helps the recovery module cope with the harsh conditions of atmospheric entry. During initial testing, the design of the current heat shield seemed sufficient for the Stratos IV rocket. However, with the advent of cryogenic propulsion for future DARE missions, the scope of the current heat shield seems limited. To help illustrate why this is indeed the case, the subsequent sections of this Chapter look at providing the reader with the recovery flight regime of the Stratos IV rocket, the challenges associated with cryogenic propulsion and the means by which these very challenges can be troubleshot.

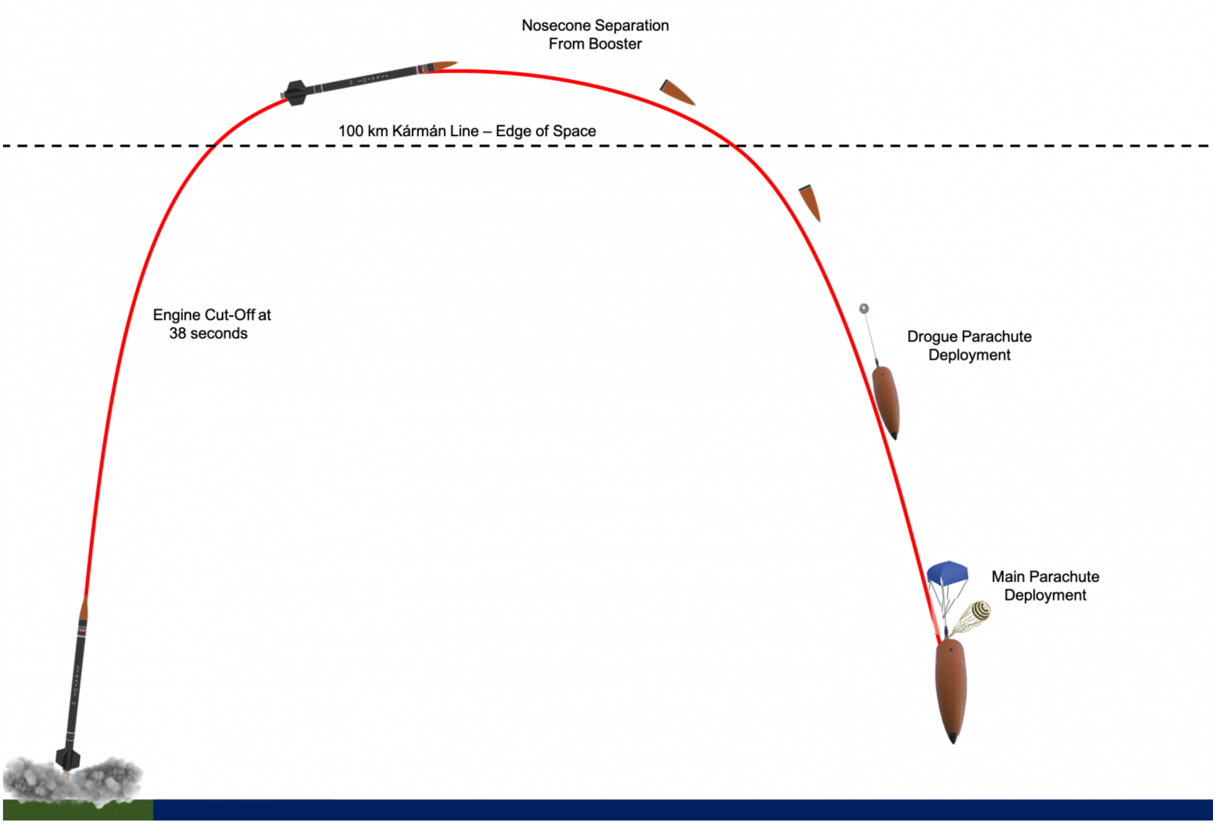

Figure 1.1: Stratos IV Mission Path [1]

1.1 Recovery Flight: Stratos IV and Beyond

Fig. 1.1 depicts the overall mission of the Stratos IV rocket. The recovery phase of the mission begins once the nosecone of the rocket has successfully separated from the booster stage. Upon separation, the nosecone is susceptible to a tumbling motion during the atmospheric entry phase due to gyroscopic precession. Once sufficient pressure conditions have been achieved during descent, a drogue parachute, capable of withstanding velocities of up to Mach 3 is deployed from the recovery module of the nosecone (opposite end of vertex) to slow it down. However, as the density of the atmospheric layers increases consistently during entry, the nosecone is exposed to ever-increasing drag forces. The effect of these drag forces during supersonic entry leads to shock wave formation. These shock waves further lead to a phenomenon called aerodynamic heating and hence, the development of an elevated temperature profile over the surface of the nosecone stage [12]. Whilst the exact temperature that can potentially develop is dependent on the tumbling motion of the nosecone, if no change in orientation is achieved for timescales below a hundred seconds, temperatures between 100 and 500 °C are to be expected (based on preliminary simulations conducted by DARE). Whilst these temperatures can be sustained by the aramid lines of the drogue parachute, they cannot be sustained by the nylon lines of the main parachutes and hence, the heat shield that protects the outer surface of the recovery module before drogue deployment becomes a requirement.

The Stratos IV rocket uses the DHX-400 Nimbus hybrid rocket engine that makes use of a liquid oxidiser and a solid rocket fuel. However, for future missions, DARE looks at integrating a rocket engine that relies completely on cryogenic propulsion [1]. It becomes important to highlight the implications cryogenic propulsion has on the recovery flight. Assuming that a rocket engine is built to the same thrust specifications as that of the current hybrid engine, the cryogenic engine can then be expected to have a higher specific impulse. What this means is that if the same mass of fuel is supplied to both engines, the cryogenic engine will be able to sustain the same thrust for longer periods of time as compared to the hybrid engine. As a consequence of Newton's third law, this would mean that the rocket can now achieve greater velocities. Although the exact velocities that can be achieved is not known, it is expected that the rocket will at least be propelled at velocities greater than its current velocity. This would propel the rocket into the near-hypersonic/hypersonic velocity regime (greater than or equal to Mach 5). Given that the mission strategy during the entry phase is not expected to change much, atmospheric entry upon separation will now take place at much higher velocities. This would mean a further elevation in temperatures. For the timescales that were stated earlier, it is now expected that the temperature of the heat shield will consistently lie between 500 °C and 1000 °C (again based on preliminary tests conducted by DARE).

Owing to the thermal properties of commercially available cork [13], it could still be used as a heat shield for supersonic entry. However, since drag forces scale quadratically with an increase in velocity, the hypersonic velocities would demand a heightened thermal insulation performance from the heat shield. As cork is a naturally available material that offers limited scalability in its design, it would mean that either a thicker slab of cork could be used or, a slab of cork that is coated with an additional thermally insulating layer be used. In either case, the limit on scalability forces the mass of the heat shield to go up. This is not a desirable outcome in the field of rocket science. And so; the demands of hypersonic flight bring with them the requirement for a new heat shielding material.

1.2 Biopolymer Nanocomposites

Whilst a multitude of materials exists to be utilised as a heat shield, there are still some key characteristics that are desirable for the application at hand. As mentioned above, it is still desirable to keep the mass of the material as low as possible. In order to preserve the current production technique, it is important that the new material be integrable within a sandwich structure. Additionally, it is important that in case the material ablates, it still retains a good portion of its stiffness to preserve structural integrity and produce a char layer that is resistive to aerodynamic shear forces [12]. As DARE is a student team, it is also important that the cost of the material is kept as low as possible. Some additional constraints include ease of availability, handling and production.

Intensive research on composite materials has promoted the development of polymer nanocomposites for a number of applications [14–18]. Unlike conventional polymer composites, the thermal and mechanical properties of the nano-sized fillers in conjunction with other characteristics such as high aspect ratio and a high degree of ordering at the nanoscale has led to the development of macro-scale materials with very desirable properties. In his PhD thesis [2], Zlopaša talks about the utilisation of the sodium alginate biopolymer in conjunction with montmorillonite (MMT) nanoclay fillers to facilitate the production of a biopolymer nanocomposite. By utilising an affine deformation technique to yield nanocomposite films from a suspension, he was able to synthesize films with exceptional ordering at the nanoscale (Fig. 1.2). As a consequence, the composite benefited from the creation of tortuous paths within its structure. These paths act as a physical barrier for transport phenomena such as diffusions. This, in combination with the low thermal conductivity of the polymer, has depicted great flame retarding capabilities even for very small thickness (Fig. 1.3). Additionally, the high ordering in combination with the inclusion of a much stiffer nanoclay filler has led to the development of biopolymer nanocomposites with a storage modulus between 10 GPa and 30 GPa, based on the loading concentration. It has also been observed, that even at elevated temperatures this modulus value is retained above the 10 GPa mark for certain weight concentrations of MMT clay in sodium alginate (Fig. 1.4).

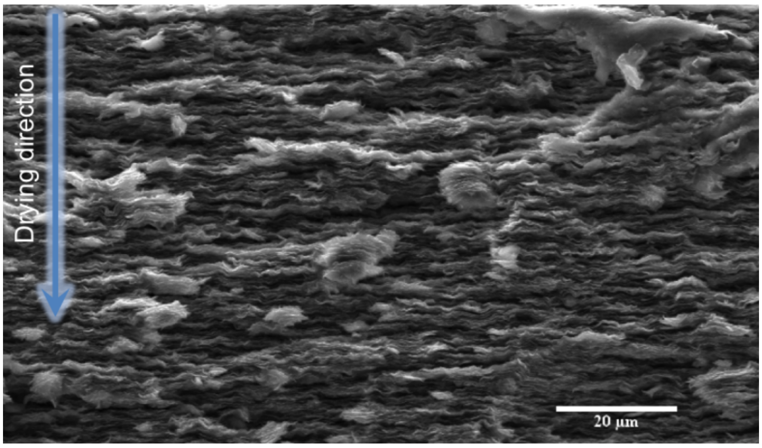

Figure 1.2: Nanoscale ordering observed in sodium alginate - MMT clay (50% wt.) nanocomposites ; ESEM micrograph [2]

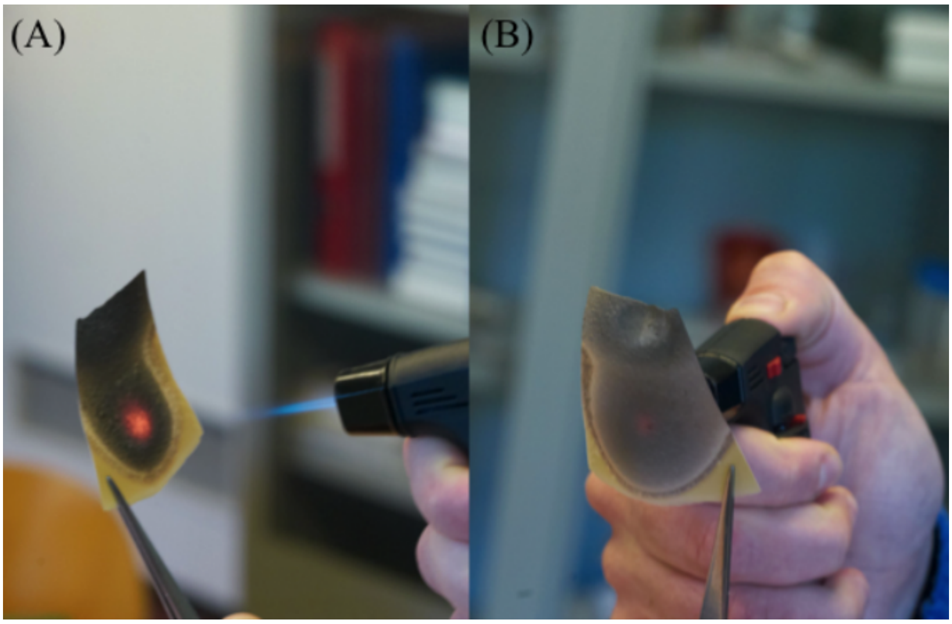

Figure 1.3: Flame retardancy exhibited by an 80μm thick sodium alginate - MMT clay (80% wt.) nanocomposite film [2]

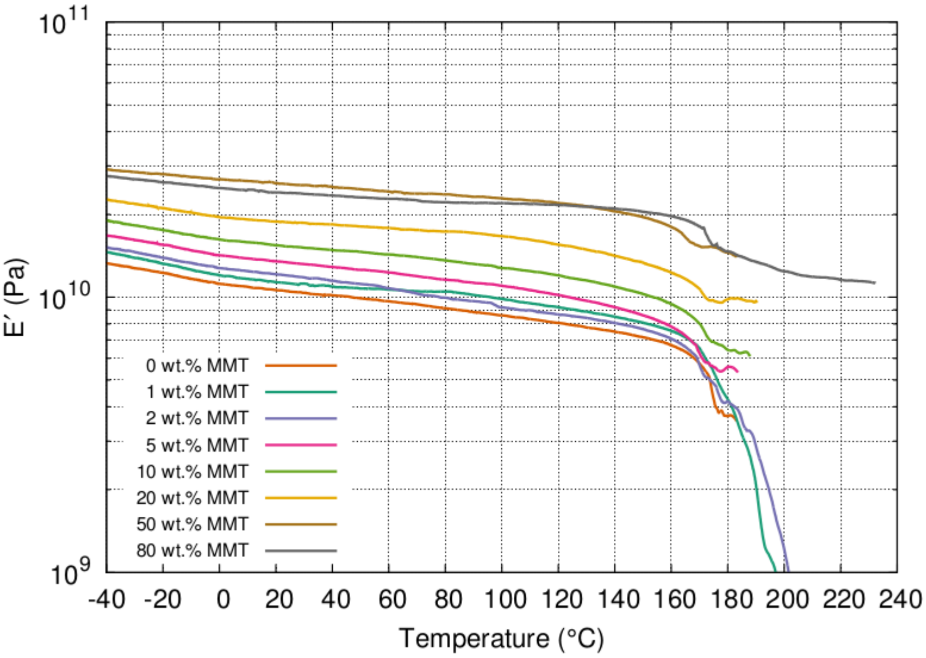

Figure 1.4: Storage modulus as a function of temperature for different nanoclay conc. [2]

Whilst these properties only answer a portion of the requirements that are expected from the heat shield, by turning the biopolymer nanocomposite into a cellular solid such as a foam, it is possible to meet all the criteria set for the heat shield. Owing to the fact that foams are lighter than their parent phase material, the density of the heat shield is further dropped. Not only this, as the gas phase tends to occupy a greater volume fraction in low density foams, a further decrease in the thermal conductivity can be expected. Thus, by opting to design a biopolymer nanocomposite foam, it is possible to create a sustainable product that looks at setting a new benchmark for applications concerning thermal insulation.

1.3 Outline of Thesis

Although the aim is quite clear, i.e. to create a foam(s) whose cell structures are made using a biopolymer nanocomposite, it is important to understand how successfully these foams can be produced, whether there is a direct translation of the nanocomposite's flame retarding capabilities to the foam and more importantly, what are the mechanical properties that can be established for the foam. The following chapters look at covering those topics in that particular order; with references being made to relevant literature sources, important questions being formulated along the way and the extent to which theoretical and experimental work was carried out.

Chapter 2

Foam Production

To understand how biopolymer nanocomposite foams can be produced, it became important to understand the techniques that were prevalent in literature [3, 19–23]. More importantly however, the property of foam materials stems from one important parameter called the relative density:

$$\rho_{rel} = \rho^* / \rho_s \tag{2.1}$$

ρ^* here represents the density of the foam material and ρ_s represents the density of the solid material that makes up the solid structures within the foam. In the subsequent chapters, it shall be shown how the relative density can be used to describe the thermal properties and more importantly, the mechanical properties of the biopolymer nanocomposite foams. For now, however, it helps to understand how foams of different relative densities may be produced.

2.1 Trends in Production

The polymers traditionally used to make foams do not exhibit volatility. This prompts the need for using a foaming agent that facilitates the entrapment of the gas phase. Broadly speaking, there are two types of foaming agents. Physical foaming agents employ the use of an irreversible phase change mechanism to trigger the nucleation of the gas phase. In most cases, this is as simple as saturating the polymer matrix with the desired gas under high pressure and subsequently releasing the pressure to allow the gas to expand in volume. Chemical foaming agents on the other hand prompt an exothermic reaction that facilitates the release of gas. Owing to the challenges imposed by the creation of unwanted side products, most commercially available foams make use of a physical foaming agent. This trend has also stuck with the production of nanocomposite foams.

Unlike traditional polymeric foams, the inclusion of the nanoclay in nanocomposites reduces the surface energy for gas nucleation and hence, the voids begin to expand heterogeneously [22]. As a consequence of the heterogeneous nucleation, newer voids are not formed within the polymer matrix over time and; the size of the voids consistently grow to occupy a uniform size in the final foam. This provides a controllable way of producing the foams. With the help of an easily recyclable, low cost and stable supercritical fluid, high levels of solubility can be achieved within the polymer nanocomposite suspension. This has prompted the utilisation of supercritical CO_2 in foam production. Additionally, this goes hand in hand with large scale foam manufacturing processes such as extrusion. Fig. 2.1 illustrates the morphology of the foams that yield from the utilisation of an extrusion technique; in this case to produce polystyrene - MMT clay foams with the help of supercritical CO_2.

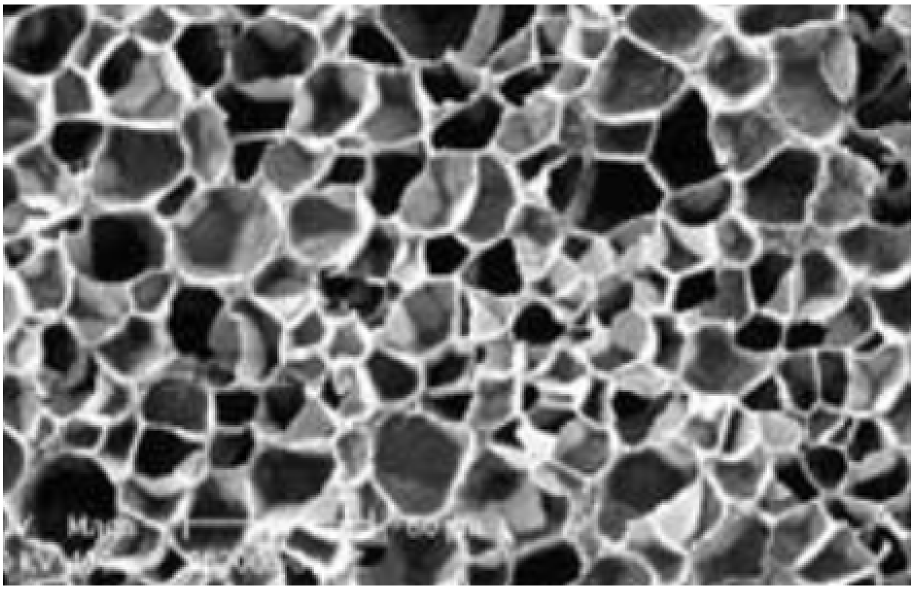

Figure 2.1: Morphology of Polystyrene - MMT clay (5% wt. conc) nanocomposite foam; SEM image; avg. cell size : approx. 25 μm [3]

On paper, it may seem simple to adopt the production techniques/methods that have been discussed in literature. However, the utilisation of an extrusion machine that makes use of pressurised supercritical gas to make lab-scale samples is not feasible. In an attempt to make heat shielding foams, the idea is to easily produce small quantities of the foam with a simple manufacturing technique. Additionally, commercially available foams show only 5-10% variability in their relative density values. This is often a result of the limitations posed by a specific manufacturing technique. An investigative study, that is aimed at understanding the underlying trends in mechanical and thermal properties as a function of the foam's relative density is crippled by adopting a single manufacturing technique.

2.2 Alternate Strategies

Fortunately, the utilisation of a polysaccharide-based biopolymer like alginate provides the versatility to test foaming techniques that are adopted in culinary disciplines. A few of these well-known practices that pose relevance to this study have been mentioned under the headings that follow.

2.2.1 Baking

Over the centuries, the use of leavening agents whilst cooking baked goods has become a popular choice. The idea has been to convert the initial dough mixture into a lighter solid by aiding the formation of voids within the mixture (Fig. 2.2). Leavening agents such as baking soda or baking powder rely on the facilitation of a spontaneous acid-base reaction that leads to the release of gases like CO_2. Upon elevating the temperature, these gases expand leading to the formation of voids. Whilst multiple variables such as baking temperature, baking time, the acidity of mixture and concentration of leavening agent control the relative density of the foam, a parametric study can yield an ideal baking strategy to produce the foam. If the baking technique can be mastered, it provides a simple strategy to produce foams with different dimensions.

Figure 2.2: Baked sponge cake [4]

2.2.2 Freeze Drying

Traditionally, biopolymer nanocomposites are produced by mixing and subsequent drying of the biopolymer solution and clay suspension. However, if the mixture were frozen instead of being dried, it will prompt the nucleation of ice crystals within the final suspension. When a vacuum pump is used to reach the triple point of the ice phase in the suspension, the ice has the ability to sublimate. Upon sublimation, the space occupied by the ice crystals is now occupied by voids thus forming the foam. This method also called freeze-drying (Fig. 2.3), allows precise control over the density of the foam that can be produced. This is because the solid content in the suspension is what characterises the ultimate solid mass in the foam. However, in order to gain better control over the rate of nucleation of the ice crystals, an additional compound may be added into the solution. In the case of biopolymers, it has been observed in small studies not documented in the literature, that ethanol can indeed provide the much-needed stability to the system. This already provides a vital starting point worth investigation.

(a) Freeze dried food flown on Apollo 11 [24]

(b) A freeze dryer that is used for scientific purposes [?]

Figure 2.3: Freeze drying

2.2.3 Whipping

Whipping is the process of physically incorporating a gas phase into a polymer gel solution. When done successfully, uniform void distribution can be achieved within the gel whilst not compromising on the structural integrity of the gel itself. Whilst traditional whipping is done by mechanically entrapping the gas, modern-day whipping strategies involve the dissolution of the gas (usually CO_2 or N_2O) within the gel with the help of pressurised whipping siphons (Fig. 2.4). Because the initial phase is a gel solution, the structural integrity of the foam is governed by the storage modulus of the gel. In the case of biopolymer nanocomposites, cross-linking may be facilitated using known cross-linking agents to increase the structural integrity within the gel. Upon subsequent drying of the solution, the excess moisture can be removed thereby leaving behind the nanocomposite to form the solid structures within the foam. The relative density of the whipped foam is only governed by the amount of gas entrapped within the gel solution. Also, it still preserves the utilisation of a simple production technique. The other advantage this method poses is that it preserves the utilisation of a gas phase alongside a physical foaming method as favoured in literature.

(a) Cream that is whipped without a siphon [25]

(b) Cutaway diagram of a whipping siphon; E: foaming nozzle, F: whipped foam, H: gas cartridge [?]

Figure 2.4: Whipping, with and without a siphon

2.3 Methodology

Throughout the span of this production study, the type of sodium alginate (Na-Alg) and nanoclay used were kept consistent. Bomalgin (Na-Alg) which is produced by Ranie Chemie and CEBOGEL (nanoclay) which is produced by Cebo International, were used to produce the nanocomposite foams. In all cases, the weight fraction of (0.5:0.5) was kept consistent between the Na-Alg and the nanoclay. This was done in an effort to emulate the highest possible storage modulus from Zlopaša's work (Fig. 1.4). Conventionally, nanocomposite films are produced by separately stirring suitable wt. concentrations of Na-Alg solution and nanoclay suspension for extended periods of time (typically 24 hours) and then mixing the suspension into the solution to obtain the desired wt. fractions. However, since the topic of interest here remains foams and not films, the technique adopted was modified to suit the individual foam production techniques. These are outlined in great detail in the subsections that follow.

2.3.1 Baking

Dough Preparation

Analogous to conventional baking, the idea was to produce a suitable dough-like mixture that could then be treated in the oven to produce the final foam. To that effect, the process began by uniformly mixing all the dry powders together and then adding deionised water in batches until a kneadable dough of desired consistency was obtained. As mentioned earlier, conventional baking techniques utilise leavening agents that facilitate an acid-base reaction and thus, the release of carbon dioxide gas. However, with regards to nanocomposite foams, the formation of side products was undesirable and needed to be mitigated. Hence food grade ammonium bicarbonate that readily dissociates to form ammonium ions and carbon dioxide gas at elevated temperatures was used as a leavening agent. It was understood that the ammonium ions would readily dissolve in the water and escape the system upon heating. Although not directly stated in literature, the utilisation of no more than 10% of the dry mass as the leavening agent in the prescribed as the pseudo standard when it comes to conventional baking. And so, a dry mass wt. frac of 0.45-0.45-0.1 of Na-Alg, nanoclay and ammonium bicarbonate respectively was preserved for all baked samples. Again, analogous to conventional baking, a dough mixture that stops clumping was considered as the desired end result. To understand the wt. fraction at which the water content became sufficient to stop the clumping, the water was added in batches. It was noticed that at 50% wt. frac. (w.r.t to the total dough mass), the dough was kneadable and thus, an equal mass of the dry powder mixture was mixed with water and kneaded into a consistent dough. The dough was then shaped on a flat surface to suit the dimensions that were desired.

Times and Temperatures

To understand the effect of temperature and more importantly the effect of temperature profiles within the sample, a conventional hot air recirculation oven was used in conjunction with a microwave oven to produce the final foams. It is a known fact that Na-Alg is likely to exhibit signs of degradation at higher temperatures [2]. Thus, in the case of a hot air recirculation oven, the samples were baked at temperatures of 120, 140 and 160 °C. In the case of the microwave oven, the temperature was kept constant at 140 °C, but wattages of 250, 500, 750 and a 1000 W were trialled. As the ideal baking time was unknown at the start of the study, this also became a variable worth consideration. Hence, in the case of the hot air recirculation oven, three different baking times were trialled for each temperature. 1, 1.5 and 2 hours. As it was understood that more uniform heating can be sought using the microwave oven, the baking time was restricted to only 2 mins.

Control over Drying

In the case of baked foams, the actual foam morphology resides beneath the surface of the baked product. However, the low thermal conductivity of the polymer leads to the formation of a large temperature flux on the surface. This residual heat can lead to a non-uniform departure of water vapour from the system and can leave the surface susceptible to cracking due to constriction. Since the non-uniform heating was expected to occur in the hot air recirculation oven, additional samples were prepared. But now, either the entire sample was wrapped with aluminium foil or the top and bottom surface of the sample were covered with a suitable insulating material such as silicone or paper. This was done in an effort to contain the water vapour within the sample. Since there was no proven technique to understand which combination of containment techniques would work well, they were solely based on the intuition gained by baking each sample. Additionally, to understand if plasticising agents would help overcome this problem, even more, samples were made with known plasticising agents. This was done in an effort to create a continuous network within the polymer that would mitigate crack propagation. In these cases, the water used to make the dough was replaced by a plasticising agent solution. They are as follows: 30% wt. glycerol, 30% wt. ethylene glycol, 30% wt. isopropanol and 15% wt. butanol. The concentrations for these solutions were based on their solubility limit in water. Additionally, combinations of these plasticising agents were also trialled. But again, the combinations were based solely on the knowledge gained from baking individual samples. In the cases were a plasticiser was used, the baking temperature was changed suitably to kerb the risk of volatilising the plasticising agent. In the case of glycerol and ethylene glycol, it was 120 °C and in the case of isopropanol and butanol, it was 70 °C. In the case of plasticised samples as well, the surfaces were again covered with insulating materials as a precautionary step.

Finally, once the baked samples were removed from the oven, they were inspected for quality. In case the samples yielded a desirable morphology purely from visual inspection, they were subsequently dried either using a well ventilated (Temperature = 22 °C, Relative Humidity = 50%) fume hood, or overnight ($\sim$ 15 hours) at a suitable temperature using the hot air recirculation oven or desiccated over silica gel. The choice here was based solely on the amount of moisture that was still retained within the sample.

2.3.2 Freeze Drying

Suspension preparation

As mentioned earlier, the solid wt. fraction of the suspension is what characterises the relative density of the final foam. Since multiple concentrations could be made by diluting a high concentration suspension, a method best suited to prepare high concentration suspensions was deemed necessary. Whilst a theoretical limit on the concentration doesn't exist, it was physically observed that at around 10% wt. concentration, the suspension loses out on its tractability. However, at such high concentrations, it becomes physically impossible to stir the suspension using a magnetic stirrer. To that effect, two different methods were adopted.

The first method involved the utilisation of a Janke and Kunkel RW20 overhead stirrer. The stirrer was suitably fitted with an impeller blade to stir the high concentration suspension. The stirring process began by first filling a polypropylene beaker with the desired amount of deionised water. Next, the beaker was suitably positioned underneath the stirrer such that the impeller blade remained a few millimetres above the bottom surface of the beaker. The stirring device was then turned on and the suspension preparation began by initially dispersing the nanoclay in the water. Care was taken to add the nanoclay in batches and wait until it was uniformly suspended. Once this was done, the Na-Alg has then added in small batches again to the clay suspension. This was done until no large-sized chunks of Na-Alg were noticeable in the suspension. The suspension was then left stirring for roughly another hour to further aid uniform distribution. Throughout this entire process, the speed of stirring was influenced based on the viscosity of the mixture. As the viscosity kept increasing, the speed of stirring was dropped to aid vibrational stability whilst stirring. This reduction was not done to a prescribed value, rather it was done until stability was noticeable visually. Once the stirring was complete, the beaker was sealed using laboratory film and refrigerated overnight for roughly 15 hours at 4 °C, to aid the alignment of the nanoclay within the suspension. Once it was taken out, it was stirred again using a glass rod for about a minute. It was then cast into silicone moulds or Petri dishes for further drying. In order to cast lower concentration suspensions, the 10% wt. concentration was first diluted to 2.5% and 5% wt. suspensions before being cast similarly.

The second method involved the utilisation of a handheld scraping tool typically intended for making confectionery. The suspension preparation began by first weighing suitable masses of dry constituents, mixing them thoroughly to form a uniform mixture and spreading it over a glass plate. Next water was slowly added in batches and the clumps that resulted were broken down consistently to yield a homogeneous suspension. Care was taken to ensure that the water did not exit the confines of the plate as this would lead to a deviation from intended concentration. Once the desired suspension concentration was reached, the suspension was then transferred to a glass beaker, sealed using laboratory film and refrigerated overnight for roughly 15 hours at 4°C, to aid the alignment of the nanoclay within the suspension. To understand the influence the size of the dispersed particles had within the suspension, two such suspensions were prepared and stored. One in which a consistent amount of time was spent to ensure that all the large-sized chunks were broken down successfully; and the other in which the presence of small-sized particles, roughly a few hundred micrometres thick, was considered acceptable. Finally, the samples were again cast into silicone moulds or Petri dishes for further drying. Only the 10% wt. the suspension was prepared using this method as the primary objective was to understand the effect that the texture of the suspension had on the final result. As the likelihood of larger sized particles being present was relatively higher in the 10% wt. suspension, only it was used to cast these samples.

Freezing + Drying

To understand the role that ice nucleation rate had on the morphology of the foam, two different drying strategies were adopted. In the first method, the samples were frozen at -80 °C for roughly 30 minutes to aid ice crystal nucleation within the sample. The samples were then transported to the freeze dryer for the drying step. The drying was performed using a Christ Alpha 1-4 LDplus freeze dryer. It was performed at a set temperature of -60 °C and at a set pressure of 5 Pa. To aid successful drying of the samples, the samples were dried for a period of roughly 15 hours. This was the standard protocol established for freeze-drying.

In the second method, Liquid Nitrogen was used to flash freeze the samples. This was done in an effort to create multiple rapid nucleation sites within the sample. To further aid this type of crystal growth, water that was used to prepare the suspension was replaced with a 5% ethanol solution. The ethanol was expected to bond with the water molecules in an attempt to retard the growth of the ice crystals. However, since the ethanol was volatile enough, it would also exit the system upon subsequent drying. The suspension was the first cast into Petri dishes. It was then slowly submerged into a bowl-shaped dewar flask containing liquid nitrogen until no more bubbling was noticeable on the surface of the sample. The sample was then frozen at -80 °C for 30 minutes to minimise the large increase in temperature during drying. The drying was again performed in a fashion similar to the one stated above.

2.3.3 Whipping

The process for whipping began in a fashion similar to the one used for freeze-drying. The suspension was again prepared using mechanical stirring. However, since whipping siphons are built to accommodate dilute solutions/suspensions, a 5% wt. the suspension was prepared in place of a 10% wt. suspension.

It was decided to gel the solution by replacing a fraction of the Na^+ ions in the Na-Alg with Ca^{2+} ions. This would aid cross-linking between the carboxylic groups of the alginate biopolymer. However, if the Ca^{2+} ions were readily available in the suspension, the cross-linking would take place instantaneously, thereby limiting the potential for foam processability. Thus, calcium carbonate ($CaCO_3$) was identified as a suitable salt as a virtue of its low solubility in neutral pH solutions. However, upon changing the pH to a slightly acidic medium (pH $\sim$ 5), it would start dissolving to facilitate the slow release of Ca^{2+} ions. Once the 5% wt. the suspension was made, $CaCO_3$ from Sigma Aldrich was added to the suspension and stirred again for a period of 30 mins to disperse it within the suspension. The mass of $CaCO_3$ needed was arrived at from stoichiometry. Since the Ca^{2+} has an additional positive charge compared to the Na^+ ion, each Ca^{2+} would replace two Na^+ ions in the alginate biopolymer. However, the mass of the $CaCO_3$ is approximately 46% ($\sim$ 50%) the mass of the Na-Alg, and thus, 0.25 times the mass of Na-Alg in $CaCO_3$ was dispersed within the suspension.

A 250 ml capacity iSi whipping siphon was used to produce the foams. The container was initially filled with 100 ml of the suspension mixture. It was then topped up with an equal volume of food grade carbonic acid solution which had a HCO_3^- ion concentration of 18 mg/l. The carbonic acid solution was added to facilitate the desired reduction of pH within the suspension. The container was then quickly sealed and charged with CO_2 gas. The charging was done using the standard soda chargers (volume = 10 ml, net mass = 7.5 g) that are available for the siphon mentioned above. Only a single charger was used as this was the prescribed gas pressure for the siphon. Once charged, the contents of the siphon were shaken thoroughly for 30 seconds to promote uniform mixing and gas dissolution. The foam was then whipped into a petri dish and set aside for 30 mins to aid the cross-linking within the alginate biopolymer.

At this stage, although the samples yielded cross-linked foams, it was necessary to ensure that sufficient cross-linking could occur within the sample to help retain the structure of the foam upon subsequent drying. However, since the porosity was already produced within the gel by this stage, instantaneous cross-linking could be carried out using readily dissolvable calcium salts. Thus, a 1% wt. solution of Sigma Aldrich based Calcium Chloride ($CaCl_2$)s was prepared for this very purpose. The petri dish containing the cross-linked foam was dipped into a shallow bath containing the $CaCl_2$ solution for 1.5 hours, such that only the top surface of the foam remained immersed beneath the solution and not the entire petri dish. This was done in an attempt to control the rate of diffusion within the sample and prevent drastic dimensional changes due to shrivelling. Once the salt bath treatment was concluded, the excess solution was emptied out of the petri dish whilst carefully preserving the structural integrity of the cross-linked sample.

The only step that remained was the drying of the samples. However, as a low relative density was expected within the samples ($< 2.5\%$), it would result in the evaporation of a majority of the sample's original mass. This rapid change in surface energy would result in a large scale contraction of the foam and a collapse of the foam's structure. In order to yield a more successful drying procedure, two different strategies were adopted. The first strategy involved the utilisation of the same Christ Alpha 1-4 LDplus machine that was used for the freeze-dried samples. However, the drying time was extended to a period of 24 hours to account for the lower solid wt. frac. within the whipped samples. The other strategy involved the use of isopropanol and substituting it in the place of water within the samples osmotically. Since isopropanol is a non-solvent, the cross-linked biopolymer would reject it readily, thereby allowing it to vaporise. However, since it possesses a smaller surface tension than water, rapid loss in mass by vaporisation would still result in surface energy that is fairly constant throughout the entire drying process. To carry out drying using isopropanol, the Petri dishes containing the samples were consecutively immersed for 15 mins in beakers containing 5, 10, 20, 40, 80 and 100% wt. isopropanol solutions. The resulting sample was then dried ambiently in a well-ventilated fume hood (Temperature = 22 °C, Relative Humidity = 50%).

2.4 Results and Discussions

In reality, a large number of samples were prepared by trial and error and thus, the effects of changing the parameters that influenced each production technique was studied. For the purposes of this report, the samples that were successfully prepared have been documented in this section. Success, in this case, was attributed to the homogeneous morphology within the sample upon visual inspection alone. For the benefit of the reader however, all the samples that were prepared over the course of this study have been consolidated in Appendix 7.2.

It should also be noted that the successful samples were intended for future characterisation. Hence, they were post processed to yield circular disks of relatively uniform thickness and morphology. Although additional details are provided in Chapter 6 to explain how this post-processing was carried out, for the ease of interpretation, the diameter of the samples listed below are between 20 and 25 mm.

2.4.1 Baking

The successful samples that the baking process yielded have been documented in Table 2.1. It is clear from this table that in the temperature window between 120 °C and 140 °C, ammonium bicarbonate retains its ability to function as a leavening agent. However, as the temperatures are not too high, the rate of evaporation of water from the sample wasn't critically high enough to cause large cracks developing within the samples (Figs. 2.5, 2.6 and 2.7). Additionally, as efforts were made to contain the rate of evaporation by covering or wrapping the samples with various insulating material (silicone/paper) or aluminium foil respectively, the water loss was much better controlled and also resulted in mitigation of large cracks within the sample.

The utilisation of glycerol and ethylene glycol as plasticising agents also suggestively yielded foams without cracks. However, as noticeable from Figs. 2.8, 2.9 and 2.10 the inability of the Na-Alg to dissolve within these plasticising agents results in a more rougher morphology within the foam. Upon inspection, it was also noticed that the plasticisation had resulted in more ductility within the sample. Whether this increase in ductility was accompanied by a considerable drop in the modulus was worth understanding during the mechanical characterisation tests.

Finally, the utilisation of microwaves not only drastically reduced the production time as intended but also resulted in the mitigation of non-uniform heating within the sample. In terms of morphology, the use of the microwaves resulted in larger void formation within the sample (Figs. 2.11 and 2.12). It was noticed that when the input power was further increased beyond 500 W, these larger voids were now responsible for the collapse of the sample.

2.4.2 Freeze Drying

The successful samples that the freeze-drying process yielded have been documented in Table 2.2. Almost intuitively, a progressive densification was noticeable, proportional to the initial mass concentration of the suspension (Figs. 2.13, 2.14 and 2.15). However, the results from the 10% wt. samples (Figs. 2.15, 2.16 and 2.17) seem to suggest that the initial method adopted to prepare the concentrated suspension has little effect on the final morphology of the foam. On the subject of morphology, it was clear that the refrigeration process was long enough to aid the formation of directional ice crystals within the suspension (Figs. 2.13, 2.15, 2.16 and 2.17). However, when flash freezing using liquid nitrogen was adopted as a mitigative strategy, it resulted in large cracks developing within the sample as a consequence of rapid cooling. Thus, only one sample could be obtained from the flash freezing strategy using liquid nitrogen (Fig. 2.18).

2.4.3 Whipping

Although the process adopted to produce whipped samples is rather drawn out with multiple parameters influencing the final density of the whipped samples, the morphology was solely dependent on the initial whipping step. Thus, the success of the whipping process was attributable to the most efficient drying step. Unfortunately, the use of isopropanol still led to large scale contraction within the samples. This is because, although the surface energy was greatly minimised during the drying step, the volatility exhibited by isopropanol resulted in contraction simply from the rate of mass loss within the sample.

This could be overcome by utilising a less volatile and bulkier non-solvent. However, this would mean utilising non-solvents that aren't readily miscible in water. And so, only one type of sample could be obtained by adopting the freeze-drying step. The resultant foam sample is depicted in Fig. 2.19.

Figure 2.5: Baked - 1

Figure 2.6: Baked - 2

Figure 2.7: Baked - 3

Figure 2.8: Baked - 4

Figure 2.9: Baked - 5

Figure 2.10: Baked - 6

Figure 2.11: Baked - 7

Figure 2.12: Baked - 8

Table 2.1: List of successfully baked samples

Sample ID	Composition (Wt. %)	Baking Process	Figure
Baked-1	22.5% Na-Alg + 22.5% nanoclay + 5% Ammonium Bicarbonate + 50% Water	1.5 hours @ 140 °C; Al foil - wrapped + overnight drying (∼15 hours) @ 70 °C; Al. foil - top and bot. + desiccation	Fig. 2.5
Baked-2	22.5% Na-Alg + 22.5% nanoclay + 5% Ammonium Bicarbonate + 50% Water	2 hours @ 140 °C; Al. foil - top & bot. + overnight drying (∼15 hours) @ 50 °C; Al. foil - top and bot. + desiccation	Fig. 2.6
Baked-3	22.5% Na-Alg + 22.5% nanoclay + 5% Ammonium Bicarbonate + 50% Water	2 hours @ 140 °C; Paper - top and bot. + drying @ 120 °C - 2hours + desiccation	Fig. 2.7
Baked-4	22.5% Na-Alg + 22.5% nanoclay + 5% Ammonium Bicarbonate + 15% Glycerol + 35% Water	2 hours @ 120 °C; Al. foil - top and silicone mat - bot + desiccation	Fig. 2.8
Baked-5	22.5% Na-Alg + 22.5% nanoclay + 5% Ammonium Bicarbonate + 15% Ethylene Glycol + 35% Water	2 hours @ 120 °C; Al. foil - top and silicone mat - bot + desiccation	Fig. 2.9
Baked-6	22.5% Na-Alg + 22.5% nanoclay + 5% Ammonium Bicarbonate + 12.5% Ethylene Glycol + 2.5% Glycerol + 35% Water	2 hours @ 120 °C; Al. foil - top and silicone mat - bot + desiccation	Fig. 2.10
Baked-7	22.5% Na-Alg + 22.5% nanoclay + 5% Ammonium Bicarbonate + 50% Water	Microwaved @ 140 °C, 250 W + desiccation	Fig. 2.11
Baked-8	22.5% Na-Alg + 22.5% nanoclay + 5% Ammonium Bicarbonate + 50% Water	Microwaved @ 140 °C, 500 W + desiccation	Fig. 2.12

Figure 2.13: Freeze Dried- 1

Figure 2.14: Freeze Dried - 2

Figure 2.15: Freeze Dried- 3

Figure 2.16: Freeze Dried - 4

Figure 2.17: Freeze Dried- 5

Figure 2.18: Freeze Dried - 6

Table 2.2: List of successfully freeze dried samples

Sample ID	Composition (Wt. %)	Drying Process	Figure
Freeze Dried-1	1.25% Na-Alg + 1.25% nanoclay + 97.5% Water	Mechanical Stirring + Refrigeration (-80 °C) + Drying @ 5 Pa, -60 °C	Fig. 2.13
Freeze Dried-2	2.5% Na-Alg + 2.5% nanoclay + 95% Water	Mechanical Stirring + Refrigeration (-80 °C) + Drying @ 5 Pa, -60 °C	Fig. 2.14
Freeze Dried-3	5% Na-Alg + 5% nanoclay + 90% Water	Fine Scraping + Refrigeration (-80 °C) + Drying @ 5 Pa, -60 °C	Fig. 2.15
Freeze Dried-4	5% Na-Alg + 5% nanoclay + 90% Water	Coarse Scraping + Refrigeration (-80 °C) + Drying @ 5 Pa, -60 °C	Fig. 2.16
Freeze Dried-5	5% Na-Alg + 5% nanoclay + 90% Water	Mechanical Stirring + Refrigeration (-80 °C) + Drying @ 5 Pa, -60 °C	Fig. 2.17
Freeze Dried-6	5% Na-Alg + 5% nanoclay + 5% Ethanol + 85% Water	Mechanical Stirring + LN2 (-196 °C) + Drying @ 5 Pa, -60 °C	Fig. 2.18

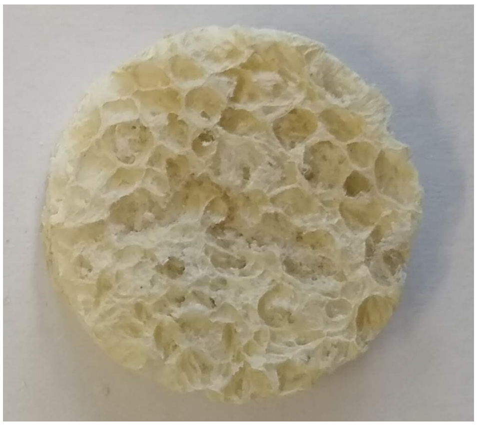

Figure 2.19: Whipped Sample

Chapter 3

Thermal Behaviour

So far, it has been possible to produce foams with different morhphologies and relative densities. The ability of these foams to retain the virgin biopolymer nanocomposite's flame retarding capabilities however, becomes important.

3.1 Thermal Conductivity of Foams

One would assume that the ideal starting point would be to characterise the foams for their thermal conductivity and thus, that it makes sense to turn to literature for providing a method by which this may be done. Gibson and Ashby [5] consolidated the efforts made previously [26–28] in estimating the thermal conductivity of a foam. As pointed out by them, the thermal conductivity of a foam can be estimated using the equation:

$$\lambda^* = \lambda_s^* + \lambda_g^* + \lambda_c^* + \lambda_r^* \tag{3.1}$$

Where λ^* represents the overall thermal conductivity of the foam, λ_s^* represents the conductive contribution made by the solid structures within the foam, λ_g^* represents the conductive contribution made by the gaseous phase within the foam, λ_c^* represents the convection that can occur within the cells of the foams and λ_r^* represents the contribution made by radiation through the entire foam itself.s

Upon approximating the cell walls as vertically flat plates, it is understood that for convection to occur due to the laminar flow of air (Grashof number > 1000), the dimensions of the cell walls would have to be in the order of ten millimetres [29]. However, for most commercially available foams used in engineering applications, the average cell wall size falls in the order of a few micrometres. Thus, the contribution made by the convection term is negligibly small and may be excluded from Equation 3.1.

To understand the contribution made by the remaining terms towards the overall thermal conductivity of the foam, Gibson and Ashby illustrated the results that were obtained for polymer foams as a function of their relative density (Figs. 3.1 and 3.2).

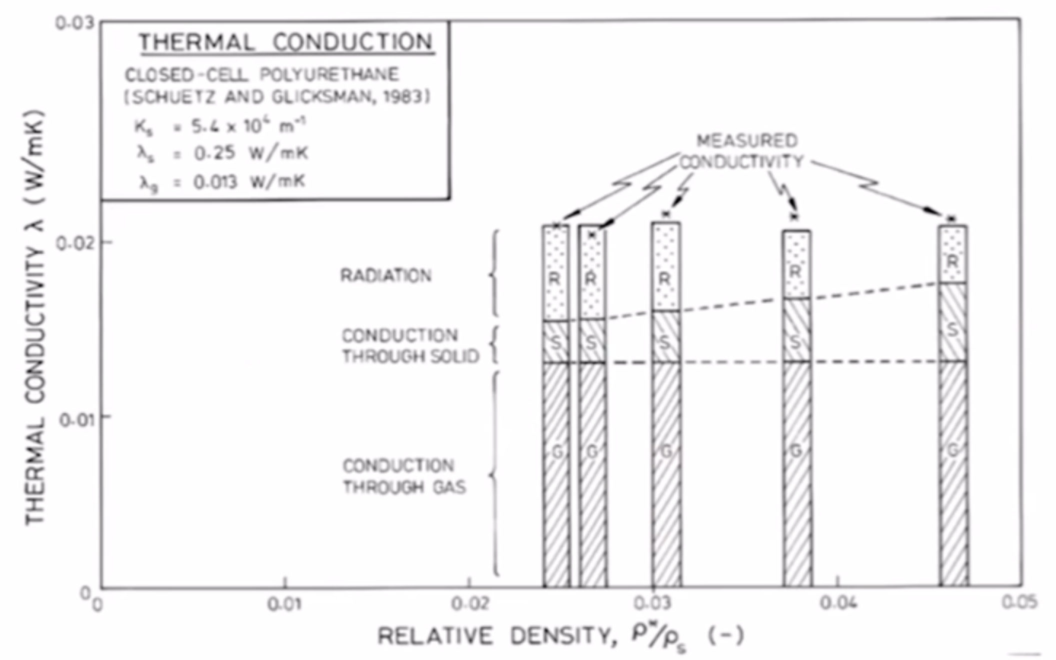

Figure 3.1: Contributions made by each mode of heat transfer towards the overall thermal conductivity [5]

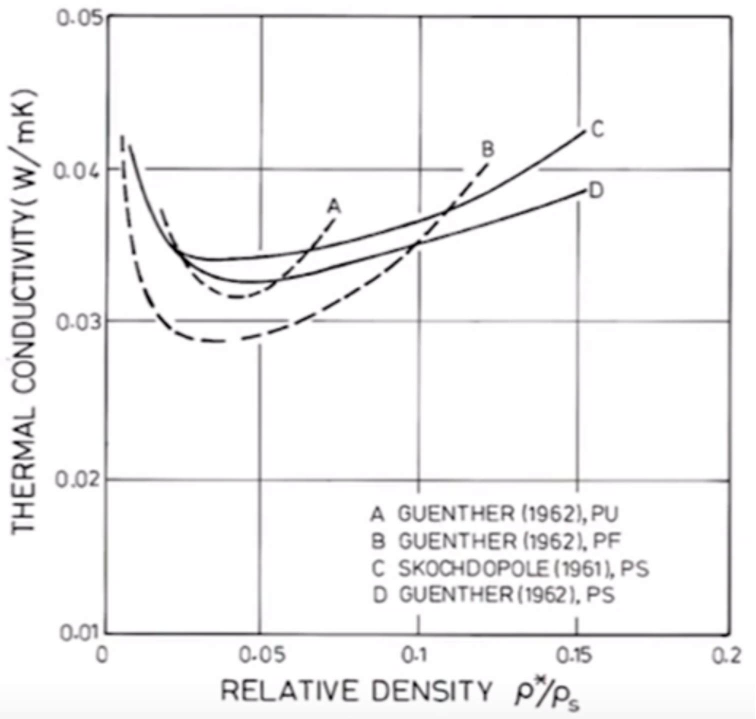

Figure 3.2: Thermal conductivity of a foam as a function of its relative density [5]

It is evident from these results that the conduction through the solid and the radiation through the foam exhibit stronger dependencies on the relative density when compared to conduction through the gas. This is attributable to the relatively low thermal conductivity of the gas phase. Additionally, what becomes worth observing is that the solid conduction and radiation are competing processes. As the relative density is increased, the solid structures within the foam occupy a greater volume. This provides a less tortuous path for conductive heat transfer to take place. However, the increase in solid structures within the foam is expected to scatter and absorb a greater amount of radiation [26, 27], thereby making it a less efficient mode of heat transfer and hence, reducing its contribution towards the overall thermal conductivity. Thus, as observable in Fig. 3.2, at a critical value of relative density, a shift is observed from radiation dominant heat transfer to conduction dominant heat transfer. Since at this point the contributions made by both these components are minimal, the overall thermal conductivity drops to its minimal value.

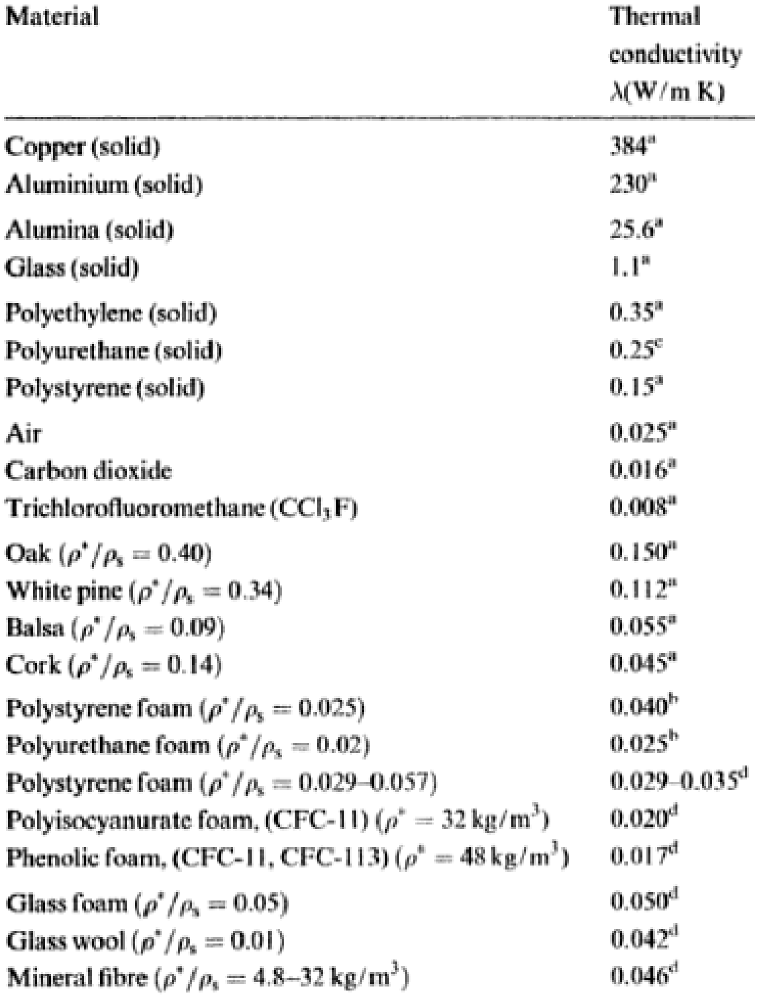

Material	Thermal conductivity λ(W/m K)
Copper (solid)	384[a]
Aluminium (solid)	230[a]
Alumina (solid)	25.6[a]
Glass (solid)	1.1[a]
Polyethylene (solid)	0.35[a]
Polyurethane (solid)	0.25[c]
Polystyrene (solid)	0.15[a]
Air	0.025[a]
Carbon dioxide	0.016[a]
Trichlorofluoromethane (CCl_3F)	0.008[a]
Oak ($\rho^*/\rho_s = 0.40$)	0.150[a]
White pine ($\rho^*/\rho_s = 0.34$)	0.112[a]
Balsa ($\rho^*/\rho_s = 0.09$)	0.055[a]
Cork ($\rho^*/\rho_s = 0.14$)	0.045[a]
Polystyrene foam ($\rho^*/\rho_s = 0.025$)	0.040[b]
Polyurethane foam ($\rho^*/\rho_s = 0.02$)	0.025[b]
Polystyrene foam ($\rho^*/\rho_s = 0.029$–0.057)	0.029–0.035[d]
Polyisocyanurate foam, (CFC-11) ($\rho^* = 32\ \text{kg/m}^3$)	0.020[d]
Phenolic foam, (CFC-11, CFC-113) ($\rho^* = 48\ \text{kg/m}^3$)	0.017[d]
Glass foam ($\rho^*/\rho_s = 0.05$)	0.050[d]
Glass wool ($\rho^*/\rho_s = 0.01$)	0.042[d]
Mineral fibre ($\rho^*/\rho_s = 4.8$–$32\ \text{kg/m}^3$)	0.046[d]

Figure 3.3: Thermal conductivity of common materials and foams [5]

Although these efforts look at providing the ideal starting point for estimating the thermal characteristics of foams at different relative densities, they, unfortunately, may not necessarily describe the ability of a foam to provide thermal insulation at different temperatures. Fig. 3.3 represents a table of thermal conductivity values that have been borrowed from Gibson and Ashby's [5] work. It is clear from this table that although most foams exhibit roughly the same thermal conductivity, their flame retarding capabilities are quite varied. In fact it is also possible for materials with a relatively higher thermal conductivity value to exhibit greater flame retarding capabilities (upon comparing cork to polyurethane). Thus, although there is a drop in the thermal conductivity of a material by introducing voids within it, thermal conductivity alone doesn't necessarily highlight properties such as flammability of the foam at higher temperatures (analogous to the flashpoint). This is typically a function of the phase changes/chemical degradation that the material undergoes under an oxidative/reductive environment at higher temperatures. It thus becomes important to specifically characterise the flame retarding capabilities of the biopolymer nanocomposite foams.

3.2 Methodology

The characterisation of the biopolymer nanocomposite foams was broken down into two sets of experiments. One where its flame retarding capabilities could be qualitatively tracked against that of cork and; another quantitatively highlighting how the differences in production techniques had an impact on the flame retarding capabilities. The quantitative results could then be suitably compared with known thermal protection systems.

3.2.1 Comparison with Cork

To carry out the experiments, cork that was available in synthesis laboratories as a stopper for experimental equipment was selected. A baked foam was selected as the representative sample for biopolymer nanocomposite foams. The baked foam was prepared by mixing 22.5% wt. of Bomalgin (Na-Alg) from Ranie Chemie, 22.5% wt. of Bentonite (Nanoclay) clay from Sigma-Aldrich, 5% wt. of food grade Ammonium Bicarbonate and 50% wt. deionised water. The sample was then placed on a silicone mat and baked at 140 °C for 1.5 hours using a hot air recirculation oven. It was subsequently dried using a well-ventilated fume hood.

As only a qualitative comparison between the biopolymer nanocomposite foam and the cork was sought, it was decided to simplify the experimental setup. Thus, the samples were tested in open-air conditions with the help of an oxidising propane-butane torch flame. The samples were held using a pair of metal tongs and the experiment was recorded with the help of a High Definition digital camera equipped with a CMOS sensor. The exposure to the flame was limited as much as possible to the front surface of both samples and lasted for two minutes. The samples were then allowed to cool in open-air conditions by distancing them from the flame and were stored for future analysis. The resulting recordings were paused at different timesteps to result in a stable emission from the samples' surface. The colour from these emissions was later compared with the colour temperature scale available on the IrfanView editing software to provide a qualitative estimation of the samples' surface temperature.

3.2.2 Influence of Production

To understand the influence that the individual production techniques had on the flame retarding capabilities of the foam, two representative foam samples were produced (one baked and one whipped). Whilst freeze-drying was also trialled as an independent production technique, the aim here was to highlight the differences between the samples with the lowest and highest densities.

Baked Foam

A bakeable dough mixture was created using 22.5% wt. of Bomalgin (Na-Alg) from Ranie Chemie, 22.5% wt. of CEBOGEL (Nanoclay) clay from Cebo International, 5% wt. of food-grade Ammonium Bicarbonate and 50% wt. deionised water. It was then baked in the oven at a temperature of 140 °C for 2 hours. The sample was covered in a layer of Aluminium foil during this process. The sample was then dried at a temperature of 40 °C, over a period of 72 hours using a vacuum oven. The thickness of the sample was then recorded using Vernier callipers with a least count of 0.05 mm.

Whipped Foam

The bulk of the whipped foam's production technique using Bomalgin and CEBOGEL was preserved from Chapter 2. The only differences include the saturation of the sample using CO_2 gas and skipping the use of $CaCO_3$. The intention here was to produce a sample with a greater density to limit voids whose dimensions were in the same order of magnitude as the thickness of the sample. Thus, the excess CO_2 gas was evacuated from the chamber and the contents were cast into the petri dish by pouring instead of spraying. This increase in density already stabilised the foam's initial structure and thus, didn't necessitate the use of $CaCO_3$. The thickness of the sample was then recorded using Vernier callipers with a least count of 0.05 mm.

Experimental Setup

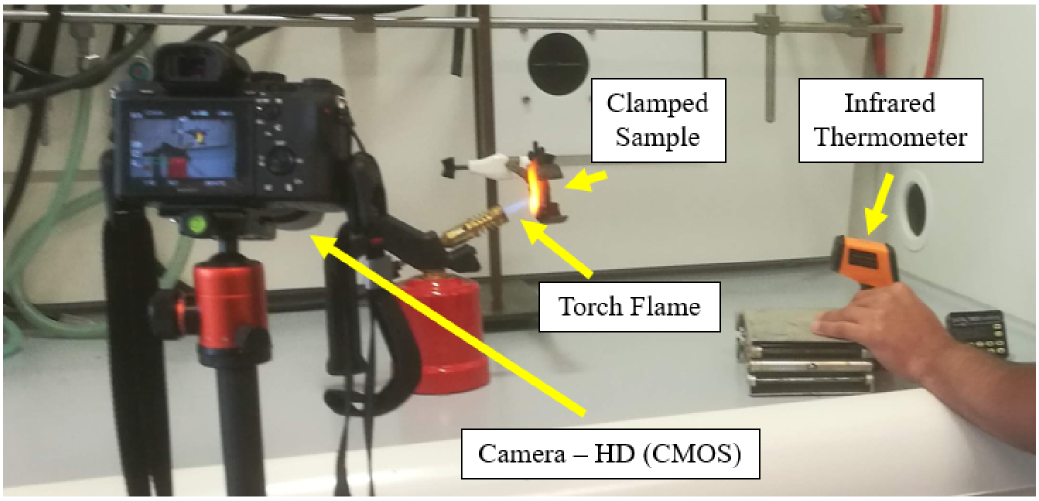

Figure 3.4: Setup to quantitatively study the influence of the production techniques on the flame retarding capabilities

Fig. 3.4 represents the setup that was in place to carry out the experiments. The samples were mounted vertically using a metallic clamp at a height suitable enough to direct the oxidising propane-butane torch flame. The length of the flame was kept consistent whilst studying both foams. This allowed for the underlying assumption that the heat source is adiabatic. As noticeable, the entire experiment was performed inside a fume hood where a stable airflow could be expected and the ambient conditions were well known (Temperature: 22 °C, Relative Humidity: 50%). The temperature of the surface opposite to that of the torch flame was measured using an infrared thermometer from a fixed distance. The thermometer was capable of measuring temperatures up to 380 °C. A High Definition, CMOS sensor-based camera was used to record the experiment. The front surface of the sample was exposed to the torch flame for a period of 2 mins. During this period, the temperature at the back surface of the samples was conveniently recorded at different intervals of time. Beyond the two minute stages, the recording was stopped and the camera was prepared to estimate the temperature of the front surface of the samples. This was done by adjusting the white balance colour temperature setting to 6500 K and clicking multiple photos of the samples and analysing them at different exposures levels; to account for the differences in the hue resulting from the inability of the sample's surface to act as an ideal black body. Once done, suitable sRGB values resulting from the stable surface emissions of the samples were extracted using the IrfanView editing software and converted to CIE 1931 xy values. These values were then virtually plotted onto the CIE xy chromaticity colour space to estimate the colour temperature resulting from the surface emissions on the samples. To better equip the reader on how these conversions/white balance settings result in meaningful colour temperature readings, it is important to provide knowledge about the CIE 1931 colour space. However, as this lies beyond the purview of this study, it has been explained in great detail in Appendix 7.2.

3.3 Results and Discussion

3.3.1 Qualitative Testing

The results for both, cork and the baked foam have been summarised pictorially using a sequence of images; obtained at different timestamps during the flame test (Figs. 3.5 and 3.6). It is clear that by the 24-second mark, the degradation within the cork sample is much more severe compared to that in the baked sample. This seems to progressively worsen as time proceeds and finally culminates in a charred mass that has shrunk down in volume and is pliable between the tongs. Whilst the surface of the baked sample undergoes progressive charring over the course of the entire flame test, no changes in its volume were observed and; the stiffness of the sample seemed to be barely impacted (despite the crack on the sample's surface). What's more, whilst the entire cork sample seems to have charred leading to the emission being produced by the entire sample, the emission in the case of the baked samples seems to be limited to only its front surface (Fig. 3.7). From the crude approximation of the colour temperature, it was clear that the temperature on the sample's surface was roughly between 1000 and 1500 K. When this temperature value is compared against literature sources that have documented the degradation of cork [30] and the biopolymer nanocomposite [2], the characteristic traits as observed above become clear.

In the case of cork, it has been noted that upon exposure to a temperature of 350 °C for an hour, the cork already loses roughly 62% of its original mass. The suberin, the polysaccharides from the cellulose and hemicellulose and a majority of the soluble lignin that characterises the cork material are expected to escape the sample, leaving behind only the insoluble lignin. Whilst the timescale from the results noted in literature are not the same as ones for the flame test being conducted here, it is expected that the elevation in temperature is sufficiently high to cause a partial volatilisation of the cork's polymers and a significant reduction of their functional groups. This explains the reduction in volume/structural integrity and the charring within the sample. As the escape of the volatile compounds is expected to occur in the open air, it creates room for ablation to occur from the entire sample and not just the front surface.

In the case of the baked foam however, the nanoclay is only expected to undergo fusion at a mean temperature of 1450 °C [31]. As the surface temperatures during measurements are well below this temperature, the fusion of clay is not expected to occur. However, the temperatures are sufficiently high enough to cause the degradation of the biopolymer thereby leading to charring within the sample. This explains why although charring was noticeable, the clay that is stacked within the sample provides both, the structural integrity, as well as the tortuous path that limits the diffusion of oxygen and other volatile gases that are trapped within the sample. Thus, ablation is not expected to occur.

In both cases, the degradation of the polymers in each sample has been identified as being the primary source of charring. This charring is expected to convert both the cork as well as the nanocomposite to a near-ideal black body, capable of radiating electromagnetic emissions outward, thus causing cooling within the sample.

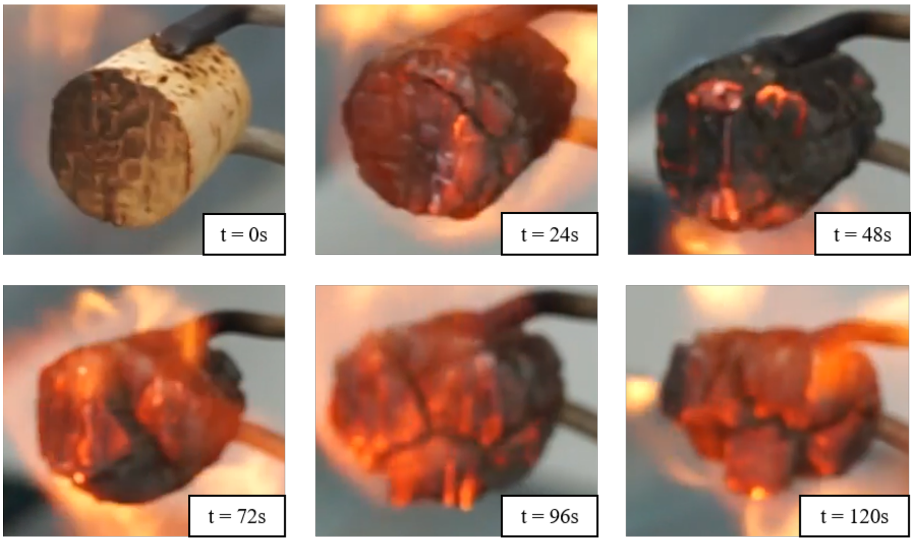

Figure 3.5: Cork at different time stamps of the qualitative flame test

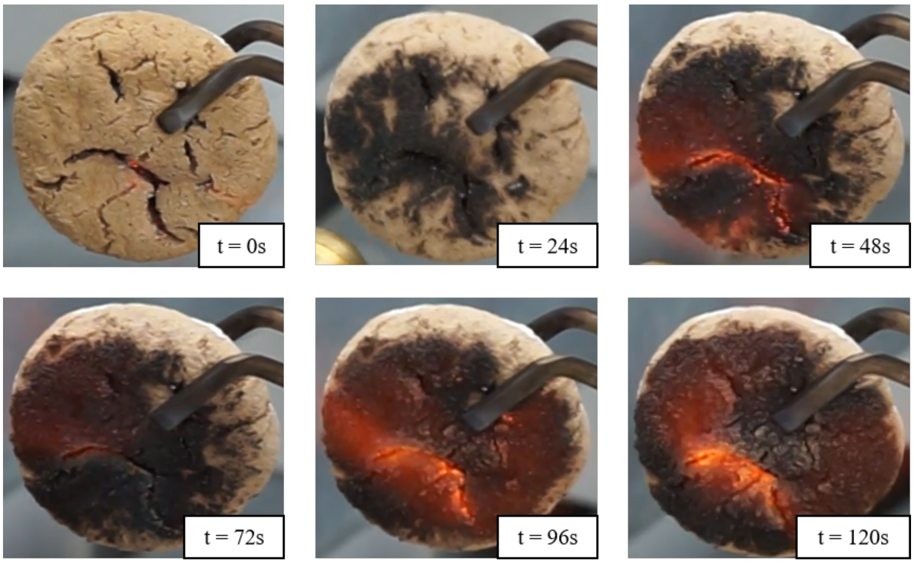

Figure 3.6: Baked nanocomposite foam at different time stamps of the qualitative flame test

Figure 3.7: Char layer of the baked sample

3.3.2 Quantitative Testing

The results for both, the baked and the whipped sample have been summarised pictorially using a sequence of images; obtained at different time stamps during the flame test (Figs. 3.8 and 3.9). Whilst these images provide a visual representation of the emissions, more can be inferred from looking at the samples before and after the test.

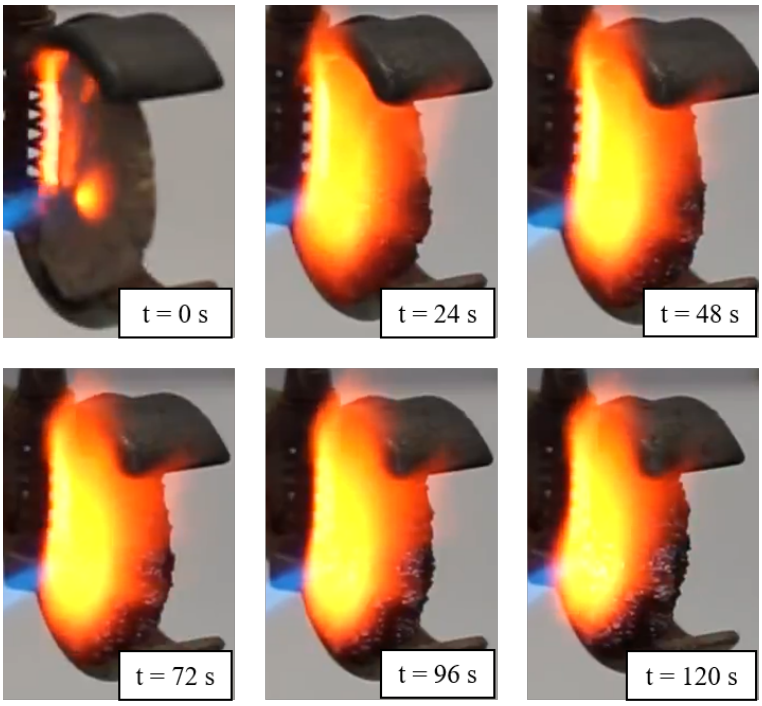

Figure 3.8: Baked nanocomposite foam at different time stamps of the quantitative flame test

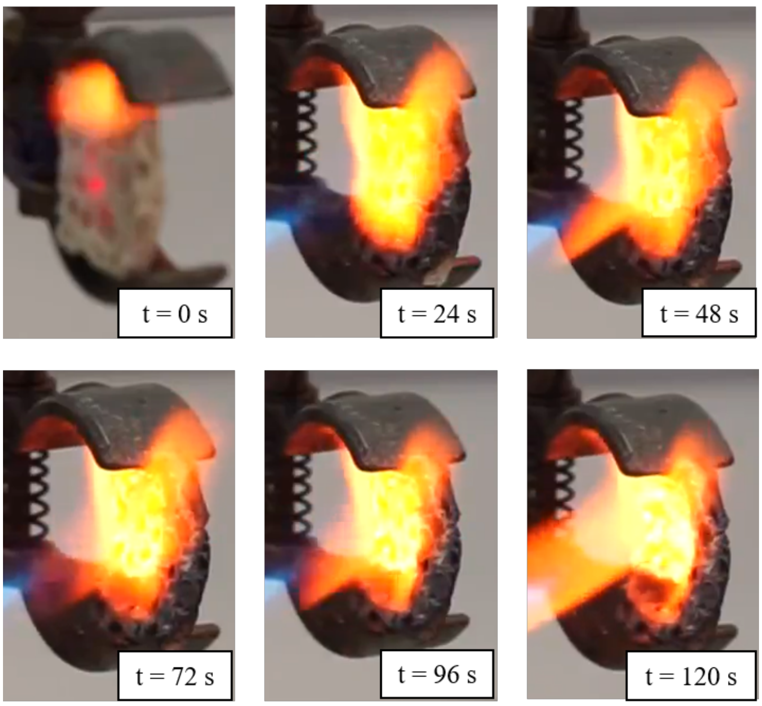

Figure 3.9: Whipped nanocomposite foam at different time stamps of the quantitative flame test

Figs. 3.10 and 3.11 represent the baked foam before and after (respectively) prolonged exposure to the flame, lasting appoximately three minutes. It becomes interesting to note that the sample has undergone a considerable expansion in its thickness. This is expected to have resulted from the entrapment of gases that are trying to diffuse away from the sample. What's more, compared to the qualitative test results from before, a greater thickness of the sample (if not the entire sample itself) has undergone charring. This is expected to be a consequence of a higher surface temperature and a smaller thickness of the sample.

Figure 3.10: Baked sample before test

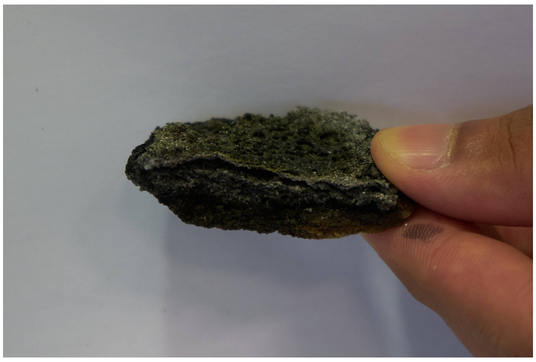

Figure 3.11: Baked sample after test

Figs. 3.12 and 3.13 represent the whipped foam before and after (respectively) prolonged exposure to the flame lasting appoximately four minutes. The hole after the flame test immediately suggests that the initial assumption of a higher flame temperature in the case of the baked sample is justified. In fact, for a hole to perepetuate through the thickness of the sample, the flame temperature must be higher than the range of temperatures where clay fusion is possible.

Figure 3.12: Whipped sample before test

Figure 3.13: Whipped sample after test

To understand just how high the temperature was, it became important to accurately predict the surface temperature using the CIE xy chromaticity colour space. However, as mentioned earlier, deviations stemming from the inability of the sample's surface to act as an ideal black body was expected and thus, the results from multiple exposure values were accounted for. Whilst it may seem sensible to quantify the exposure time in seconds, these values become meaningless unless a tangible phenomelogical explanation is provided. Fig. 3.14 represents the image used to express the lower exposure limit. Fig. 3.15 represents the image used to express the upper exposure limit. In both these cases, the images were considered over and underexposed based on the fact that the different zones within the flame were nearly indistinguishable. The colour temperature conversions yielded surface temperatures of 1753 K and 2303 K for the underexposed and overexposed images respectively. When an average of these two values is taken, it results in an average surface temperature of 2028 K.

Figure 3.14: Lower limit for exposure

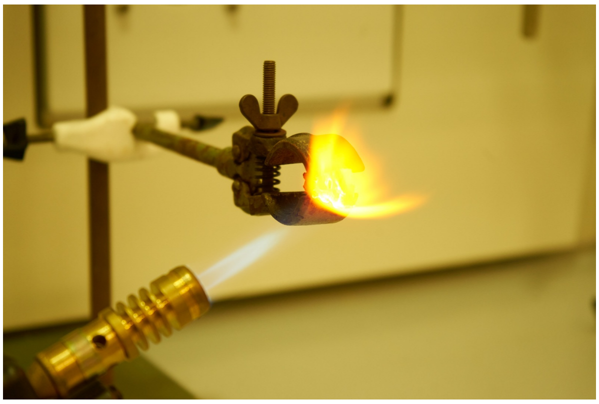

Figure 3.15: Upper limit for exposure

The average surface temperature, however, could also be arrived at theoretically. Based on the fact that complete degradation was noticeable within the sample (Fig. 3.13), the mean clay fusion temperature of 1450 °C was considered as the lower limit [31]. Similarly, as a propane-butane gas torch was used, the maximum possible adiabatic flame temperature of 1980 °C for propane based fuels [32] was considered as the upper limit. The average of these two values resulted in an average surface temperature of 1715 °C. This value, when converted using the Kelvin scale, yields a temperature value of approximately 1988 K.

When this theoretical value is used to construct a transient temperature gradient plot per unit thickness of the baked and whipped samples, it results in Fig. 3.16. The averaging errors being expressed here are based on the differences that exist between the theoretically estimated value and the values that result from the colour temperature readings. These errors represent less than 2.5% deviation from the theoretically estimated value. The temperature gradient drops by 8.21% from its original value in the case of the baked sample and by 13.47% from its original value in the case of the whipped sample over the entire measurement timespan. Since even a 2.5% deviation is eclipsed by these larger changes in the transient property's value, the errors can be accounted for as being minimal here. The human error that has been expressed in these figures has amounted to potential fluctuations in the handheld thermometer's temperature readings. As this error is eclipsed by the errors from averaging, it is considered to be negligibly small.

Although these results look at quantitatively providing the ability of a material to offer thermal insulation when exposed to a high-temperature flame, it should be noted, however, that the flame temperature plays a huge role here. This is because the nanocomposite is subject to a number of physical phase transformations as well as chemical decompositions. These changes are a function of temperature and thus influence the ability of the nanocomposite to act as a flame-retarding material. However, in the experiments conducted above, the average surface temperature is above the maximum clay fusion temperature and thus, it is expected that every potentially imaginable change in the sample has been undergone to provide the least possible thermal insulation possible. It can then be said that the values quoted in Figs. 3.16 are the conservative limits of the material's capabilities. In reality, the experiments can be repeated at the mean clay fusion temperature to offer a greater degree of accuracy. However, since it's exceedingly impossible to maintain even an adiabatic flame source exactly at this temperature, these values can already be used to describe the material's insulating characteristics at the mean clay fusion temperature.

Now that temperature gradient values were available, it becomes easy to compare the thermal characteristics of the material against the high-temperature tiles of NASA's Space Shuttle Orbiter [6,7]. Whilst a number of different thermal protection systems are enlisted for the Orbiter, it was deemed fit to draw a comparison against the tiles, as they are also sandwich structure-based systems. It is clear from Fig. 3.16 that the temperature gradient is at least four times higher for the nanocomposite foams. Whilst this may suggest that the nanocomposite foams outperform the high-temperature tiles, the maximum values stated for the tiles are the design values and do not necessarily correspond to the maximum possible temperature gradient of the tiles. However, since the tiles' temperature gradient value is deemed flight worthy for an Orbiter entering the Earth's atmosphere at velocities greater than Mach 10 [33], the nanocomposite foams at least offer viability for use aboard hypersonic sounding rockets.

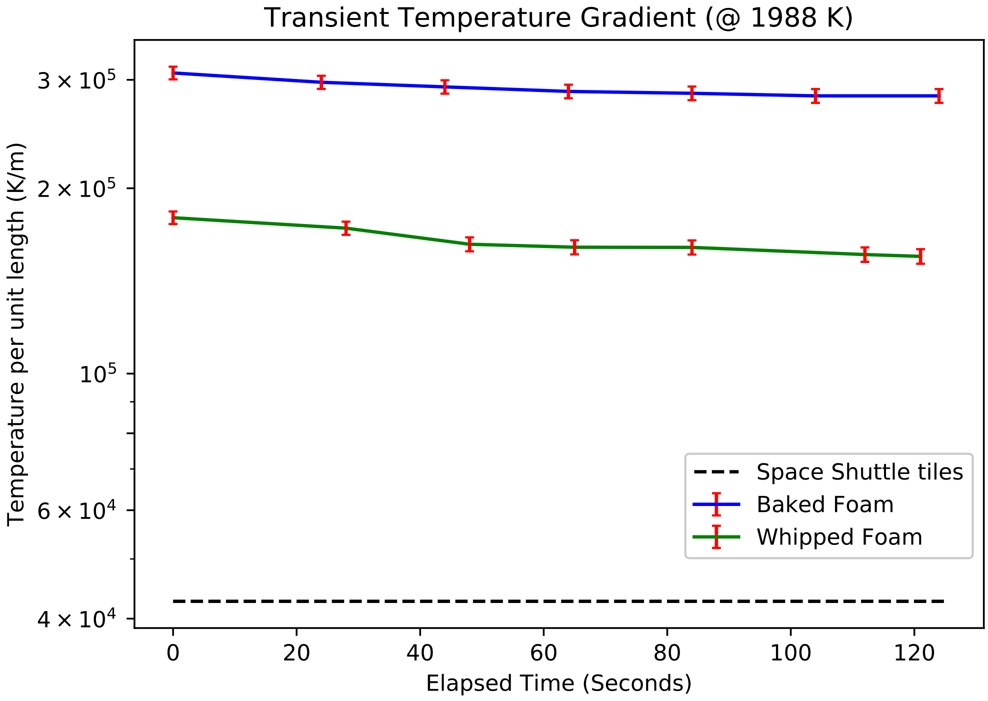

Figure 3.16: Comparing the transient temperature gradient of biopolymer nanocomposite foams and the maximum possible temperature gradient [6,7] for the Space Shuttle Orbiter's high temperature tiles.

Chapter 4

Theoretical Framework

Based on what has been discussed in Chapters 2 and 3, it may seem that sufficient data has been gathered to suggest that desirable characteristics have been sought from the nanocomposite foams. However, the mechanical characteristics also form an important part in the assessment of nanocomposite foams. This is because they provide an understanding of how the foams may be utilised/integrated structurally. The mechanics of foams however, has remained a widely elusive topic and, has beckoned the need for adopting multiple characterisation strategies [5,8–10,34–44].

The viability of utilising the theoretical framework provided by any one of these methods had prompted a detailed investigation of the various literature sources. The understanding gained from committing to this detailed literature review has been outlined in the subsequent sections; including the methods that were deemed fit to estimate the mechanical properties of nanocomposite foams.

4.1 Literature Review

The mechanical properties of foams stems directly from the properties of the solid material used to produce the foam. Thus, it first becomes important to understand the properties of the underlying nanocomposite itself. The work carried out by Zlopaša [2] aims at equipping the reader already with this knowledge and begins with the Halpin-Tsai equation [45]:

$$E_c = E_m \frac{E_f(1+\zeta\phi_f) + E_m(\zeta - \zeta\phi_f)}{E_f(1-\phi_f) + E_m(\zeta + \phi_f)} \tag{4.1}$$

Where E_c, E_m and E_f are the modulus values of the composite, matrix and the filler phases respectively, ϕ_f is the volume fraction of the filler phase and ζ is the shape factor of the filler whose value is dependent on the geometry, orientation and aspect ratio of the filler. Equation 4.1 can be further simplified upon comparing E_c/E_m to ζ.

In cases where $\zeta << Ec/Em$:

$$E_c = (\frac{1-\phi_f}{E_m} + \frac{\phi_f}{E_f})^{-1} \tag{4.2}$$

In cases where $\zeta >> Ec/Em$:

$$E_c = (1-\phi_f)E_m + \phi_f E_f \tag{4.3}$$

Equations 4.2 and 4.3 describe the series and the parallel models for composites respectively. As described by Zlopaša, the series model usually underestimates the modulus and the parallel model usually overestimates the modulus. Hence, in most cases, the observed modulus lies between these two limits. To estimate the modulus values of Na-Alg and nanoclay based nanocomposite films, Zlopaša borrowed the shape factors as prescribed by van Es [14] to formulate the following equation:

$$E_c = (\frac{<P_2>}{E_{\parallel}} + \frac{1-<P_2>}{E_{\perp}})^{-1} \tag{4.4}$$

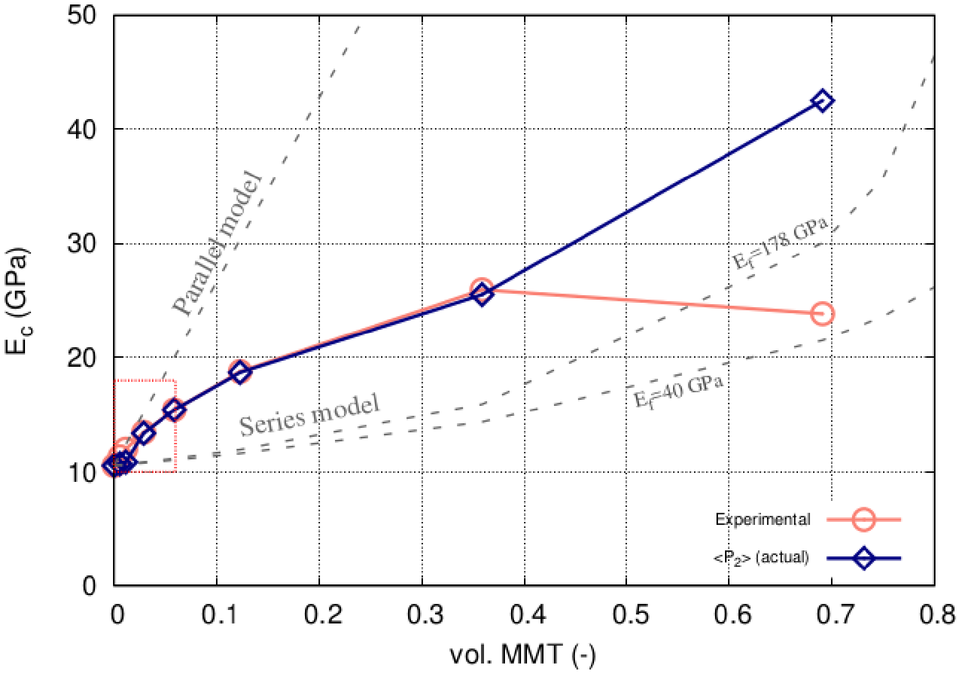

Figure 4.1: Storage modulus v/s vol. frac. of MMT clay in sodium alginate-MMT nanocomposites [2]

Where the tensile modulus in the radial direction of the clay platelets ($E_{\parallel}$) is calculated using Equation 4.1 by assuming $\zeta = 2/3 * (L/D)$ and; the tensile modulus in the perpendicular direction of the clay platelets ($E_\perp$) is calculated by assuming $\zeta = 2$. $< P_2 >$ here describes the average degree of ordering of the clay platelets in the cross-sectional plane of the nanocomposite film. When all the clay platelets are aligned perfectly parallel to each other, $< P_2 > = 1$ and when the alignment of the clay platelets is completely random, $< P_2 > = 0$. To illustrate the accuracy of this model, Zlopaša plotted the observable modulus values for different concentrations of nanoclay against his theoretical estimations (Fig. 4.1). The deviations of the observable modulus from the predictions at higher concentrations has been attributed to the limited exfoliation achievable between the clay platelets; thereby dropping the effective aspect ratio. This additionally serves to highlight why the 50% wt. ($\sim$ 0.36 vol. frac.) concentration of nanoclay in Na-Alg becomes the desirable loading concentration: as it leads to the best tradeoff between the mechanical and thermal properties of the nanocomposite.

It now becomes important to evaluate the elastic modulus of the foams. To facilitate this more conveniently for the reader, the sources available in literature have been broadly classified into two subgroups; those that describe the analytical methods and those that describe the numerical methods. As the latter is very much dependent on the groundwork posed by the analytical techniques, the reader is first acquainted with the former.

4.1.1 Analytical Methods

When it comes to the subject of estimating the elastic modulus of foams, Gibson and Ashby [5] look at providing a holistic consolidation of previous endeavours and thus; their methods are widely accepted amongst other literature sources [8–10,38–44]. Hence, their approach towards estimating the modulus has broken down in great detail.

Intuitively, it can be understood that if any solid material is turned into a foam, a large number of voids are introduced within the structure, thereby reducing its stiffness. However, the quantification of this stiffness is subject to the accurate prediction of the micro-scale deformations that occur within the cells of the foam structure. Whilst numerous attempts have been made in the past to model these deformations [34–37], Gibson and Ashby look at consolidating these efforts into a single formula for linear-elastic loading:

$$\frac{E^*}{E_s} = C_1\phi^2(\frac{\rho^*}{\rho_s})^2 + C_2(1-\phi)\frac{\rho^*}{\rho_s} \tag{4.5}$$

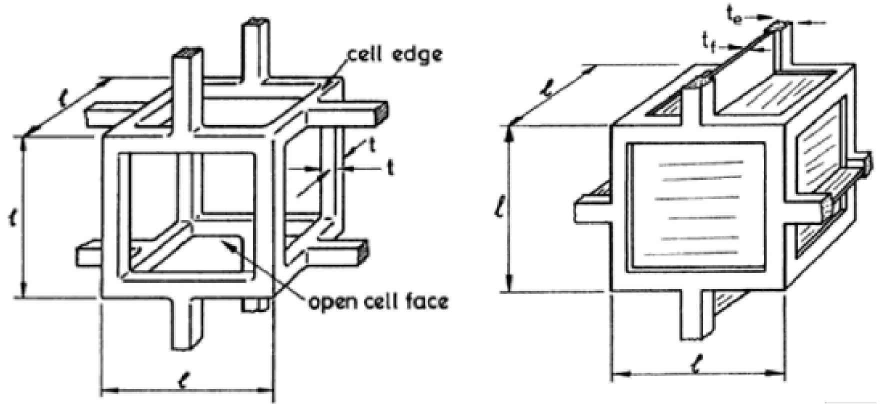

Figure 4.2: Open cell (left) and closed cell (right) foams [5]

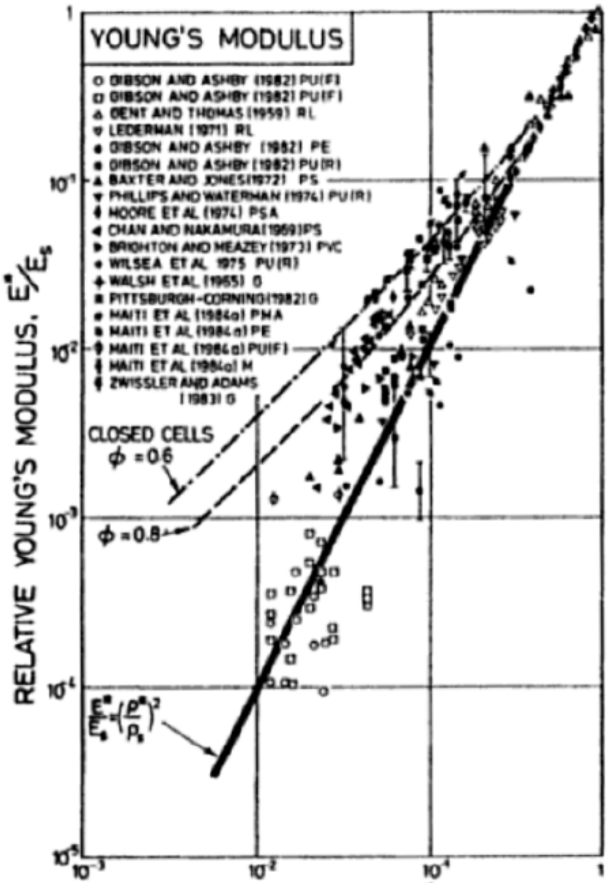

Figure 4.3: Relative Young's modulus as a function of relative density [5]

Where E^* represents the Young's modulus of the foam and E_s represents Young's modulus of the original solid material. The cells of a foam material may either, only be characterised by strut shaped members along its edges (open cells) or by both, strut shaped members as well as membrane shaped walls (closed cells) (Fig. 4.2). Thus, ϕ represents the volume fraction of solid that is contained in the cell edges. (1 - ϕ) then represents the volume fraction of solid that is contained in the membranes of the cell walls for closed-cell foams. C_1 and C_2 represent the constants of proportionality. The first term on the right-hand side of Equation 4.5 represents the contribution made by the cell edges and the second term on the right-hand side of the same equation represents the contribution made by the membranes of the cell walls. In order to help understand how the constants C_1 and C_2 may be evaluated, the results obtained from multiple experiments for both open as well as closed-cell foams were consolidated into a single plot (Fig. 4.3). The best-fitting curves were obtained when both C_1 and C_2 approached unity. Thus, based on these results, Equation 4.5 was modified to help approximately predict Young's modulus of any foam material:

$$\frac{E^*}{E_s} \approx \phi^2(\frac{\rho^*}{\rho_s})^2 + (1-\phi)\frac{\rho^*}{\rho_s} \tag{4.6}$$

4.1.2 Numerical Methods

The analytical framework that has been discussed so far looks at estimating the properties of conventional foam materials that are easily producible using polymers. However unconventional foam materials that can be produced using metals, ceramics or composites even, have prompted the use of Finite Element (FE) methods to estimate their properties [8,9,41,43]. In one instance, these techniques have also been extended to estimate the properties of closed-cell polymer foams [42]. As described by Betts [41], the utilisation of FE methods to estimate the mechanical properties is heavily reliant on the foam geometries that are successful in capturing the morphology of the foam cells. To that effect, he discusses two of the most prevalent techniques to generate cell geometries:

Tetrakaidecahedron Cells

In order to simplify the task of modelling the morphology of foam cells, the use of tetrakaidecahedron cells (also called Kelvin cells) to generate a representative volume element, capable of representing the idealised morphology of the foam, has been adopted as one of the strategies [8,9,41] (Fig. 4.4). The use of Kelvin cells has been attributed to their ability to fill space when stacked in a body-centred configuration [39]. In all cases, these Kelvin cells are modelled as 3D solid structures in order to generate voxels of desired dimensions. Additionally, Wang et. al. also depict how this modelling technique can be extended to introduce a random distribution of fillers within the struts (cell edges) and the walls of the cell [8] (Fig. 4.5).

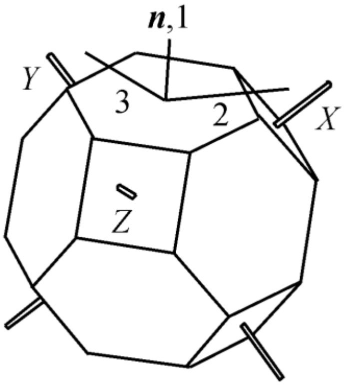

Figure 4.4: Tetrakaidecahedron cell [8]

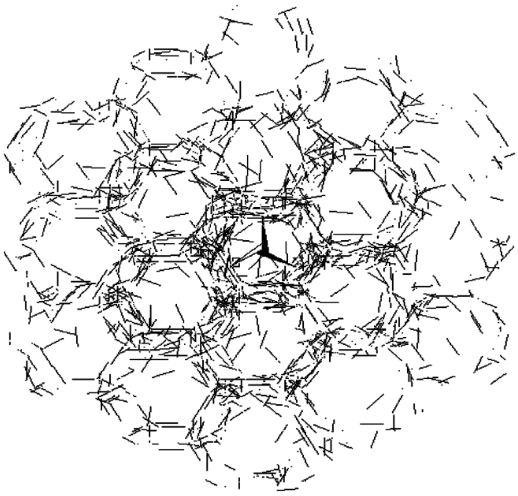

Figure 4.5: Random distribution of fillers within Kelvin cells [8]

Voronoi Technique

As described in literature [8,9,42,43], the Voronoi technique looks at capturing the morphology of the foam cells more realistically. This technique relies on the creation of a random spatial distribution of a fixed number of nucleation sites within the voxel. Subsequently, the empty space surrounding these sights are broken down into polygonal regions, whose edges act as the perpendicular bisectors of the line segments connecting adjacent nucleation sites. This breakdown ultimately leads to the creation of a tessellation within the three-dimensional space of the voxel. The tessellation is then utilised to create the solid cell struts and cell walls to yield the foam-like morphology. In order to mitigate the risk of cells collapsing within one another, a parameter called δ that regulates the distance between adjacent nucleation sites is usually prescribed. Additionally, the degree of periodicity/randomness in the ordering of the cells is usually measured using a parameter called α. Whilst a single definition of α doesn't exist, it is usually expressed as a non-dimensional number that scales linearly with respect to the ratio δ/L, where L usually represents the distance between adjacent nucleation sites in the case of a periodic arrangement of cells. When δ changes, α changes and the degree of randomness/periodicity amongst the cells also changes. It should be noted here that it is also possible to revert back to the ordered Kelvin cell-like arrangement by setting α to zero. This has been illustrated in Fig. 4.6.

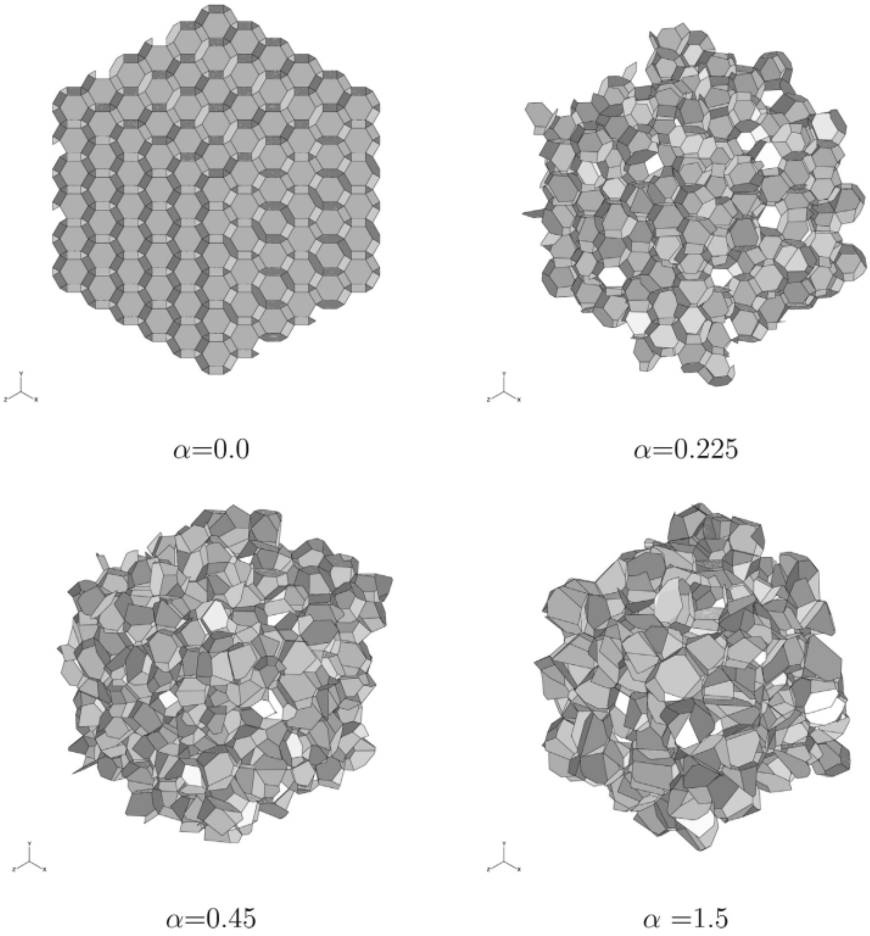
α=0.0

α=0.225

α=0.45

α =1.5

Figure 4.6: Voronoi tessellations with varying degrees of periodicity [9]

4.2 Critique on Literature Sources

Much like the section before this, it too has been split between the analytical and numerical methods.

4.2.1 Analytical Methods

On the subject of predicting the elastic modulus of foams, Gibson and Ashby try to provide a set of best-fit curves for all foams. However, by doing so, some critical details are overlooked. The scatter in Fig. 4.3 has been predominantly attributed to the uncertainty associated with the limited precision by which a polymer's original modulus value can be measured. This has been explained as being dependent on the alignment of the polymer chains. However, this needn't be the case necessarily. In order to fit the curves, the constants of proportionality (C_1 and C_2) in Equation 4.5 have been approximated to 1. In reality, these constants are the prefactor terms that accompany the relative density term. They must therefore be dependent on the shape of the foam cells. To make the underlying assumption that these terms approach unity suggests that the elastic modulus of any foam is independent of the shape of its cells. At first glance, this seems counterintuitive and thus, requires a much more detailed assessment; ideally with an alternative approach that is independent of the micro-scale deformations that occur within the foams.

4.2.2 Numerical Methods

Unlike the analytical models, the numerical models are not coerced by limitations in predicting the micro-scale deformations. Also, since the interest lies predominantly in predicting the relative modulus of foams, the FE analysis can be carried out using simple linear elastic models. Whilst the numerical models seem to tackle the major limitations associated with the analytical models, they do however suffer from their own disadvantages. One of the glaring loopholes that exist amongst all literature sources is the inadequacies associated with accurately mentioning the boundary conditions and the type of loads that are applied. Whilst this may indicate that it is indeed open to the reader's interpretation, it also highlights the lack of a standardised simulation technique. Thus, the onus falls on the individual to ascertain the validity of the numerical simulations. Secondly, although the Voronoi technique is provided as a solution to model the foam geometries accurately, it is not the easiest method to adopt. Barbier et. al. [9,42] describe the use of a software library based tessellation generator (Voro++). Whilst packages such as Voro++ [44] offer an open-source solution, it still suppresses some of the geometric features of the foam. A similar problem persists if one were to incorporate the random distribution of fillers within the Kelvin cells. Whilst alternate strategies that make use of tomographic images have also been mentioned in literature [40], it still reiterates the fact that the realistic modelling of the foam geometry is not straightforward.

4.3 Alternate Methodology

So far, an overview of some of the widely prevalent methods has been provided and some of their concerning drawbacks have been highlighted. The task of better understanding the theory in place to characterise the elastic modulus of foams, however, still remains. To that effect, the initial phase of this study was spent in unravelling some of the concerns highlighted earlier; specifically, the shape independence of foams implicitly stated by Gibson and Ashby in their approach and simplifying the task of characterising foams numerically.

4.3.1 Halpin Tsai approach and Shape Independence

The Halpin-Tsai modelling technique although semi-empirical in nature can be facilitated by strong theoretical reasoning; whilst simultaneously supporting a simple modelling technique. Thus, an investigation was carried out to assess whether this technique could be extended to model the relative modulus of foam materials. By doing so, it is assumed that a foam is a composite material, whose solid matrix is filled with fluid voids.

It was already discussed earlier, how Zlopaša modified Equation 4.1 to predict the modulus of the nanocomposites. It is now possible, however, to modify the same equation to predict the elastic modulus of foams. Upon considering a foam as a composite material whose matrix phase is the solid material and whose fillers are the fluid voids trapped within the foam, the original Halpin-Tsai equation (Equation 4.1) becomes:

$$E_{foam} = E_{solid}\frac{E_{fluid}(1+\zeta\phi_{fluid}) + E_{solid}(\zeta - \zeta\phi_{fluid})}{E_{fluid}(1-\phi_{fluid}) + E_{solid}(\zeta + \phi_{fluid})} \tag{4.7}$$

Given that $E_{fluid} << E_{solid}$, the fluid contribution to the modulus can be negated from Equation 4.7 to yield the following relation:

$$E_{rel} = \frac{E_{foam}}{E_{solid}} = \frac{1-\phi_{fluid}}{1+(\phi_{fluid}/\zeta)} \tag{4.8}$$

Where E_{rel} represents the relative modulus of foams. However, the relative modulus of foams is not expressed in terms of volume fractions. Rather, it is given in terms of the relative density:

$$\rho_{rel} = \rho^*/\rho_s = \frac{m_{foam}/V_{foam}}{m_{solid}/V_{solid}} \tag{4.9}$$

Where ρ^* represents the density of the foam, ρ_s represents the density of the original solid from which the foam is made, m_{foam} represents the mass of the foam, V_{foam} represents the volume occupied by the foam, m_{solid} represents the mass of the original solid and V_{solid} represents the volume occupied by the original solid. It is known that $m_{foam} = m_{solid} + m_{fluid}$. However, $m_{fluid} << m_{solid}$ and so, the fluid contribution can be negated. Therefore:

$$\rho_{rel} \approx \frac{V_{solid}}{V_{foam}} \tag{4.10}$$

The volume fraction of the solid within the foam can be estimated using the following relation:

$$\phi_{solid} = (1 - \phi_{fluid}) = \frac{V_{solid}}{V_{solid} + V_{fluid}} = \frac{V_{solid}}{V_{foam}} \tag{4.11}$$

Thus, upon comparing Equations 4.10 and 4.11, the following relation is obtained:

$$\rho_{rel} \approx (1 - \phi_{fluid}) \tag{4.12}$$

Substituting the value of relative density from Equation 4.12 into Equation 4.8, the following equation is obtained for the relative modulus of foams:

$$E_{rel} = \frac{E_{foam}}{E_{solid}} \approx \frac{\rho_{rel}}{1 + [(1 - \rho_{rel})/\zeta]} \tag{4.13}$$

Since Equation 4.13 offers a non-dimensional relation, it must stand for all foam materials. However, in order to characterise the relative modulus for both, open as well as closed-cell foams, the task of accurately estimating the value of the shape factor still remains. More so, once the shape factor has been estimated, its value must be quantitatively as well as qualitatively understood in order to gain a strong, theoretical perspective.

As mentioned earlier, the shape factor is dependent on the geometry, aspect ratio and orientation of the filler. In the case of foams, the shape factor would then stem from the shape of the structures that make up the cells themselves. In the case of open cell foams, this would translate to the strut like structures that make up the foam. Thus, the estimation begins by considering a rod-shaped element of thickness d and length l (Fig. 4.7). In order to simplify the procedure of capturing the morphology of an open-cell foam, this rod can be translated and rotated in a three-dimensional space to obtain the desired representative cell element. Then, the volume of the entire element is proportional to l^3 and the volume of the rods that are present within the element is proportional to d^2l. Thus, the relative density of the cell element (vis-à-vis the foam) is given by the following relation:

$$\rho_{rel} \propto (d^2l/l^3) = (d/l)^2 \tag{4.14}$$

In the case of isotropic foams, the rod is rotated and translated randomly in three-dimensional space. Thus, statistically speaking, the constant of proportionality in Equation 4.14 becomes unity (as stated). Similar to the approach adopted for open-cell foams, the relative density approximation for closed-cell foams begins with the consideration of an arbitrary membrane shaped element of edge length a and thickness t (Fig. 4.8). This membrane looks at representing the walls that make up the closed cell morphology. It can be suitably rotated or translated in three-dimensional space to obtain the desired representative cell element. Then the volume of the entire element is proportional to a^3 and the volume of the walls that are present within the element is proportional to a^2t. Thus, the relative density of the cell element (and of an *isotropic/statistically averaged* foam) is given by the following relation:

$$\rho_{rel} \propto (a^2t/a^3) = (t/a) \tag{4.15}$$

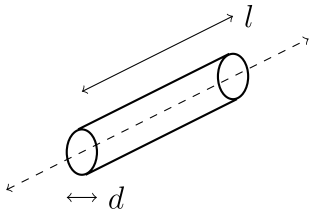

Figure 4.7: Rod Shaped Element

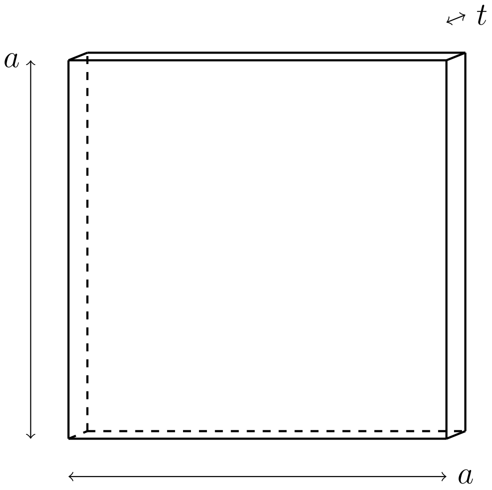

Figure 4.8: Membrane Shaped Element

It is thus clear from Equations 4.14 and 4.15 that the relative density in itself looks at describing the effect of shape in the case of foams. If the shape factor term in Equation 4.13 is substituted as the relative density, then the following realtion is obtained:

$$E_{rel} = \rho_{rel}^2 \tag{4.16}$$

Upon comparing Equations 4.14 and 4.15, it is clear that the relative density exhibits a square dependency on the geometric ratio in the case of open-cell foams; and a linear dependency on the geometric ratio in the case of closed-cell foams. If thus, the relative density of closed celled foams is squared and substituted back into Equation 4.13 as the shape factor term, the following relation is obtained:

$$E_{rel} = \frac{\rho_{rel}^3}{\rho_{rel}^2 - \rho_{rel} + 1} = O(\rho_{rel}) \tag{4.17}$$

The results of Equations 4.16 and 4.17 are not dissimilar to the contributions obtained by Gibson and Ashby for open cell and closed cell foams respectively (Equation 4.6). It thus indicates that the relative modulus does in reality exhibit some sort of shape independent power-law dependence on the relative density. In the Halpin-Tsai approach, however, the result for closed-cell foams is arrived at by making the underlying assumption that closed-cell foams are only characterised by membranes. In reality, closed-cell foams are also characterised by strut like members. Thus, the relative modulus according to the Halpin-Tsai approach can be expressed by the following relation:

$$E_{rel} = \rho_{rel}^{\alpha} \tag{4.18}$$

Where α is the power index term, such that $1 \leq \alpha \leq 2$; depending on the vol. fraction of the strut like members. If the foam is characterised only by struts, then $\alpha = 2$. However, if there are no struts at all within the foam, then $\alpha = 1$. The results for different values of α, obtained from equation 4.18 were overlapped with the best-fit curves that were obtained by Gibson and Ashby in Fig. 4.3. This has been depicted in Fig. 4.9.

It is clear, that an alternate approach, such as the Halpin-Tsai approach, that doesn't rely on consolidation, but rather on alternate theoretical reasoning also looks at providing shape independence for foams. However, the following underlying assumptions need to be made:

1. To ensure that there are no coefficient terms that result from the estimation of the relative density, it is assumed that the cells of the foam yield from statistically averaging the random translations and rotations of the strut/membrane in three-dimensional space. This would then result in an isotropic foam structure whose properties are independent of the shape of the cells.
2. It is assumed by Gibson and Ashby that the struts of an open-cell foam structure act as beams and the cell walls of closed-cell foam structures act as membranes. However, the morphology of a foam needn't remain consistent for all foams in general. In fact, this is predominantly influenced by the production technique. The fact

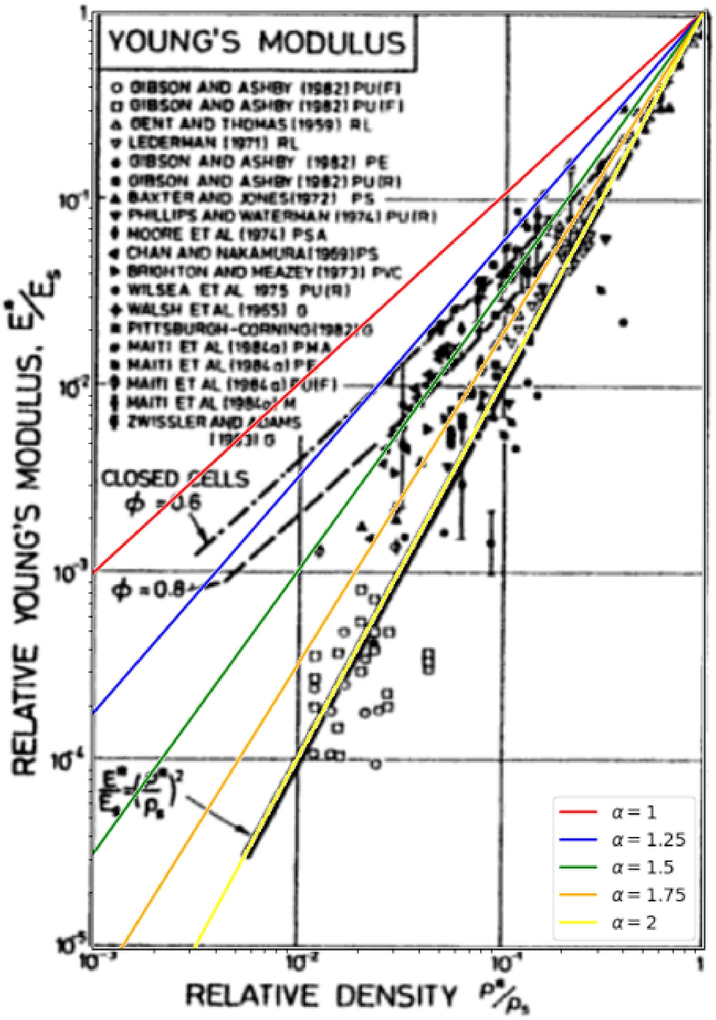

Figure 4.9: Visual comparison between the Gibson-Ashby model and the Halpin-Tsai approach

that most commercially available polymer foams exhibit a standard morphology is a consequence of the standardised extrusion technique using a blowing agent. However, if alternate production techniques are sought, then it isn't guaranteed that they obey the beam and membrane simplification that is expected from open and closed cell foams respectively.

4.3.2 Standardising Numerical Simulations

The primary question that needs answering on the numerical simulations front is the type of modelling technique that is worth adopting to depict foams. Whether the use of random, tesselation algorithms really has an edge over techniques that rely on idealising the cell geometry to create lattice-like voxels. Zhu et. al. [10] carried out a study for regularly arranged and random open-cell foam geometries (Fig. 4.10). They opted to represent the degree of randomness using a dimensionless parameter called C_v whose value is given by the ratio of the standard deviation of the cell diameter to the average value of the cell diameter. The terms C^*_{11}, C^*_{12} and C^*_{44} in Fig. 4.11 represents the terms that make up the effective stiffness matrix. Based on the results obtained from their study, it seems that the differences in the stiffness parameters are the greatest between the Kelvin cell model and the other random models. Thus, it becomes important to understand if the use of other idealised cell geometry models is justified in predicting the stiffness of the foams. Upon revisiting the approach adopted by Gibson and Ashby for estimating the contributions made by open and closed cell geometries, it becomes clear that modes of deformation were also hypothesized by idealising the morphology of foams as staggered cubic lattices (Fig. 4.2). This model was considered suitable for comparison against the Kelvin cell strategies.

Unlike conventional FE software packages, it was understood that FEniCS made use of a more transparent approach. FE methods in general concern themselves with converting the strong form partial differential equations to a weak form solution that offers themselves up for discretisation using linear algebra. However, conventional software suites mask this process from the user and thus, the user is only exposed to an abstract understanding of how this takes place. The advantage of using FEniCS is that the user can instead use the Python-based front end to feed in the weak form partial differential equation themselves. This allows them to understand the system of equations as well as the variables for which the solution is being obtained. As the main concern of this study involves linear elasticity, the following system of equations was considered [46]:

$$\begin{aligned} a(u,v) &= \int_\Omega \sigma(u) : \nabla v dx \\ \sigma(u) &= \lambda(\nabla \cdot u)I + \mu(\nabla u + (\nabla u)^\top) \\ L(v) &= \int_\Omega f \cdot v dx + \int_{\partial\Omega_T} T \cdot v ds \end{aligned} \tag{4.19}$$

Where, u is the unknown displacement term defined in the spatial domain Ω, v is the test function, σ is the stress, λ and μ are Lame's coefficients, f is the body force also acting in the spatial domain Ω and T is the traction (stress at the boundary) on the boundary of this spatial domain. The unknown equation is solved for by equating the functions a and L, which are nothing but a set of linear functions that offers the viability for discretisation.

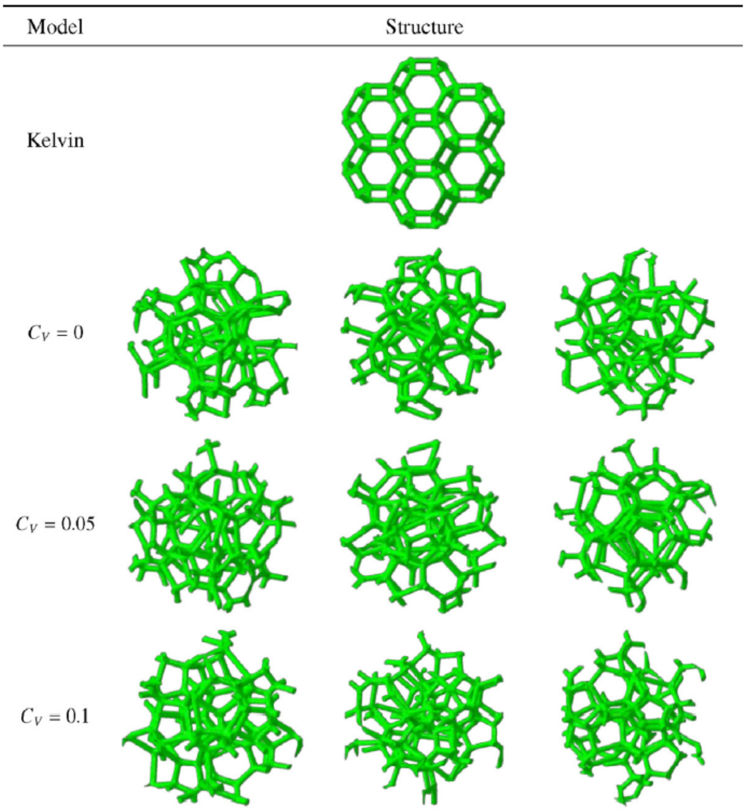

Figure 4.10: Differences between Kelvin cell and random models for open cell foams [10]

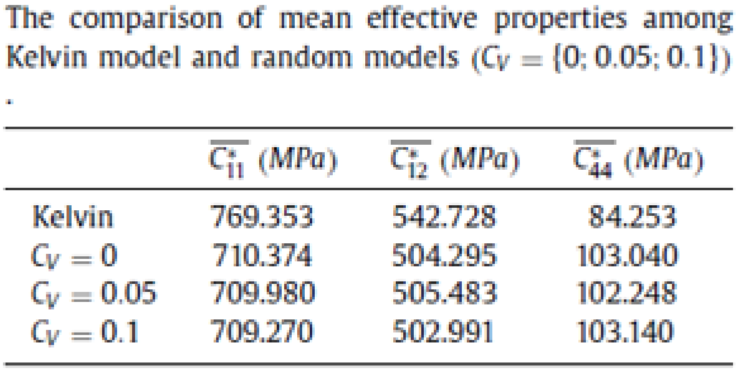

The comparison of mean effective properties among Kelvin model and random models ($C_V = \{0; 0.05; 0.1\}$)
.

	$\overline{C_{11}^*}$ (MPa)	$\overline{C_{12}^*}$ (MPa)	$\overline{C_{44}^*}$ (MPa)
Kelvin	769.353	542.728	84.253
$C_V = 0$	710.374	504.295	103.040
$C_V = 0.05$	709.980	505.483	102.248
$C_V = 0.1$	709.270	502.991	103.140

Figure 4.11: Stiffness terms for regular and random open cell foams [10]

Since a system for solving the equations was identified, the next step was to model the foam geometries themselves. Gmsh was identified as another viable software package to model the foam geometries. It was possible to use Gmsh to model both, the staggered cubic shaped cells, as well as the Kelvin cells. Subsequently, these geometries could also be meshed using tetrahedrally shaped cells (Figs. 4.12 and 4.13). Unfortunately however, FEniCS is only equipped to read the .xml file extension format for meshed files. This meant having to convert the Gmsh files from their native .msh format to the .xml format using the meshio package available on the Python Package Index. Despite this, the meshed files were still deemed unreadable by FEniCS. The reasons for this were attributed to either, the complexities involving the geometries and their meshes or, the lack of relevant mesh conversion documentation that is available for the latest releases of FEniCS. It thus resulted in having to use FEniCS's inbuilt geometry and mesh generating tools. As these tools are not equipped to handle complicated geometries, it was only possible to create the open cell staggered geometry (Fig. 4.14). Even so, these tools don't offer ease of scalability or the versatility required to test multiple idealised foam morphologies. It thus poses the greatest limitations in terms of carrying out a methodological study. In theory, it would be possible to carry out a more elaborative study to understand how a versatile open-source software like FEniCS can be used to model the idealised foam morphologies. However, since this would be rather extensive and lays more emphasis on developing the tools in place for analysis over actually understanding the underlying the mechanics of the foams themselves, it lies outside the purview of this study.

For the reader, however, this is indeed an open-ended challenge that is worth pursuing in the future. To that effect, the code that was utilised to generate the foam morphology on FEniCS can be found in Appendix C.

4.4 Research Question

On the front of characterising the foams mechanically, it has been shown that estimations of the relative modulus can be made by providing strong analytical reasoning in more than one way (Gibson and Ashby approach/ Halpin-Tsai approach). Although efforts can be made to estimate the modulus of foams numerically, it would rely on the extensive development of idealised foam morphologies. Thus, it was decided to compare the experimental results of the foam moduli with the estimations that can be made using the analytical techniques mentioned above. To that effect, the following research question was formulated:

Can the relative modulus of biopolymer nanocomposite foams be experimentally characterised; in an effort to understand the validity of the analytical techniques that were identified as being suitable? If not, can the shortcomings be addressed suitably?

The details pertaining to how these experiments were carried out to specifically answer this question has been discussed in subsequent chapters.

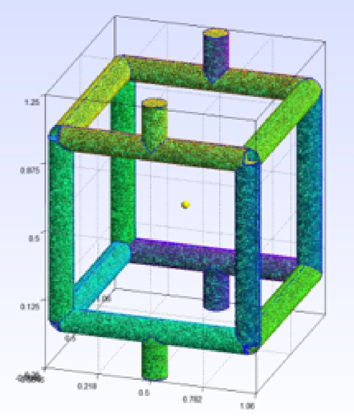

Figure 4.12: Meshed cubic cell

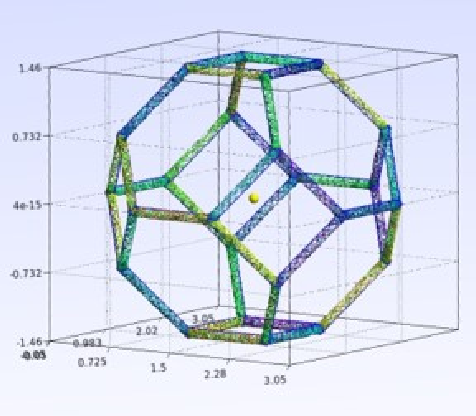

Figure 4.13: Meshed Kelvin cell

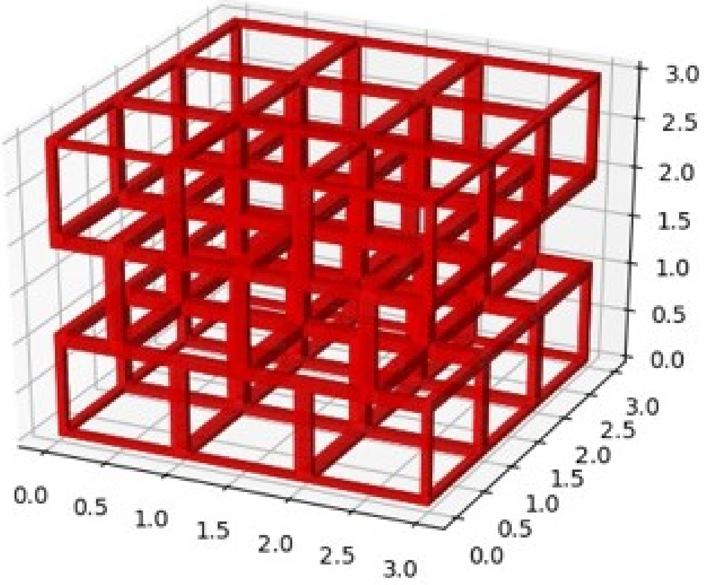

Figure 4.14: Staggered cubic lattice generated using FEniCS

Chapter 5

Sources of Error

In this Chapter, the steps that were taken to mitigate errors that may otherwise exist whilst estimating the relative density v/s relative modulus of biopolymer nanocomposite foams have been highlighted in great detail.

As stated earlier in Chapter 4, the scatter in the relative modulus v/s relative density plot (Fig. 4.3) is associated to the limited precision by which the polymer's original modulus value can be measured. Thus, whilst it may appear simple to adopt the storage modulus value of approximately 25 GPa that was stated by Zlopaša (approximated from Fig. 4.1) for 50% wt. Na-Alg and 50% wt. Nanoclay composites, the type of Na-Alg and Nanoclay used were different (Refer to Chapter 2 and Zlopaša's thesis [2]). What's more, according to Zlopaša, greater alignment of the Nanoclay within the polymer is expected to result from consistent exfoliation of the initial suspension over a period of 24 hours. In the case of the foams, this exfoliation was expected to be minimal as a consequence of either: the system being less fluid, or the limited timescale offered for exfoliation. This immediately prompted a reevaluation of the storage modulus of the nanocomposite films using the techniques and the materials used to produce the foams.

On the subject of accuracy, the ability to measure the elastic modulus of the foams depends solely on the type of experimental setup in place to measure the foam's modulus. This ability can be easily translated to the compliance that might exist in a particular setup. Thus the careful assessment of the compliance using predictable reference materials can provide an insight into the feasibility of relying on a particular set of results.

5.1 Methodology: Precision of Film Moduli

The composition of the type of films that were tested has been listed in Table 5.1. It should be noted here, that whilst a number of different production techniques and compositions were trialled with respect to baked and freeze-dried foams, it was not feasible to produce uniform films using these methods. Thus, only three distinct types of films were considered to represent each one of the production techniques.

The films were cast by pouring the suspensions into Petri dishes. They were subsequently allowed to dry in a well-ventilated fume hood (Temperature: 22 °C, Relative Humidity: 50%). The drying was continued until the thickness was expected to be between 100 and 200 μm. They were subsequently cut into strips whose length and width measured 20mm and 3mm respectively. They were then allowed to dry for a period of 24 hours in a vacuum oven at a temperature of 40 °C and stored in a desiccator filled with silica gel.

The samples were tested using the extension geometry setup of the Perkin Elmer DMA 7e Dynamic Mechanical Analyzer (DMA). Before any testing was carried out, however, the average thickness of each sample was measured to the nearest μm over five separate readings and, the mass of the samples was measured to the nearest tenth μg. As the storage modulus of the films in ambient conditions (Temperature: 24 °C, Relative Humidity: 50%) was of interest, the samples were loaded isothermally at a testing frequency of 1 Hz for 5 mins. To ensure consistency in testing amongst samples, their displacement amplitude was restricted to 2 μm.

Table 5.1: List of films produced

Representative Technique	**Composition (Wt. %)**	**Production**
Baking	1.5% Na-Alg + 1.5% Nanoclay + 0.33% Ammonium Bicarbonate + 96.67% Water	Mechanical Stirring + Refrigeration (4 °C) + Casting in Petri Dish + Ambient Drying (22 °C, RH = 50%)
Freeze Drying	1.5% Na-Alg + 1.5% Nanoclay + 97% Water	Mechanical Stirring + Refrigeration (4 °C) + Casting in Petri Dish + Ambient Drying (22 °C, RH = 50%)
Whipping	2.5% Na-Alg + 2.5% Nanoclay + 0.625% Calcium Carbonate + 50% of Carbonic Acid Soln. + 45% Water	Mechanical Stirring + Refrigeration (4 °C) + Mixing in Falcon Tube + Casting in Petri Dish + Ambient Drying (22 °C, RH = 50%)

5.2 Results: Precision of Film Moduli

The results from the testing of films have been depicted in Figs. 5.1, 5.2 and 5.3. What becomes apparent is the difference in the number of film strips that were tested. This difference, however, is purely based on the scatter that was noticeable in the data. In the case of films representative of the baked and freeze-dried samples (Figs. 5.1 and 5.2), the scatter was higher and thus, eight and ten film strips were tested respectively. In the case of the film representative of the whipped samples (Figs. 5.3), the scatter was lower and thus, only five film strips were tested.

Table 5.2: Storage Modulus values of the films

Representative Technique	**Max. Storage Modulus (GPa)**	**Avg. Storage Modulus (GPa)**
Baking	11	8.7
Freeze Drying	8.9	6.8
Whipping	7.9	7.1

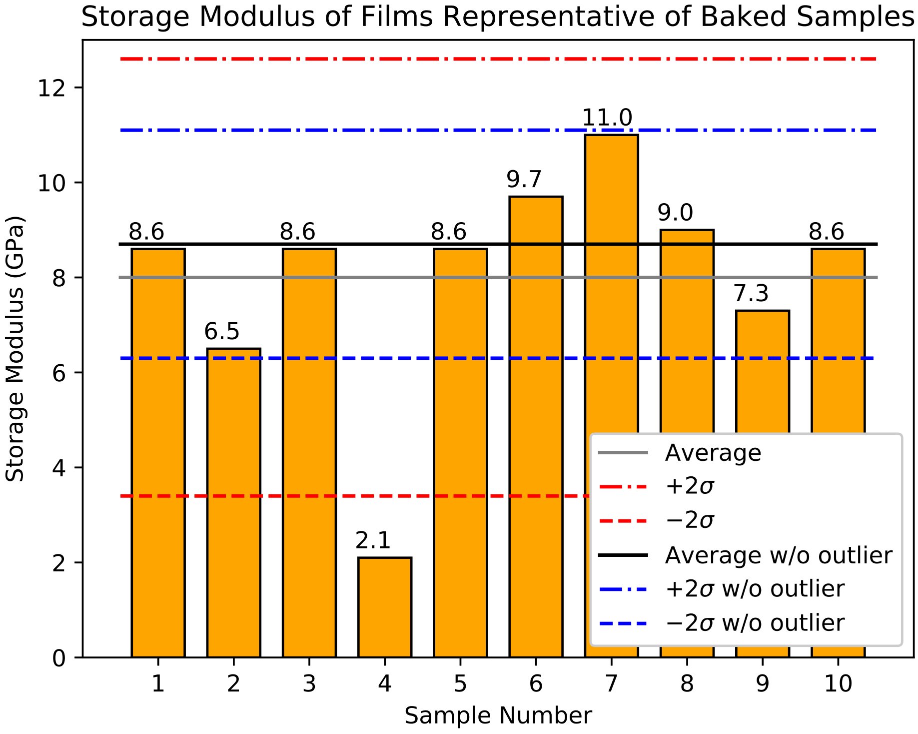

Figure 5.1: Results from films representative of baked Samples

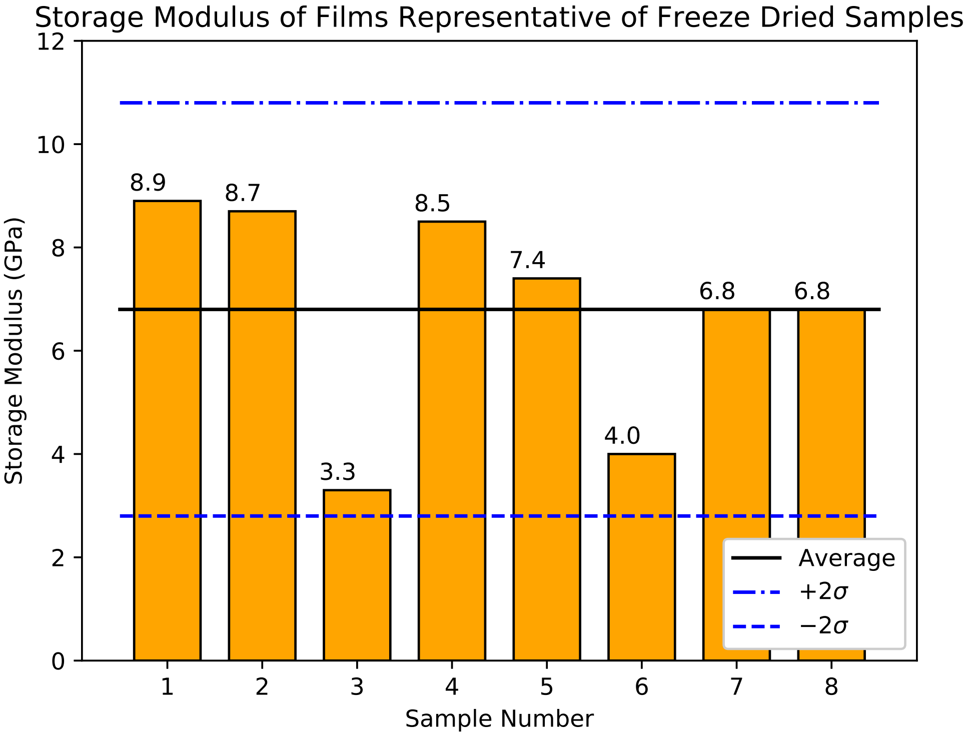

Figure 5.2: Results from films representative of freeze dried samples

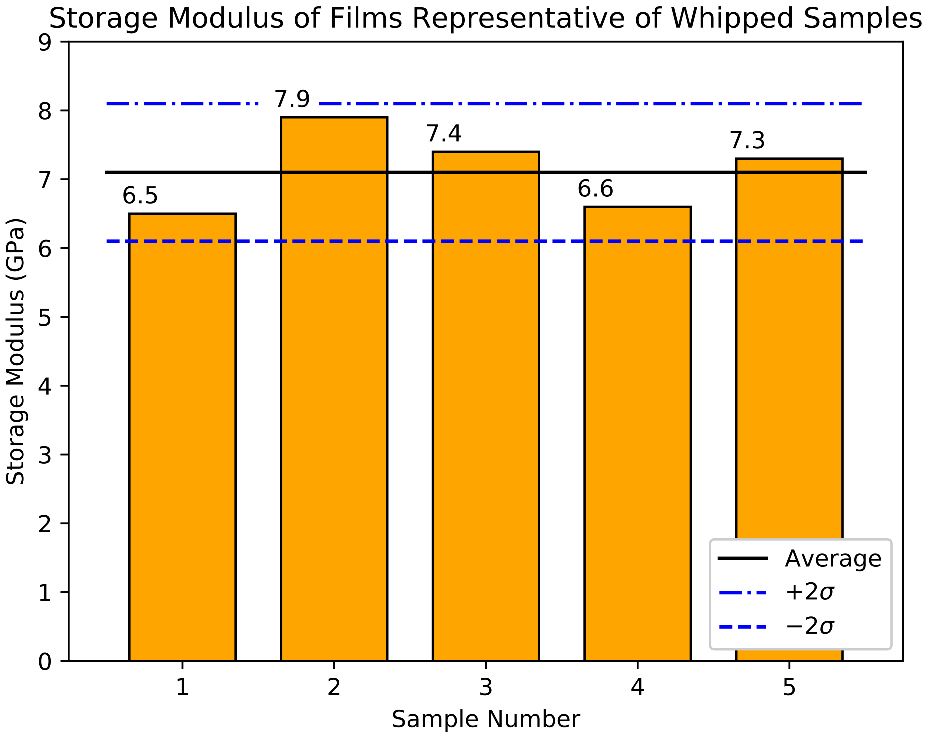

Figure 5.3: Results from films representative of whipped samples

The next discussion point is the storage modulus values themselves. Typically, when mechanical testing is carried out, a large number of samples are tested to account for the standard deviation in the data. Based on this statistical practice, the average value of the modulus is oftentimes recorded as being the modulus of the material. However, as mentioned earlier, biopolymer nanocomposites are susceptible to a number of different physical parameters. The most important amongst these being the moisture uptake. Thus, the average value of the storage modulus needn't represent the true modulus of a system that is prone to these changes. Under these circumstances, it would only make sense to consider the maximum value of the storage modulus as this looks at representing the ideal system. To faciliate the merits addressed by both schools of thought, it was considered fit to report both, the maxima values as well as the average values. These have been reported in Table 5.2. The maxima values that have been reported are straight forward to interpret. The ones describing the average values however need some clarification. Typically, the mean value for modulus is selected to suitably provide a high confidence interval for the values being reported. In the case of this study, twice the standard deviation from the mean value was regarded as being suitable as this looks at providing a 95% confidence interval. For the film's representative of the freeze-drying and whipping process, this was straight forward as no outliers were expected to be present. The results from plotting the 95% confidence interval also seem to suggest the same (Figs. 5.2 and 5.3). In the case of the film's representative of the baking process, the minimum value (2.1 GPa) was considered as being an outlier in the scatter. When this is considered to calculate the mean and the standard deviation, twice the standard deviation from the mean only represents a 90% confidence interval. However, when this value is negated from the calculations, the standard deviation window covers all the remaining values tightly to suggest a 95% confidence interval. Thus the average value was reported by considering the minimum value as being an outlier.

As Zlopaša's work involved the use of Na-Alg and not Ca-Alg, a direct comparison cannot be made with the film representative of the whipped samples. However, upon comparing the storage modulus values of the film's representative of the baked and freeze-dried samples with those stated by Zlopaša (Fig. 4.1), it is clear that the modulus has dropped more than half its value. As the drying methodology was kept consistent with his own methods, the drop in modulus is not expected to have resulted from the uptake of moisture. It thus is a result of either the level of exfoliation of the nanoclay or the purity of the individual constituents of the composite material. Between these two, it is expected that this drop primarily results from the level of exfoliation due to the drastic differences that exist between the suspension production techniques for the individual foams. These differences in exfoliation are expected to influence the effective aspect ratio of the nanoclay fillers thereby dropping their ability to reinforce the biopolymer matrix.

5.3 Methodology: Compliance of the DMA

It was believed that the DMA used to the test the films above, could also be used to test the foams using the parallel plate geometry. However, the measurement limit of the DMA in the parallel plate setup was unknown. As the elastic modulus of Polymethyl Methacrylate (PMMA) is well documented in literautre [47], and since it's modulus lies in the same order of magnitude as that of the films; a 5mm thick sample, with a diameter of 20mm was utilised to record the compliance of the DMA measurement setup.

The parallel plate setup of the DMA provided the leverage to interchangeably use different top plates. Since the effort here was to minimise the compliance during DMA measurements, it was understood that using a smaller top plate would increase the stress within the sample, thereby minimising the potential for compliance. Thus, a 5 mm diameter top plate was used to load the PMMA sample. In contrast, a 20 mm diameter plate was used as the bottom plate. The sample was loaded in ambient conditions (Temperature: 24 °C, Relative Humidity: 50%) using a static scan loading cycle designed to test materials using static stress. The sample was preloaded using a clamping force of 50 mN. The force was then increased linearly to 8000 mN at a rate of 500 mN/min. As the surface area of the sample was greater than the surface area of the top plate, it was possible to load the sample at five separate locations to obtain an average compliance value. Once the loading was complete, the linear region of the displacement v/s force curve was used to calculate the compliance.

5.4 Results: Compliance of the DMA

The results from the compliance measurements are depicted in Fig. 5.4; along with the linear best fit curve for the measurements. What becomes apparent here is the difference in the magnitude of displacements between measurements. These are expected to result from the improper mating between the top plate and the surface of the sample. This improper mating is expected to be a consequence of both, the asperities that exist on the sample's surface, as well as any skewness that may have resulted due to machining errors. However, as the slope remains consistent between measurements, these deviations are not expected to influence the compliance measurements themselves. Thus, the overall measured compliance of the PMMA sample was simply calculated from the slope of the best fit curve (0.002 mm/N).

As the PMMA sample and the DMA's geometry were loaded simultaneously, a series compliance model could be assumed. This meant that the compliance of the DMA's parallel plate geometry could be calculated eaily by subtracting the actual compliance of the PMMA sample from the value stated above. To prevent the risk of overestimating the compliance of the PMMA, the best case modulus value of 3.2 GPa was chosen [47]. This value was then inverted and subsequently converted from (1/GPa) units to (mm/N) units to yield a compliance value of 3.18x10^{-6} mm/N. As the effect of subtracting this value would have a minimal influence on the overall value, it was simply assumed that the compliance of the DMA's parallel plate setup was 0.002 mm/N for all future measurements.

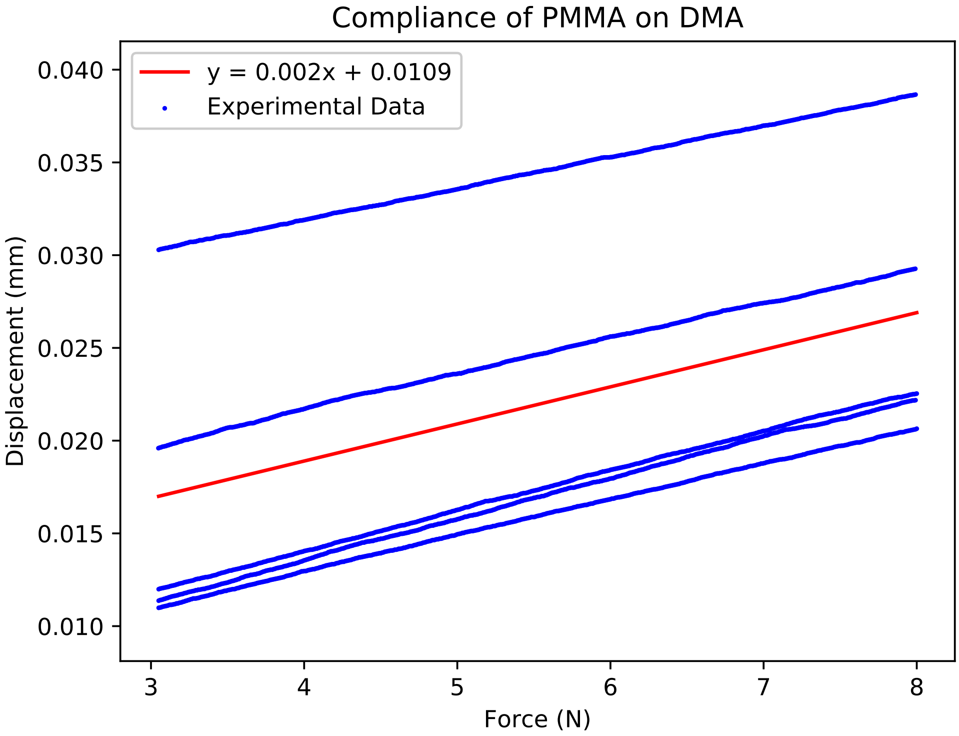

Figure 5.4: Compliance measurements on the DMA

Chapter 6

Results v/s Theory

In Chapters 4 and 5, the theoretical framework and the mitigation of experimental errors were discussed. It makes sense to then discuss how the mechanical characterisation study was carried out. The sections of this Chapter highlight the methodology adopted for this and discusses the final results that were obtained.

6.1 Methodology: DMA Testing

As discussed in Chapter 5, the parallel plate geometry setup of Perkin Elmer DMA 7e Dynamic Mechanical Analyzer (DMA) was deemed capable of characterising the foams. Also, as stated earlier in Chapter 2, the foam samples were post-processed to be tested. In the case of the baked foams, this was accomplished using a DREMEL 300 multi-tool system. To further facilitate the potential for a smooth contact between the sample and the top plate of the parallel plate setup, the top and bottom surfaces of the baked samples were also suitably post-processed using the DREMEL. The average diameter of the baked samples was approximately 20 mm. In the case of the freeze-dried foams, the samples were directly cast into a silicone mould with a diameter of 25mm. In the case of the whipped foams, the samples were post-processed using a 21 mm punch and a hammer. However, as the whipped samples were quite soft, care was taken to limit the potential for plastic deformation. The samples were then dried for 24 hours using a vacuum oven at a temperature of 40 °C. They were then sealed in a Petri dish using laboratory film and stored in a desiccator before testing.

The samples were tested using a 5mm diameter top plate and 20 mm diameter bottom plate. Before testing commenced, however, the average thickness and diameter of the samples were recorded over 5 measurements using Vernier callipers with a least count of 0.05mm. Subsequently, the mass of the sample was recorded to the nearest tenth μg. The samples were loaded in ambient conditions (Temperature: 24 °C, Relative Humidity:

50%) using a static scan loading cycle, designed to test materials using static stress. The samples were preloaded using a clamping force of 50 mN. The force was then increased linearly to 8000 mN at a rate of 500 mN/min. Once the loading was complete, the linear region of the force v/s displacement curve (below 4% engineering strain) was used to calculate the engineering stress and strain. From this, the elastic modulus of the foams was subsequently estimated. As the surface area of the sample was much greater than the top plate of the parallel plate setup, five measurements could be made on each sample. Table 6.1 lists the samples from Chapter 2 (Tables 2.1 and 2.2, whipped sample) that were successfully tested on the DMA.

Table 6.1: List of foams tested on the DMA

S No.	**Sample ID**
1	Freeze Dried-1
2	Freeze Dried-2
3	Freeze Dried-3
4	Freeze Dried-4
5	Freeze Dried-6
6	Whipped
7	Baked-1
8	Baked-8

6.2 Results: DMA Testing

For the convenience of the reader, the results have been broken down into two subsections, one describing the results of the freeze-dried and whipped foams, the other describing the results of the baked foams.

6.2.1 Freeze Dried and Whipped Foams

Fig. 6.1 represents the elastic moduli values of freeze-dried and whipped foams; before and after the compliance of the measurement setup was accounted for. As each sample was tested five times, there are multiple elastic modulus values that were recorded for the same relative density value. Analogous to what was stated earlier for the PMMA sample in Chapter 5, the scatter in the data here is expected to result from the surface asperities and the skewness of the top surface of the sample. In cases where the contact area is maximised, the sample would exhibit a heightened internal resistance and thus, a greater modulus. This allows for the underlying assumption to be made that the greatest modulus value for each sample truly represents the elastic modulus of the foams; as a relatively smooth contact was achievable between the top plate and the surface of the sample.

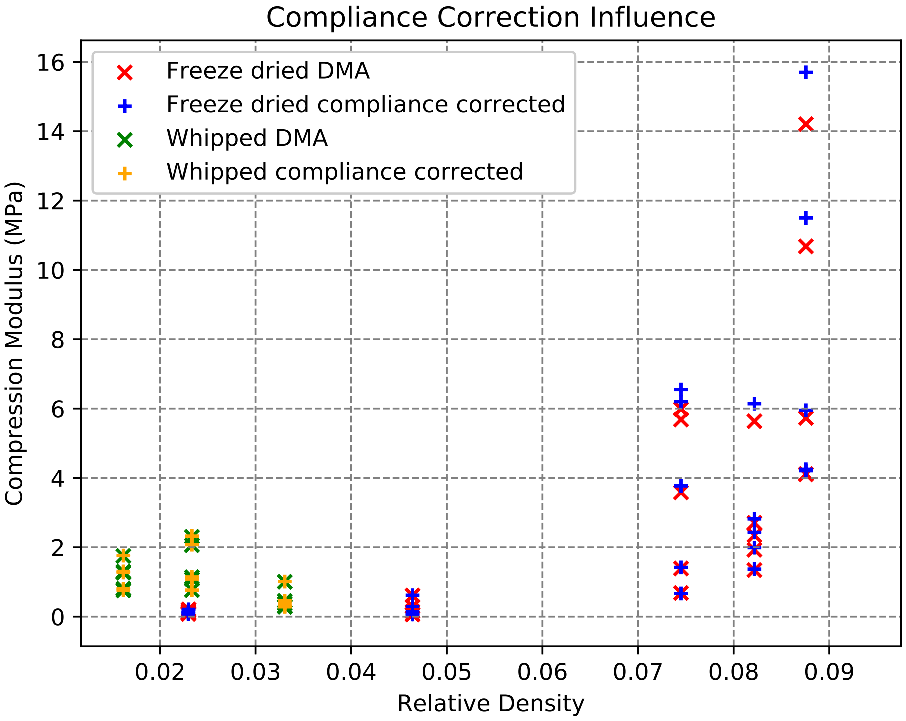

Figure 6.1: DMA Results of freeze dried and whipped foams- With and without the compliance correction

The compliance correction seems to have minimal influence on the recorded elastic moduli of the freeze-dried and whipped foams. The effect of these corrections only seems to majorly influence the elastic modulus of the higher density freeze-dried samples. Thus, an easy consolidation of the trends noticeable in the modulus can be made. Based on the results that were recorded for whipped foams, the samples seem to exhibit an elastic modulus roughly between 1 and 2 MPa. Although the scatter in the elastic modulus of the whipped foams is minimal, the scatter in their relative density is higher. This is a result of the larger voids that are a characteristic feature of the whipped foams. As the distribution of these large voids is fairly random within the whipped sample, it is possible for the smaller sized samples (like the ones being tested on the DMA) to exhibit slight differences in their relative density values. When assessing the results for freeze-dried foams, however, it seems that the lower density samples are only capable of recording elastic modulus values of a few hundred kilopascals. However, in the case of higher density freeze-dried samples, the elastic modulus values are drastically improved and lie between 6 and 16 MPa. Unlike the whipped samples, a means of stabilising the foam was not provided for the freeze-dried samples. It is thus believed, that at the very low densities, the structural integrity of the sample is compromised resulting in collapsed structures within the foam. This hypothesis, however, needed further verification and shall be discussed in the subsequent sections of this Chapter.

6.2.2 Baked Foams

Fig. 6.2 represents the elastic modulus values of baked foams; before and after the compliance of the measurement setup was accounted for.

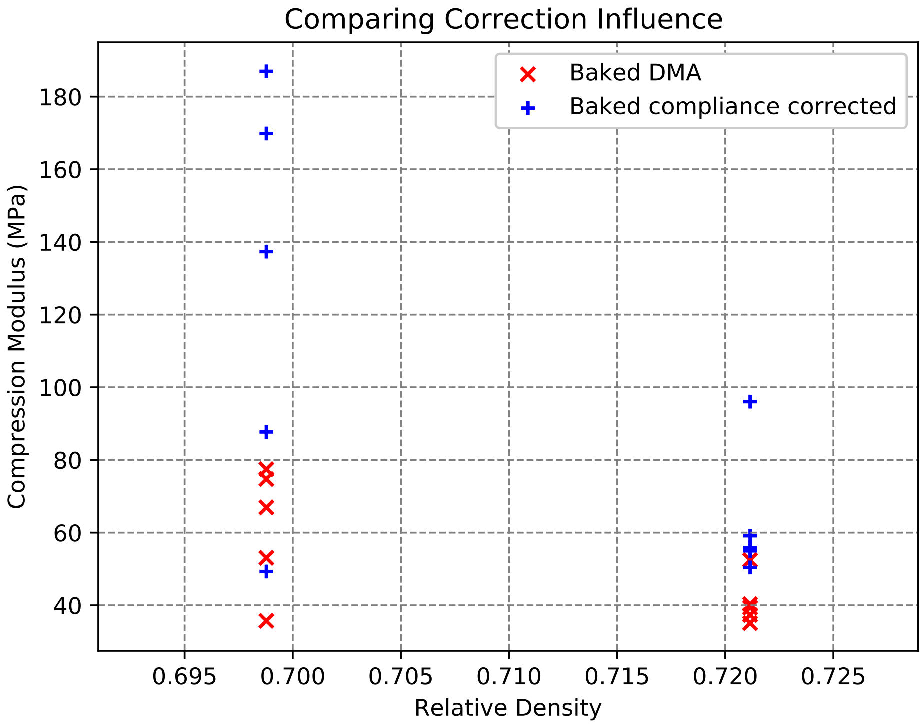

Figure 6.2: DMA Results of baked foams- With and without the compliance correction

Similar to the results that were obtained for whipped and freeze-dried foams, each sample was tested five times on the DMA. Thus, multiple readings were noted for the same relative density value and again, the maxima amongst these values were considered as being representative of the foam's elastic modulus. The primary observation that can be made is the jump in the modulus value after the compliance correction has been accounted for. In both the samples, the modulus jumps by nearly twice its original value. As the baked samples are much stiffer than the freeze-dried and the whipped samples, it is expected that this jump results from the lower compliance that the sample exhibits. For the modulus values recorded here, the compliance during measurement translates approximately to the order of 1x10^{-4} mm/N. Since this is only one order of magnitude below the 0.002 mm/N value that was recorded earlier (Chapter 5), it is expected to greatly influence the results and thus, the uncertainty associated with the measurements.

And so, it was believed that an alternative method had to be adopted to ascertain the elastic modulus values of the baked foams.

6.3 Methodology: Zwick Z100 Testing

An alternate strategy for compression testing of baked foams was trialled using a Zwick Z100 testing machine. As the machine is capable of exerting a load of up to 100 kN, it was believed that the issues pertaining to the compliance could be easily overcome.

ASTM Standards D1621 and D6108-19 were used as guidelines to test the baked sample. Based on these standards, the engineering strain within the sample was measured using the crosshead displacement. The samples were loaded using a 3% engineering strain rate. The elastic modulus was estimated automatically by the measurement setup using the textXpert II (Version 3.6) software. All the baked foams (Table 2.1, Chapter 2) were tested using this method in an attempt to retain a large number of data points.

6.4 Results: Zwick Z100 Testing

Fig. 6.3 represents the results that were obtained using the Zwick Z100 machine alongside the results that were obtained from the DMA for the baked foams.

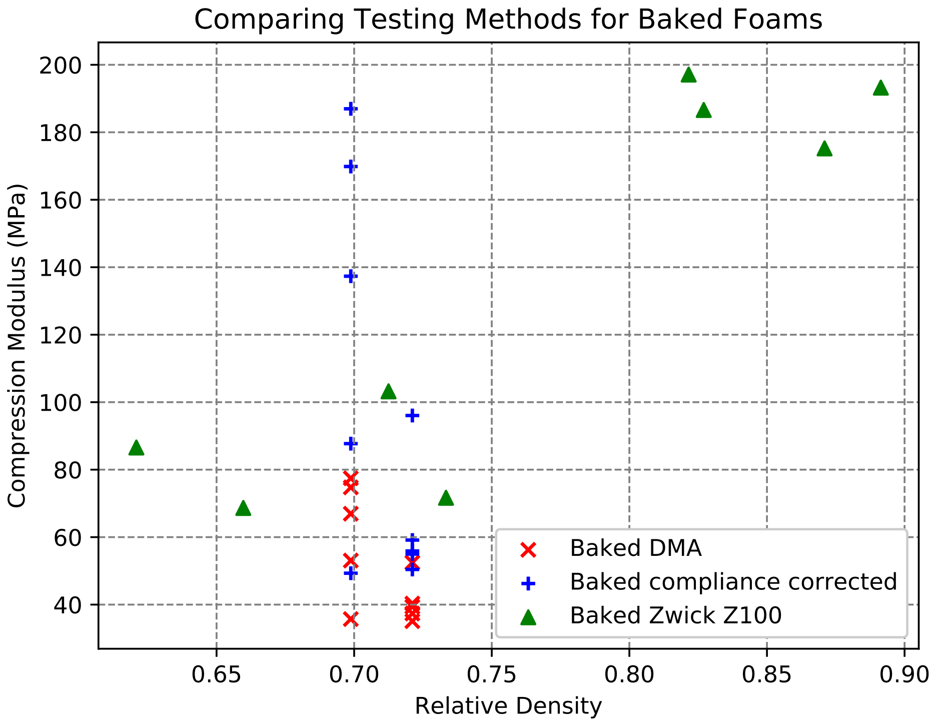

Figure 6.3: Mechanical testing of baked foams- With and without the compliance correction (DMA) and differences in testing methods

It is clear from this graph that the previous challenge had been overcome to provide two sets of readings for the baked foams. A lower density set, whose elastic modulus values are between 60 and 110 MPa and a higher density set, whose elastic modulus values are between 170 and 200 MPa. When these values are compared with the compliance corrected values from earlier, it becomes clear that there was definitely a very large uncertainty associated with the values that were obtained for baked foams from the DMA testing earlier. Finally, since the entire top surface of the sample was loaded uniformly, the scatter in the Zwick Z100 testing data is expected to have resulted from the skewness of the samples.

6.5 Comparison with Theory

So far, only the individual results were discussed for the foams. It now becomes important to compare these results with the theoretical predictions from Chapter 4.

Fig. 6.4 depicts the experimental results being overlayed over the theoretical estimation provided by Gibson and Ashby. The relative modulus v/s relative density scatter was calculated using both, the maxima and average storage modulus values of the films, the elastic modulus values that were recorded for baked foams using the Zwick Z100 testing machine and the maximum compliance corrected elastic modulus values for freeze-dried and whipped foams. The NFC-MMT scatter represents the results that were obtained for isotropic, freeze-dried nano fibrillated cellulose - montmorillonite clay (NFC-MMT) foams [11]. It immediately becomes clear that the differences between using the maxima and the average storage modulus values seem to be negligible. On the other hand, the results for the biopolymer nanocomposite foams fall well below Gibson and Ashby's predictions for both open as well as closed-cell foam materials. This drop in relative modulus is to be explained and thus, it becomes important to highlight the subtle details that accompany this drop.

To begin with, the scatter for the whipped samples (relative density: 0.01 to 0.04, relative modulus: 1x10^{-4} to 4x10^{-4}) overlaps with the scatter that was observed by Gibson and Ashby themselves. As it is easy to ascertain that the samples are indeed open-cell foams, it is expected that the scatter for whipped foams obeys theoretical predictions closely.

On the other end of the spectrum, it is noticeable that the relative density of baked foams is almost equal to 1. At these relative density values, the samples must start exhibiting the modulus of the inherently stiff nanocomposite material. However, it is clear that this value falls well below the storage modulus of the film's representative of the baked sample approximately by a factor of 0.02. A list of sensible reasons as to why this drop in the relative modulus is observed would include the limited exfoliation of nanoclay due to hand mixing, the residual moisture that might exist within the sample due to the inconveniences associated with the drying and the potential existence of micro or nano-sized cracks in samples that are otherwise consistently characterised by cracks observable with the naked eye. Although a lower degree of exfoliation is expected to impact the storage modulus value, it would only drop the modulus value down to that of the Na-Alg polymer, due to the inability of the nanoclay fillers to reinforce the polymer matrix. Thus, amongst the reasons listed above, the presence of the cracks and the moisture that is retained within the sample are expected to be the major reasons for the drop in the relative modulus.

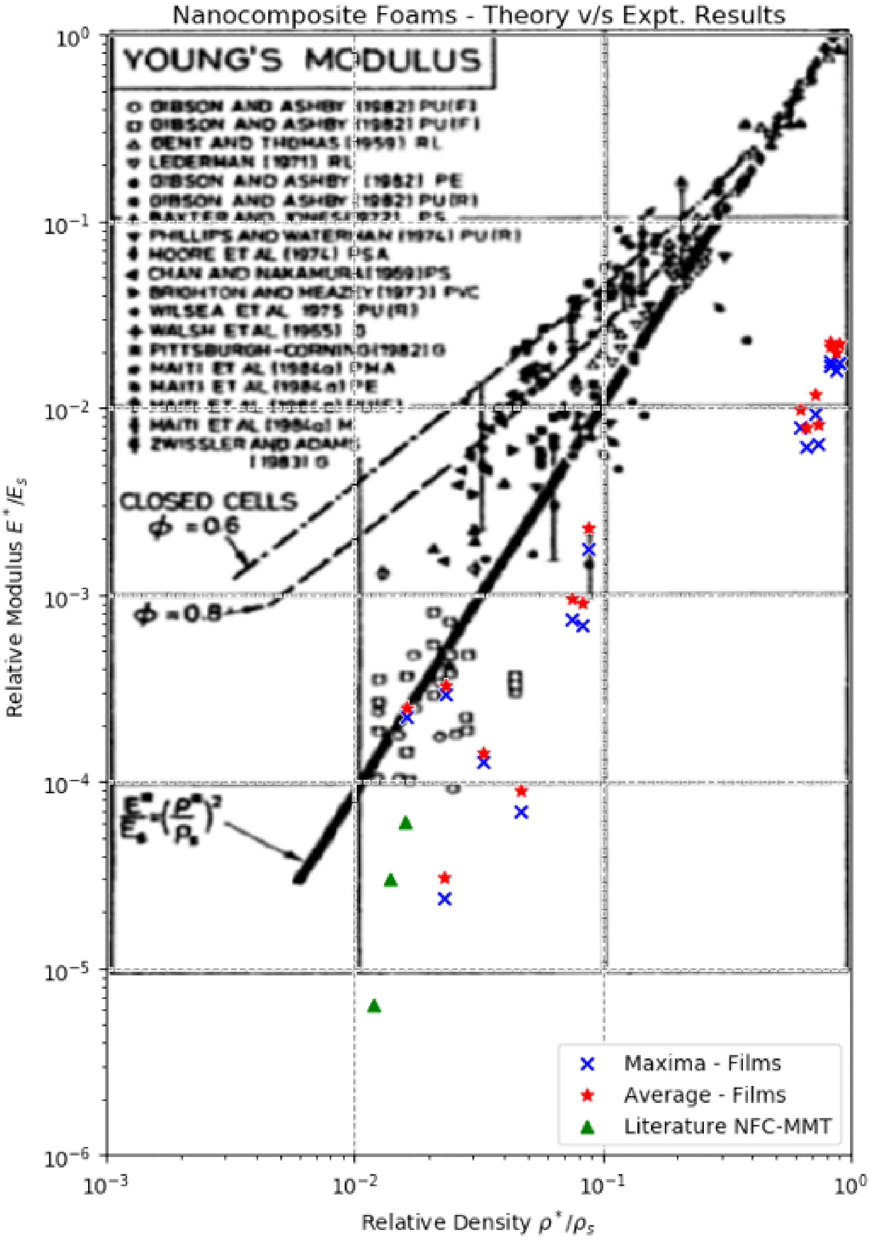

Figure 6.4: Comparing experimental results with theoretical predictions [5]

The major points of departure from the theoretical estimations include the relative modulus values that was observed for the freeze-dried foams (relative density: 0.01 to 0.1, relative modulus: 1x10^{-5} to 1x10^{-4} and; relative density: 0.07 to 0.09, relative modulus: 6x10^{-4} to 3x10^{-3}). However, upon comparing these values with the ones observable for NFC-MMT nanocomposite foams, it is clear that these values could highlight similarities with trends observable in other experiments. In the case of NFC-MMT foams, the potential existence of interpenetrating or loosely connected structures was explained (Fig. 6.5). If such structures persist within the foam, then their ability to act as strut or membrane-like structures considerably drops. To that effect, it became important to analyse the samples using a JEOL JSM-6010LA Scanning Electron Microscope. Whilst it was not possible to extract samples from the freeze-dried samples that were tested,samples with the same solid mass percentages which were prepared using a 5% ethanol solution insted were analysed (preparation analogous to Freeze Dried-6 sample - Table 2.2) . The results have been depicted in Figs. 6.6, 6.7 and 6.8. It becomes clear that there is an absence in the regular presence of strut or membrane shaped elements for the 2.5% and 5% wt. concentration samples. However, when the solid mass percentage within the sample is increased to 10% (Freeze Dried - 6, Table 3.2), regular cell-like ordering within the sample is noticeable. These results are consistent with the trends that are observable in the relative modulus v/s relative density plot. Whilst the deviations are larger in the case of the lower density freeze-dried foams, the presence of the regular cell-like structures in the case of the higher density freeze-dried foams reduces the deviation to within one order of magnitude from the theoretical estimations for open-cell foams. However, since the SEM images indicate the presence of closed-cell foam structures, it becomes easy to suggest the inability of the freeze-drying process to produce consistent strut or membrane-like morphologies within the cells of the foam.

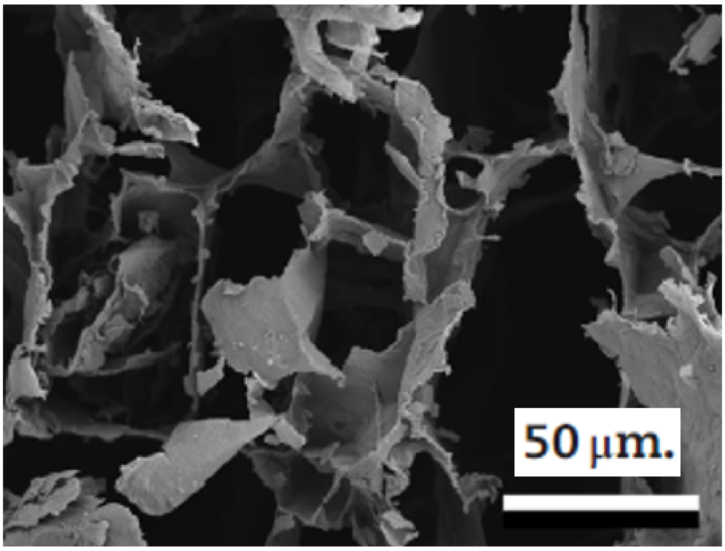

Figure 6.5: SEM image of freeze dried NFC - MMT foams [11]

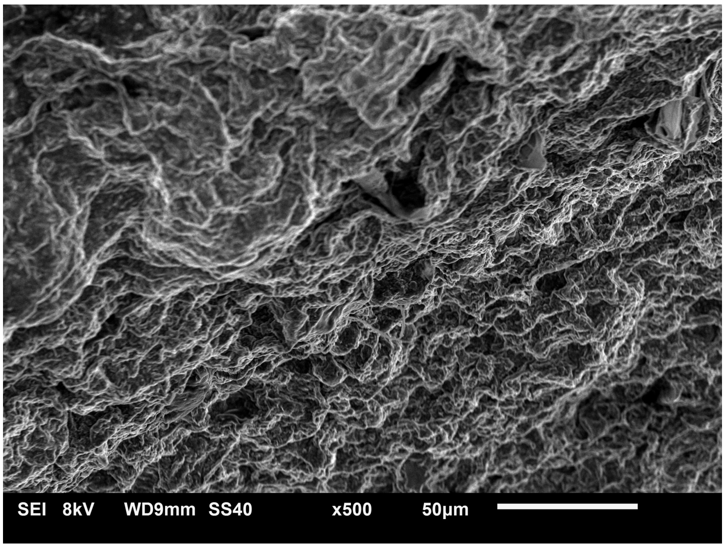

Figure 6.6: SEM image of 2.5% wt. freeze dried foam

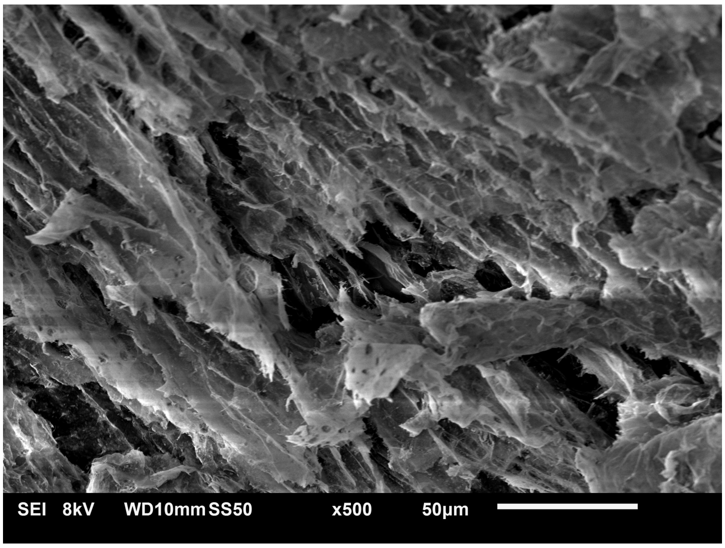

Figure 6.7: SEM image of 5% wt. freeze dried foam

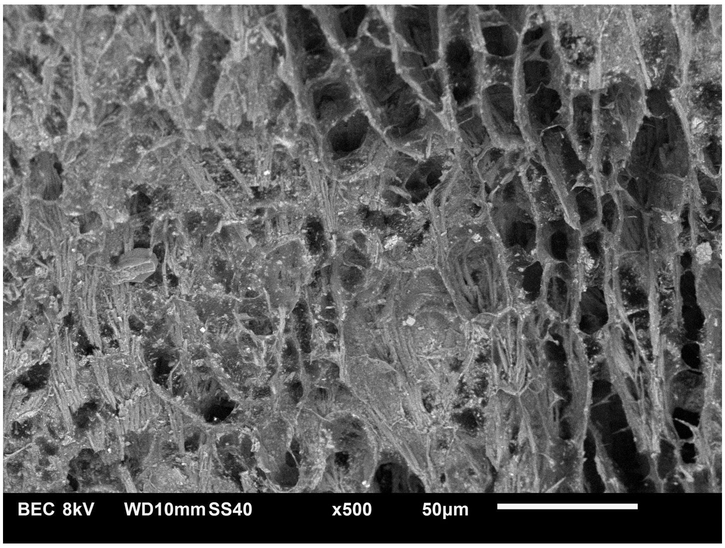

Figure 6.8: SEM image of 10% wt. freeze dried foam

Chapter 7

Conclusions and Recommendations

This study was focussed on the development and characterisation of foam-like cellular structures that are based on sodium alginate biopolymer and montmorillonite nanoclay composites. The work carried out over the course of this study looked at establishing the viability of using these biopolymer nanocomposite foams as hypersonic heat shields aboard Delft Aerospace Rocket Engineering's future sounding rocket missions.

7.1 Conclusions

After carefully assessing the results from this study, it is possible to draw the following conclusions:

1. Simple production techniques such as baking, freeze-drying and whipping offer methods by which biopolymer nanocomposite foams of different relative densities can be produced. It was possible to use all three methods to produce foams with relative density values spanning from a minimum value of 0.017 to a maximum value of 0.891.

2. The process of turning nanocomposites into foams does not seem to detrimentally impact their ability to function a flame retarding materials. Upon qualitatively assessing these foams, it is clear that they outperform existing cork based heat shields. Quantitatively speaking, these foams were capable of offering a temperature gradient between $1.5\text{x}10^5$ and $3.2\text{x}10^5$ K/m when exposed to a high-temperature propane-butane torch flame for 2 mins. These values are comparable with the temperature gradient offered by the high-temperature tile-based Thermal Protection Systems aboard NASA's Space Shuttle Orbiter.

3. Whilst it is easy to say that the preliminary thermal characteristics and the ease with which the foams can be produced guarantees their ability to work as hypersonic

heat shields, it becomes important to assess the mechanical behaviour of these foams in order to guarantee their use as/within structural components. This was identified as being rather elusive due to the inconsistencies that were noticeable in existing analytical/numerical models to estimate the elastic modulus of foams. By elaborative reasoning from first principles using the Halpin-Tsai equation however, similarities can be observed with the Gibson and Ashby model [5] for foams.

4. After carrying out an extensive mechanical characterisation regime, it has been understood that the Gibson and Ashby model is fit enough to accurately estimate the relative modulus of whipped foams. The scatter in the data coincided with the trend line and the existing scatter for open-cell foams.

5. Deviations from the Gibson and Ashby model were observed in the case of baked foams and freeze-dried foams. In the case of the baked foams, these have been primarily attributed to the potential for moisture retention and the micro or nano cracks within the foam. Additionally, limited exfoliation of the nanoclay within the foam due to hand mixing was also regarded as being another reason. In the case of the lower density freeze-dried foams, this has been attributed to the inability of the freeze-drying process to produce well connected cellular structures capable of providing an internal resistance to compressive loads.

6. Amongst the production techniques listed here, it seems that whipping bears the closest resemblance to the conventional extrusion-based production techniques for polymer foams. Although not explicitly stated, this could mean that the Gibson and Ashby model is limited to characterising foam morphologies that are produced using the extrusion techniques. This would serve to explain why the best-fit curves utilised by them, disregard the effect of the shape of the cells. Thus, the Gibson and Ashby model is coerced by the limited experimental data that is available on all potential cellular solids that can be classified as foams.

7. Finally, it becomes important to understand the elastic modulus values of the foams themselves. The best values of the elastic modulus that the baking, freeze-drying and the whipping processes yielded were 197.11 MPa, 15.7 MPa and 2.32 MPa respectively. These values serve to represent the basis against which future mechanical characterisation results can be compared.

7.2 Future Recommendations

Based on these conclusions, the following recommendations can be made for future research in this subject area:

1. So far, samples were only made in an attempt to primarily characterise them and thus, were limited in size. In the future, the volume of the foams produced can be scaled up. This should look at providing an insight into the challenges associated with large scale handling and production.

2. In this study, foam materials with single relative densities were considered of importance to understand the underlying properties. But since it is now understood that the production techniques offer great versatility when it comes to the properties of biopolymer nanocomposite foams themselves, a stacked structure using foams of different densities can also be trialled.

3. As the baked foams consistently provide the best results, there's enough reasons to suggest a more consistent grasp of their mechanical properties. Amongst the reasons listed for deviations in the baked foams' elastic modulus values, it is hard to gain consistent control over the amount of moisture present within the sample or the cracking within the foam. However, the level of exfoliation can be studied closely. To that effect, a detailed X-Ray Diffraction (XRD) study can be carried out to understand how changes brought about to the baking process can improve the exfoliation of the nanoclay. Although limited control can be expected over the cracking, tomography scans could also reveal an improved insight into the distribution of these cracks within the baked foams.

4. So far, only the static - elastic compressive modulus of the foams have been evaluated. However, for a system as dynamic as entry into the Earth's atmosphere, multiple load cases persist. It then becomes important to assess the behaviour of these foams when loaded flexural, or in shear, or using an oscillating load. These load cases serve to highlight the likelihood of failure of the foams when utilised structurally and address the limitations of the foam.

5. The development of the numerical simulation of foams forms the basis for extensive modelling in the future. The development of filler based composite foams that are susceptible to mixed loading modes would definitely prompt the simplification of numerical simulations. The simplification of the foam geometry would then serve as the ideal starting point to help improve the efficiency of these simulations.

6. Only the thermal gradient that develops as a result of exposure to high temperatures was considered of importance in this study. This property was expected to critically define the dimensions and densities that become suitable for future considerations. However, understanding the heat capacity of these foams at different temperatures and different purge environments could also prove useful. This would help in assessing their thermal characteristics in different atmospheric conditions, by understanding their underlying chemical changes.

7. Finally, a detailed in-flight testing regime aboard a suitable sounding rocket would not just serve as a demonstration mission, but also provide suitable testing data under different flight conditions.

Appendix A

This Appendix looks at providing the reader with a visual representation of the failed attempts that were encountered during production. The Appendix has been broken down based on each individual production technique.

Baking

Figs. A to C represent the effect of changing the concentration of ammonium bicarbonate on the morphology of the baked foams. Amongst these samples, Fig. B represents the ideal 10% wt. (w.r.t. solid mass) conc. that was finally adopted. In the samples represented in Figs. A and C, this concentration was maintained at 5% and 15% respectively. It was not possible to conclude anything directly from these samples as a baking temperature of 160 °C was used to produce them. This is expected to have resulted in uncontrollable nucleation within the sample, thus leading to the development of very large voids.

Figs. D to K represents the effect of the uncontrolled departure of water from the sample. The solutions that were tried to combat this problem include reducing the baking temperature to 140 °C (Fig. D), unsuccessfully scoring the surface of the sample (Figs. E, F and G), use of isopropanol and butanol as plasticising agents (Figs. H and I) and improperly covering the sample with insulating materials (Figs. J and K).

Figs. L to O represent the result of somewhat baking the samples successfully using insulating materials such as paper (Fig. L and M) or silicone mat (Fig. N). In all of these cases however, imperfections such as the paper sticking to the sample's surface (Fig. L) or warping due to the development of temperature gradients (Fig. M) were noted. Finally, irrespective of the choice of material it was realised that covering the entire surface of the sample aids the baking process (Fig. N). However, since the sample, in this case, was post-processed to a small size simply to gauge the consistency in morphology, its dimensions did not offer viability for testing and were thus, still considered as a failure.

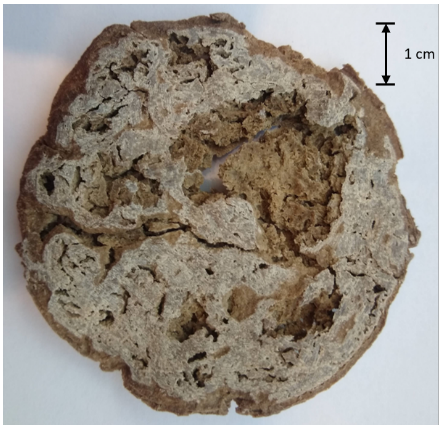

Figure A

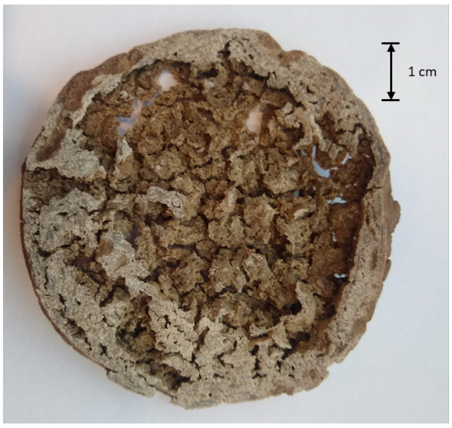

Figure B

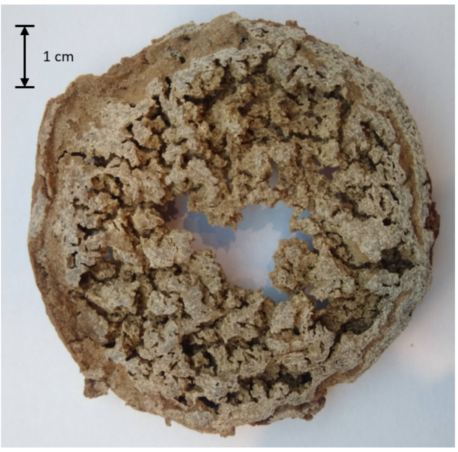

Figure C

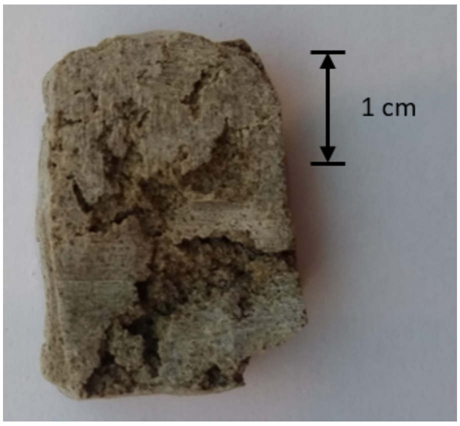

Figure D

Figure E

Figure F

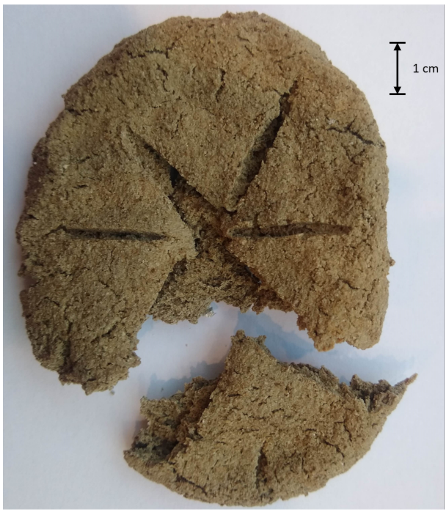

Figure G

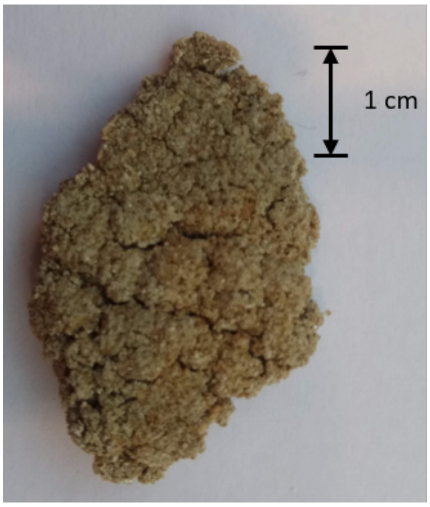

Figure H

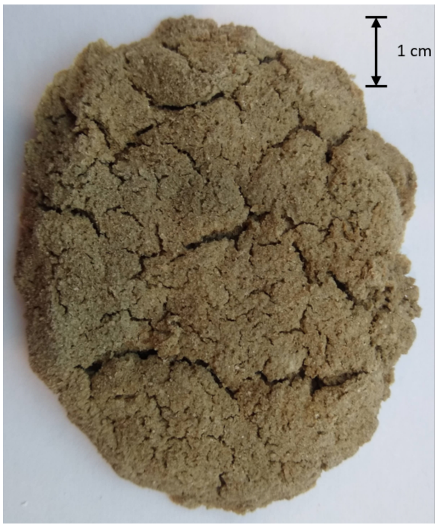

Figure I

Figure J

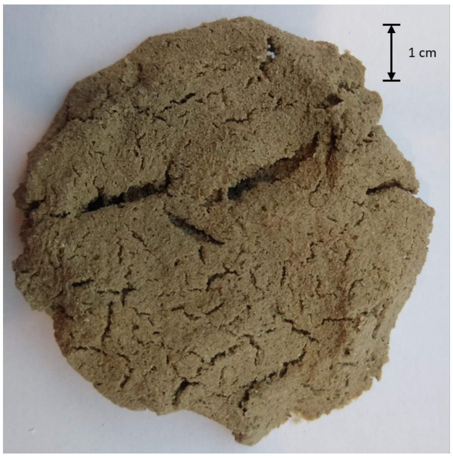

Figure K

Figure L

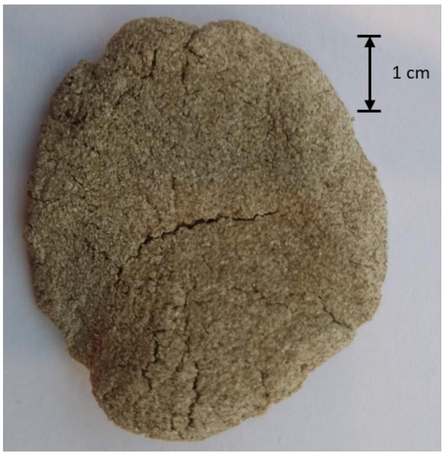

Figure M

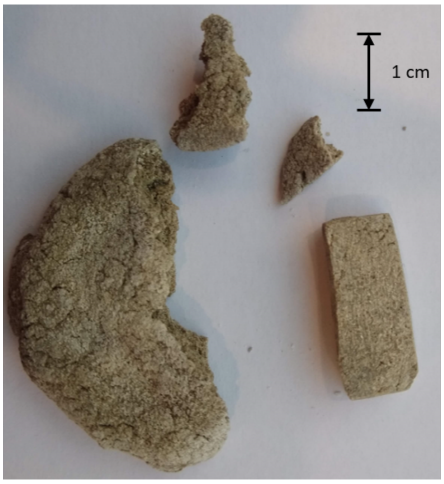

Figure N

Freeze Drying

Figs. O to S represent the results of flash freezing the samples using Liquid Nitrogen. Although multiple attempts were made to perfect the technique, the rapid onset of ice crystal nucleation due to the sudden drop in temperature, leading to the formation of thermal embrittlement of the sample; culminating in the formation of large cracks. It was believed that despite the cracks, consistency in morphology could still be attained (Figs. O, P and Q). However, this assumption was quickly dismissed upon noticing improper departure of moisture from within the sample (Figs. R and S). This led to the development of the characteristic wet spots within the sample.

Figure O

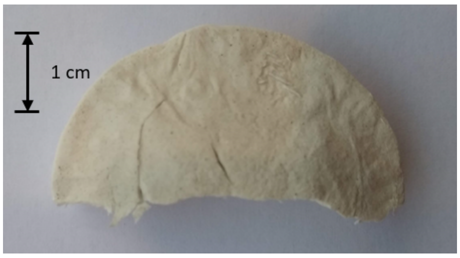

Figure P

Figure Q

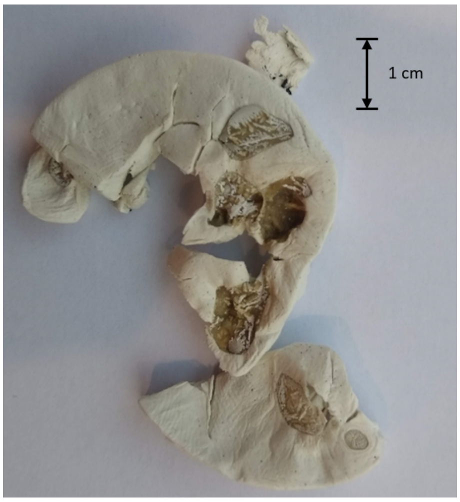

Figure R

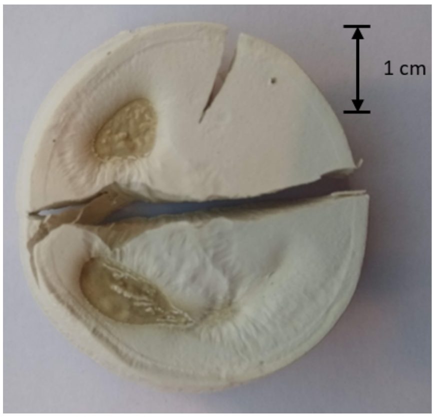

Figure S

Whipping

Figs. T and U represent the attempts of drying the low density and high-density samples in the ambient conditions of the fumehood (Temperature = 22 °C, Relative Humidity = 50%) respectively. In both cases, these samples were dried after the exchange of solvent to isopropanol. The results are self-explanatory, in that they describe the collapse of the foam structure upon drying them in ambient conditions.

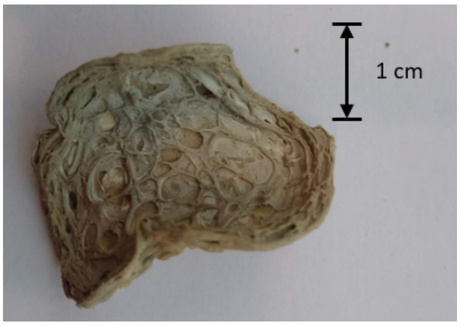

Figure T

Figure U

Appendix B

This Appendix provides the reader with insight into the CIE 1931 colour space and how the values translate to meaningful temperature values on the colour space chromaticity diagram.

Although advances are being made in an effort to capture and reproduce all the colours that lie within the visible spectrum of electromagnetic radiation, the limitations of the devices that work with visible light allow them to only truly interpret a subset of these colours. These limitations typically stem from the capabilities of the sensors in use or, the limited number of bits available to digitally represent colours. Thus, in an effort to efficiently represent a broader spectrum of the visible colours electronically, non-linear operations involving the addition of the primary colours (red, green and blue) are sought to create a usable digital colour space. One of the most prevalent non-linear colour spaces used to represent these colours is the Standard RGB (sRGB) colour space [48]. Thus, when photographs are assessed digitally, it becomes very easy to extract these sRGB values.

In reality, the addition of the primary colours preserves linearity. And so, whilst the sRGB values provide a convenient means to extract colours digitally, they do not accurately resolve the wavelengths into values that can be added linearly. Fortunately, however, standardisation of colour was already sought in the year 1931 by the International Commission on Illumination (CIE) [49]. The result is a linear colour space called the CIE xy chromaticity colour space. The advantage of using this colour space is that it permits linear transformations between its values. Thus, the values that are used to represent the chromaticity (or hue) of visible colours of light can be easily added to result in a new colour that is still perceivable by the average human eye. Also, because the CIE xy values have prevailed longer than the sRGB values, the latter scale's values can easily be converted to those of the former scale.

It now becomes important to explain the correlation between the CIE xy chromaticity colour space and colour temperatures. Typically, when a black body emits radiation, the hue resulting from the emission strictly adheres to the temperature at which the emission occurs. Thus, it provides an easy method by which the black body emission's colours can be correlated with the temperature of the black body's surface. This correlation is called the black body's colour temperature. However, an important parameter is worth considering to improve the accuracy with which the colour temperature estimation can be made. The colour temperature value is influenced not only by the temperature of the black body but also by the ambient illumination under which the emission is observed. Changes to the ambient lighting conditions, for example, influences the final wavelength value being measured. Thus, the CIE has provided illumination standards that serve to ensure consistency in the final interpretation of the colour temperature values. Amongst these, the D65 illuminant looks at best describing the open air, average midday light in western and northern Europe. On the basis of this standard, white light is perceived as being at a colour temperature value of 6500 K. This serves to explain why the camera was set to a white balance of 6500 K before any photos were taken. Once this was done, the rest of the experimental procedure could commence as intended.

Fig. V [50] provides a visual representation of the CIE xy chromaticity color space. The values stated on the periphery of the colour space correspond to wavelengths within the visual spectrum. For the sake of clarity, Fig. V also looks at representing the sRGB colour space and the temperature values that result from black body emissions. This looks at highlighting the details discussed earlier through visual means.

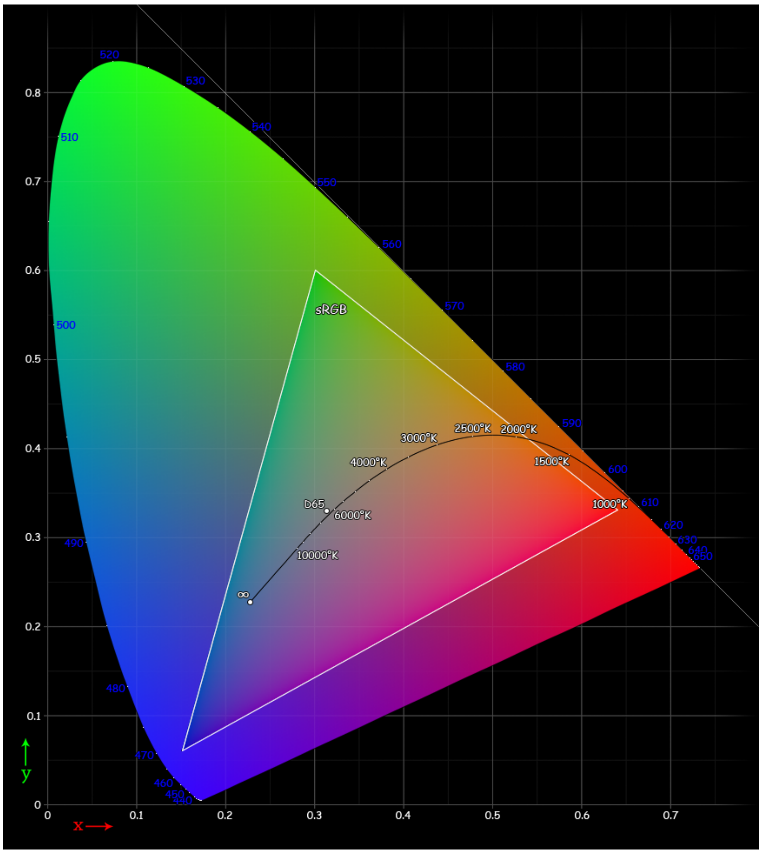

Figure V: [50]

Appendix C

This Appendix looks at enlisting the reader with the Python scripts that may become necessary to model idealised foam geometries in the future using FEniCS. The code is commented in detail and should already be clear to the reader. However, it is also recommended that the reader go through the textbook authored by Langtangen and Logg [46] for the sake of clarity.

```python
# Created by : Anand Raja, MSc. Materials Science and Engineering

# This python file describes the method by which simple open cell cubic
# geometries can be generated using FEniCS. The code below generates a
# 3 layered cubic lattice like network of staggered cubes (analogous to
# the one described by Gibson and Ashby). As with any FE solver, the
# values entered here are dimensionless and so, can be adjusted to suit
# a suitable length scale. It should also be noted here that the warning
# labels whilst using an IDE occur quite frequently.



# The first few lines of code imports the general FEniCS modules as well
# as the meshing modules.

from fenics import *
from mshr import *

# FEniCS's inbuilt Box function is being used here to generate the
# geometry

# First a solid 3D box is created in the domain where the foam is
# desired

b1 = Box(Point(0,0,0),Point(3,3,3))

# Next boxes need to be created to represent the voids within the foam.
# This can be carried out systematically.

# First 3 boxes are created parallel to the y axis.
```

```

b2 = Box(Point(0.065,0,0.065),Point(0.935,3,0.935))
b3 = Box(Point(1.065,0,0.065),Point(1.935,3,0.935))
b4 = Box(Point(2.065,0,0.065),Point(2.935,3,0.935))

# Then 3 new boxes are created parallel to the x axis.

b5 = Box(Point(0,0.065,0.065),Point(3,0.935,0.935))
b6 = Box(Point(0,1.065,0.065),Point(3,1.935,0.935))
b7 = Box(Point(0,2.065,0.065),Point(3,2.935,0.935))

# By the end of this process, the bottom layer of our foam is created.
# So a boolean operation can be performed to extract the voids in the
# bottom layer.

# In case this process is unclear, it is easy to comment out different
# sections of code to understand how the geometry looks after each
# boolean operation.

geo = b1 - b2 - b3 - b4 - b5 - b6 - b7

# The same process is repeated for the second layer. But now, its
# staggered to accomodate the geomtery proposed by Gibson and Ashby

b8 = Box(Point(0,0,1.065),Point(0.435,3,1.935))
b9 = Box(Point(0.565,0,1.065),Point(1.435,3,1.935))
b10 = Box(Point(1.565,0,1.065),Point(2.435,3,1.935))
b11 = Box(Point(2.565,0,1.065),Point(3,3,1.935))

b12 = Box(Point(0,0.065,1.065),Point(3,0.935,1.935))
b13 = Box(Point(0,1.065,1.065),Point(3,1.935,1.935))
b14 = Box(Point(0,2.065,1.065),Point(3,2.935,1.935))

geo = geo - b8 - b9 - b10 - b11 - b12 - b13 - b14

# Again its a question of repeating the process for the third layer.
# This time, the layer is kept parallel to the first layer to yield
# an AB-AB like lattice structure

b15 = Box(Point(0.065,0,2.065),Point(0.935,3,2.935))
b16 = Box(Point(1.065,0,2.065),Point(1.935,3,2.935))
b17 = Box(Point(2.065,0,2.065),Point(2.935,3,2.935))

b18 = Box(Point(0,0.065,2.065),Point(3,0.935,2.935))
b19 = Box(Point(0,1.065,2.065),Point(3,1.935,2.935))
b20 = Box(Point(0,2.065,2.065),Point(3,2.935,2.935))

```

```
geo = geo - b15 - b16 - b17 - b18 - b19 - b20

# So far, the voids parallel to the x and y axis were created. Now it is
# a question of systematically creating voids parallel to the z axis.
# For the sake of convenience/clarity, this was done for voids that have
# the same z value.


# b21 to b29 is for the bottom face of layer 1 (z=0)

b21 = Box(Point(0.065,0.065,0),Point(0.935,0.935,0.065))
b22 = Box(Point(1.065,0.065,0),Point(1.935,0.935,0.065))
b23 = Box(Point(2.065,0.065,0),Point(2.935,0.935,0.065))
b24 = Box(Point(0.065,1.065,0),Point(0.935,1.935,0.065))
b25 = Box(Point(1.065,1.065,0),Point(1.935,1.935,0.065))
b26 = Box(Point(2.065,1.065,0),Point(2.935,1.935,0.065))
b27 = Box(Point(0.065,2.065,0),Point(0.935,2.935,0.065))
b28 = Box(Point(1.065,2.065,0),Point(1.935,2.935,0.065))
b29 = Box(Point(2.065,2.065,0),Point(2.935,2.935,0.065))

geo = geo - b21 - b22 - b23 - b24 - b25 - b26 - b27 - b28 - b29


# b30 to b38 is for the top face of layer 3 (z=3)

b30 = Box(Point(0.065,0.065,2.935),Point(0.935,0.935,3))
b31 = Box(Point(1.065,0.065,2.935),Point(1.935,0.935,3))
b32 = Box(Point(2.065,0.065,2.935),Point(2.935,0.935,3))
b33 = Box(Point(0.065,1.065,2.935),Point(0.935,1.935,3))
b34 = Box(Point(1.065,1.065,2.935),Point(1.935,1.935,3))
b35 = Box(Point(2.065,1.065,2.935),Point(2.935,1.935,3))
b36 = Box(Point(0.065,2.065,2.935),Point(0.935,2.935,3))
b37 = Box(Point(1.065,2.065,2.935),Point(1.935,2.935,3))
b38 = Box(Point(2.065,2.065,2.935),Point(2.935,2.935,3))

geo = geo - b30 - b31 - b32 - b33 - b34 - b35 - b36 - b37 - b38


# b39 to b50 is for the bottom face of layer 2 (z=1)

b39 = Box(Point(0.065,0.065,0.935),Point(0.435,0.935,1.065))
b40 = Box(Point(0.565,0.065,0.935),Point(1.435,0.935,1.065))
b41 = Box(Point(1.565,0.065,0.935),Point(2.435,0.935,1.065))
b42 = Box(Point(2.565,0.065,0.935),Point(2.935,0.935,1.065))
b43 = Box(Point(0.065,1.065,0.935),Point(0.435,1.935,1.065))
b44 = Box(Point(0.565,1.065,0.935),Point(1.435,1.935,1.065))
b45 = Box(Point(1.565,1.065,0.935),Point(2.435,1.935,1.065))
```

```python
b46 = Box(Point(2.565,1.065,0.935),Point(2.935,1.935,1.065))
b47 = Box(Point(0.065,2.065,0.935),Point(0.435,2.935,1.065))
b48 = Box(Point(0.565,2.065,0.935),Point(1.435,2.935,1.065))
b49 = Box(Point(1.565,2.065,0.935),Point(2.435,2.935,1.065))
b50 = Box(Point(2.565,2.065,0.935),Point(2.935,2.935,1.065))

geo = geo - b39 - b40 - b41 - b42 - b43 - b44 - b45 - b46 - b47 - b48 - b49 - b50


# b51 to b52 is for the bottom face of layer 3 (z=2)

b51 = Box(Point(0.065,0.065,1.935),Point(0.435,0.935,2.065))
b52 = Box(Point(0.565,0.065,1.935),Point(1.435,0.935,2.065))
b53 = Box(Point(1.565,0.065,1.935),Point(2.435,0.935,2.065))
b54 = Box(Point(2.565,0.065,1.935),Point(2.935,0.935,2.065))
b55 = Box(Point(0.065,1.065,1.935),Point(0.435,1.935,2.065))
b56 = Box(Point(0.565,1.065,1.935),Point(1.435,1.935,2.065))
b57 = Box(Point(1.565,1.065,1.935),Point(2.435,1.935,2.065))
b58 = Box(Point(2.565,1.065,1.935),Point(2.935,1.935,2.065))
b59 = Box(Point(0.065,2.065,1.935),Point(0.435,2.935,2.065))
b60 = Box(Point(0.565,2.065,1.935),Point(1.435,2.935,2.065))
b61 = Box(Point(1.565,2.065,1.935),Point(2.435,2.935,2.065))
b62 = Box(Point(2.565,2.065,1.935),Point(2.935,2.935,2.065))

geo = geo - b51 - b52 - b53 - b54 - b55 - b56 - b57 - b58 - b59 - b60 - b61 - b62


# Once the geometry is completed, the only thing that remains is to
# mesh the geometry.

# This can again be done easily using the inbuilt mesh tool in FEniCS.
# 3D tetragonal mesh elements are used to mesh the geometry. The number
# in the function call is used to specify the number of elements along
# the characteristic geometric features such as edges.

mesh = generate_mesh(geo,20)

# Finally, a plot of the meshed geometry is made. This can be done
# easily.

plot(mesh,color='red')
```

Bibliography

[1] `https://dare.tudelft.nl/`.

[2] J Zlopaša. *Exploring the Structure, Properties, and Applications of Highly Ordered Bionanocomposites*. PhD thesis, TU Delft, 2017.

[3] LJ Lee, C Zeng, X Cao, X Han, J Shen, and G Xu. Polymer nanocomposite foams. *Composites science and technology*, 65(15-16):2344–2363, 2005.

[4] `https://www.bonappetit.com/recipe/sponge-cake`.

[5] LJ Gibson and MF Ashby. *Cellular solids: structure and properties*. Cambridge university press, 1999.

[6] `https://www.nasa.gov/centers/johnson/pdf/584728main_Wings-ch4b-pgs182-199.pdf`.

[7] `https://www.nasa.gov/sites/default/files/atoms/files/shuttle_tiles_5_8v2.pdf`.

[8] B Wang, RX Wang, and Y Wu. The young's moduli prediction of random distributed short-fiber-reinforced polypropylene foams using finite element method. *Science in China Series E: Technological Sciences*, 52(1):72–78, 2009.

[9] W Pabst, T Uhlířová, E Gregorová, and A Wiegmann. Young's modulus and thermal conductivity of closed-cell, open-cell and inverse ceramic foams–model-based predictions, cross-property predictions and numerical calculations. *Journal of the European Ceramic Society*, 38(6):2570–2578, 2018.

[10] Wenqi Zhu, Nawfal Blal, Salvatore Cunsolo, and Dominique Baillis. Micromechanical modeling of effective elastic properties of open-cell foam. *International Journal of Solids and Structures*, 115:61–72, 2017.

[11] Amalie E Donius, Andong Liu, Lars A Berglund, and Ulrike GK Wegst. Superior mechanical performance of highly porous, anisotropic nanocellulose–montmorillonite aerogels prepared by freeze casting. *Journal of the mechanical behavior of biomedical*

materials, 37:88–99, 2014.

[12] S Lingard and J Underwood. Entry, descent and landing systems. In *The International Handbook of Space Technology*, pages 515–539. Springer, 2014.

[13] A-b Cherki, B Remy, A Khabbazi, Y Jannot, and D Baillis. Experimental thermal properties characterization of insulating cork–gypsum composite. *Construction and building materials*, 54:202–209, 2014.

[14] MAV Es. *Polymer-Clay Nanocomposites. The importance of particle dimensions.* PhD thesis, TU Delft, 2001.

[15] DPN Vlasveld. *Fibre reinforced polymer nanocomposites.* PhD thesis, TU Delft, 2005.

[16] C Özdilek. *Colloidal liquid crystal reinforced nanocomposites.* PhD thesis, TU Delft, 2006.

[17] ML Nobel. *Acrylic polymer nanocomposite resins for water borne coating applications.* PhD thesis, TU Delft, 2007.

[18] R Kochetov. *Thermal and Electrical Properties of Nanocomposites, Including Material Processing.* PhD thesis, TU Delft, 2012.

[19] X Han, C Zeng, LJ Lee, KW Koelling, and DL Tomasko. Extrusion of polystyrene nanocomposite foams with supercritical co_2. *Polymer Engineering & Science*, 43(6):1261–1275, 2003.

[20] X Cao, LJ Lee, T Widya, and C Macosko. Polyurethane/clay nanocomposites foams: processing, structure and properties. *Polymer*, 46(3):775–783, 2005.

[21] CC Ibeh and M Bubacz. Current trends in nanocomposite foams. *Journal of Cellular Plastics*, 44(6):493–515, 2008.

[22] L Chen, D Rende, LS Schadler, and R Ozisik. Polymer nanocomposite foams. *Journal of Materials Chemistry A*, 1(12):3837–3850, 2013.

[23] Y Fujimoto, SS Ray, M Okamoto, A Ogami, K Yamada, and K Ueda. Well-controlled biodegradable nanocomposite foams: from microcellular to nanocellular. *Macromolecular Rapid Communications*, 24(7):457–461, 2003.

[24] `https://airandspace.si.edu/exhibitions/apollo-to-the-moon/online/astronaut-life/food-in-space.cfm`.

[25] `https://www.lifeloveandsugar.com/how-to-make-homemade-whipped-cream/`.

[26] MA Schuetz. Heat transfer in foam insulation, 1983.

[27] MA Schuetz and LR Glicksman. A basic study of heat transfer through foam insulation. *Journal of Cellular Plastics*, 20(2):114–121, 1984.

[28] LR Glicksman. Heat transfer in foams. In *Low density cellular plastics*, pages 104–152. Springer, 1994.

[29] JP Holman. *Heat transfer*. McGraw-Hill Companies, 1976.

[30] Helena Pereira. The thermochemical degradation of cork. *Wood Science and Technology*, 26(4):259–269, 1992.

[31] Ralph E Grim and Georges Kulbicki. Montmorillonite: high temperature reactions and classification. *American Mineralogist: Journal of Earth and Planetary Materials*, 46(11-12):1329–1369, 1961.

[32] `https://web.archive.org/web/20150924092312/http://www.rpgroup.caltech.edu/courses/me96/flame2003.pdf`.

[33] `https://www.grc.nasa.gov/www/BGH/hihyper.html`.

[34] AN Gent and AG Thomas. The deformation of foamed elastic materials. *Journal of Applied Polymer Science*, 1(1):107–113, 1959.

[35] LJ Gibson and MF Ashby. The mechanics of three-dimensional cellular materials. *Proceedings of the Royal Society of London. A. Mathematical and Physical Sciences*, 382(1782):43–59, 1982.

[36] DJ Green. Fabrication and mechanical properties of lightweight ceramics produced by sintering of hollow spheres. *Journal of the American Ceramic Society*, 68(7):403–409, 1985.

[37] RM Christensen. Mechanics of low density materials. *Journal of the Mechanics and Physics of Solids*, 34(6):563–578, 1986.

[38] MF Ashby. The properties of foams and lattices. *Philosophical Transactions of the Royal Society A: Mathematical, Physical and Engineering Sciences*, 364(1838):15–30, 2006.

[39] D Weaire. Kelvin's ideal foam structure. In *Journal of Physics: Conference Series*, page 012005. IOP Publishing, 2009.

[40] C Veyhl, IV Belova, GE Murch, and T Fiedler. Finite element analysis of the mechanical properties of cellular aluminium based on micro-computed tomography. *Materials Science and Engineering: A*, 528(13-14):4550–4555, 2011.

[41] C Betts. Benefits of metal foams and developments in modelling techniques to assess

their materials behaviour: a review. *Materials Science and Technology*, 28(2):129–143, 2012.

[42] C Barbier, PM Michaud, D Baillis, J Randrianalisoa, and A Combescure. New laws for the tension/compression properties of voronoi closed-cell polymer foams in relation to their microstructure. *European Journal of Mechanics-A/Solids*, 45:110–122, 2014.

[43] Z Li, J Zhang, J Fan, Z Wang, and L Zhao. On crushing response of the three-dimensional closed-cell foam based on voronoi model. *Mechanics of Materials*, 68:85–94, 2014.

[44] `http://math.lbl.gov/voro++/`.

[45] JC Halpin and JL Kardos. The halpin-tsai equations: a review. *Polymer Engineering & Science*, 16(5):344–352, 1976.

[46] Hans Petter Langtangen and Anders Logg. *Solving PDEs in Python: The FEniCS Tutorial I.* Springer, 2017.

[47] C Ishiyama and Y Higo. Effects of humidity on young's modulus in poly (methyl methacrylate). *Journal of Polymer Science Part B: Polymer Physics*, 40(5):460–465, 2002.

[48] Matthew Anderson, Ricardo Motta, Srinivasan Chandrasekar, and Michael Stokes. Proposal for a standard default color space for the internet—srgb. In *Color and imaging conference*, volume 1996, pages 238–245. Society for Imaging Science and Technology, 1996.

[49] Hugh S Fairman, Michael H Brill, and Henry Hemmendinger. How the cie 1931 color-matching functions were derived from wright-guild data. *Color Research & Application: Endorsed by Inter-Society Color Council, The Colour Group (Great Britain), Canadian Society for Color, Color Science Association of Japan, Dutch Society for the Study of Color, The Swedish Colour Centre Foundation, Colour Society of Australia, Centre Français de la Couleur*, 22(1):11–23, 1997.

[50] `https://upload.wikimedia.org/wikipedia/commons/6/60/Cie_Chart_with_sRGB_gamut_by_spigget.png`.

[51] TB Lewis and LE Nielsen. Dynamic mechanical properties of particulate-filled composites. *Journal of applied polymer science*, 14(6):1449–1471, 1970.

[52] LE Nielsen. Generalized equation for the elastic moduli of composite materials. *Journal of Applied Physics*, 41(11):4626–4627, 1970.

[53] LE Nielsen. Thermal conductivity of particulate-filled polymers. *Journal of applied polymer science*, 17(12):3819–3820, 1973.

[54] R Kochetov, AV Korobko, T Andritsch, PHF Morshuis, SJ Picken, and JJ Smit. Three-phase lewis-nielsen model for the thermal conductivity of polymer nanocomposites. In *2011 Annual Report Conference on Electrical Insulation and Dielectric Phenomena*, pages 338–341. IEEE, 2011.

[55] Robert J Naumann. *Introduction to the Physics and Chemistry of Materials*. CRC press, 2008.

[56] A Raja. Internship report - wascom project.